

A MEASUREMENT OF  $T_{20}$  FOR THE  ${}^1\text{H}(\bar{d}, \gamma){}^3\text{He}$  REACTION  
AND D-STATE EFFECTS IN  ${}^3\text{He}$

By

MICHEL CHRISTIAN VETTERLI

A Thesis

Submitted to the School of Graduate Studies

in Partial Fulfilment of the Requirements

for the Degree

Doctor of Philosophy

McMaster University

April, 1985



THE  ${}^1\text{H}(\bar{d}, \gamma){}^3\text{He}$  REACTION AND D-STATE EFFECTS IN  ${}^3\text{He}$



Doctor of Philosophy (1985)  
(Physics)

McMaster University  
Hamilton, Ontario

Title: A Measurement of  $T_{20}$  for the  ${}^1\text{H}(\bar{d},\gamma){}^3\text{He}$  Reaction and  
D-State Effects in  ${}^3\text{He}$ .

Author: Michel Christian Vetterli, B.Sc. (McGill University)

Supervisor: Dr. J.A. Kuehner

Number of Pages: x, 131

ABSTRACT.

The tensor analysing power  $T_{20}$  for the radiative capture reaction  ${}^1\text{H}(\bar{d}, \gamma){}^3\text{He}$  has been measured in order to test new three-body wave functions. This observable arises from the D-state of  ${}^3\text{He}$ . An effective two-body direct radiative capture calculation, which was previously shown to fit the  $a_2$  coefficient of a Legendre polynomial expansion of the differential cross-section, is found to give a good description of the present data. A range of 5% to 9% is deduced for the D-state probability in the  ${}^3\text{He}$  ground state wave function. A value of  $-0.032 \pm 0.014$  for the asymptotic D/S state ratio is extracted from the data although it is found to be model dependent.

## ACKNOWLEDGEMENTS.

There are many people whose contributions have been invaluable to my work and education at McMaster. In particular, I would like to thank the following:

Dr. John Kuehner, my supervisor, for his advice and support throughout my stay at the lab, especially during the difficult early stages of this experiment;

Dr. Henry Weller of Duke University, my "second supervisor", whose collaboration is deeply appreciated;

Drs. Jim Waddington and W.F.S. Poehlman, the other members of my committee, for their interest;

Dr. D.R. Lehman of George Washington University, for providing the wave functions for  $^3\text{He}$  and for very useful discussions on the theoretical aspects of this work;

The other members of the group for their assistance during the long runs: Dr. A.A. Pilt, Dr. C.L. Woods, and especially Anne Trudel;

The operations staff, for keeping the accelerator in good working order at voltages up to 10 MV;

John McKay for his work on the polarized ion source;

The graduate students and post-docs in the "cattle barn" for stimulating discussions (arguments?) on all aspects of physics.

Victor Janzen, the "Big Guy", my roommate for two and a half years and a good friend;

The Natural Sciences And Engineering Research Council of Canada who funded this work through grants and scholarships.

J'aimerais aussi remercier ma famille pour leur encouragement tout au long de mon education.

Finally, I would like to thank Christine, my wife, for her patience and love during the writing of this thesis.

## TABLE OF CONTENTS

Chapter	Page
1. INTRODUCTION.	1
2. THEORY.	
2.1 Three-body Wave Function.	4
2.2 Effective Two-body Radiative Capture.	10
2.3 Asymptotic D/S State Ratio.	23
3. EXPERIMENTAL METHOD.	
3.1 Excitation Function.	25
3.2 Recoil Method.	27
3.3 Kinematics.	27
3.4 Polarization.	32
4. EXPERIMENTAL SET-UP.	
4.1 Polarized Ion Source.	40
4.2 Beam Transport System.	45
4.3 Detector Configuration.	48
4.4 Detectors.	50
4.5 Electronics.	58
4.6 Beam Steering.	61

Chapter	Page
5. DATA ANALYSIS AND RESULTS.	
5.1 Experimental Details.	62
5.2 Monitor Detector.	63
5.3 Polarization Monitor.	63
5.4 Calibration.	66
5.5 Resolution.	70
5.6 Error in $T_{20}$ .	73
5.7 Results.	74
6. COMPARISON WITH THEORY.	
6.1 Wave Functions.	84
6.2 Dependence on the Order of the Transition	87
6.3 Dependence on Partial Waves.	87
6.4 Dependence on the Optical Potential.	91
6.5 Dependence on $P_D(d)$ .	91
6.6 Second Calculation.	96
6.7 M1 Correction.	96
6.8 $T_{21}$ , $T_{22}$ , $\sigma(\theta)$ .	106
6.9 Asymptotic D/S State Ratio.	106
7. CONCLUSION.	115
APPENDICES: A - Relativistic Kinematics.	119
B - Coefficients $a_k$ and $c_k$ .	125
SIBLIOGRAPHY.	129



LIST OF TABLES.

Table	Page
2.1 Possible States for $^3\text{He}$ .	9
2.2 Possible Total Wave Functions for $^3\text{He}$ .	11
2.3 Main Components of the $^3\text{He}$ Wave Function	12
2.4 Possible Transitions.	16
2.5 Optical Model Potential.	18
2.6 D-State Properties of the $^3\text{He}$ Wave Functions.	21
5.1 Values of $T_{20}(\theta)$ for the First Experiment.	79
5.2 Values of $T_{20}(\theta)$ for the Second Experiment.	80
5.3 Results for $T_{20}(\theta)$ Averaged over the Two Runs.	81
6.1 Matrix Elements for $P_D(d) = 7\%$	100
6.2 $a_k$ and $c_k$ Coefficients for $P_D(d) = 7\%$	102

LIST OF FIGURES.

Figure	Page
2.1 Link between the D-state and the S= 3/2 channel.	15
3.1 Excitation Function.	26
3.2 Kinematics for the ${}^1\text{H}(\bar{d}, \gamma){}^3\text{He}$ Reaction.	31
3.3 Madison Convention.	36
4.1 Polarized Ion Source Schematic.	41
4.2 Deuterium Breit-Rabi Diagram.	43
4.3 Spin Filter Output Current.	44
4.4 Spin Axis Alignment.	47
4.5 Detector Configuration.	49
4.6 Resistive Wire Detector.	52
4.7 $\Delta E$ : Resistive Wire.	54
4.8 E: Position Sensitive Detector.	55
4.9 Counter Positions.	57
4.10 Electronics for the ${}^3\text{He}$ Detectors.	59
4.11 Monitor Electronics.	60
5.1 Monitor Spectrum.	64
5.2 Calibration.	68
5.3 Resolution for Detector 1.	71
5.4 Resolution for Detector 2.	72
5.5 - 5.8 Position Spectra.	75-78
5.9 Experimental Results.	82

Figure	Page
6.1 S-States.	85
6.2 D-States.	86
6.3 Transition Dependence.	88
6.4 Partial Wave Dependence.	89
6.5 Potential Dependence.	92
6.6 $P_D(d)$ Dependence.	94
6.7 $T_{20}(90^\circ)$ .	95
6.8 Comparison with Santos.	97
6.9 M1 Correction.	104
6.10 Calculated $T_{21}$	107
6.11 Calculated $T_{22}$	108
6.12 Calculated Differential Cross-Section..	109
6.13 Asymptotic Wave Function.	111
6.14 $\eta$ Dependence.	112
6.15 $r_{\text{cut}}$ Dependence.	114

## Chapter 1: INTRODUCTION

Recent theoretical calculations of few-body wave functions have stimulated interest in new measurements on very light nuclei (GL84, SS79). In particular, this thesis describes a study of the three-body system through the  ${}^1\text{H}(\vec{d}, \gamma){}^3\text{He}$  reaction. Several related reactions have been used to study the ground state of  ${}^3\text{He}$ . Among these are photo-disintegration (HP73, AC83), and electro-disintegration (SA83) of  ${}^3\text{He}$ , radiative capture of protons by deuterons (MK74, KR83, SW79a), and capture of deuterons by protons (BB70). These reactions are particularly interesting because the reaction mechanism depends on the electro-magnetic interaction only. This avoids problems due to the presence of the nuclear interaction and allows the wave functions to be studied independently of the reaction mechanism.

The  $a_2$  coefficient of a Legendre polynomial expansion of the differential cross-section for  $\gamma$ -ray emission following the capture of protons by deuterons has been found sensitive to the D-state component of the  ${}^3\text{He}$  ground state wave function (KR83). As pointed out by Seyler and Weller, the tensor analysing powers of the reaction  ${}^1\text{H}(\vec{d}, \gamma){}^3\text{He}$  are expected to be more sensitive to D-state effects (SW79b).

This is because the analysing powers result from the interference between the  $S=1/2$  and  $S=3/2$  channels and vanish if the latter, which arises from the presence of the D-state, is absent. The  $S=3/2$  channel enters into the expression for the differential cross-section only as a small perturbation. These considerations will be developed further in chapter 2.

This thesis reports measurements of the tensor analysing power  $T_{20}$  for the reaction  $^1\text{H}(\vec{d}, \gamma)^3\text{He}$ . The results are compared with an effective two-body direct radiative capture model similar to the one used to fit the cross-section (KR83). In addition, a value for the asymptotic D/S state ratio  $\eta$  is extracted from the data.

Chapter 2 deals with the theoretical aspects of this work. It begins with a detailed description of the three-body wave function followed by a discussion of the direct radiative capture model and the relationship between the matrix elements generated by this model and the analysing powers. The chapter concludes with a discussion of the asymptotic D/S state ratio.

Chapter 3 deals with the experimental methods used in this study. Topics include: the detection of recoil  $^3\text{He}$  particles, relativistic kinematics, polarization in nuclear physics, and the monitoring of the beam polarization.

The instrumentation necessary for this experiment is the topic of chapter 4 which begins with a description of the polarized ion source. This is followed by discussions

of the spectrograph, the targets, the detectors, and the electronics. The final section of this chapter deals with the method used to steer the beam which was of great importance.

Chapter 5 presents the data analysis and results, with the questions of normalization, corrections for beam polarization, calibration of the detectors, and resolution being considered. An error analysis is also done in this chapter.

A comparison of the results with theoretical predictions is made in chapter 6. The dependence of  $T_{20}$  on several parameters is examined. For example, the variations in the angular distribution of the analysing power with respect to the order of the electro-magnetic transition considered, the partial waves included in the entrance channel, the choice of the optical potential, and the D-state probability are studied. A parametrization of the M1 contribution is also included. Theoretical predictions for the other tensor analysing powers ( $T_{21}$  and  $T_{22}$ ) as well as for the differential cross-section are shown. This chapter concludes with a discussion of the results in terms of the asymptotic D/S state ratio  $\eta$ .

A summary and conclusions can be found in chapter 7.

## Chapter 2: THEORY

Before attempting to understand the radiative capture process in three-body systems, it is useful to review briefly our knowledge of the three-body wave function and to examine which components of this wave function will be studied with the  ${}^1\text{H}(\bar{d}, \gamma){}^3\text{He}$  reaction. This is followed by a description of the effective two-body radiative capture calculation used to obtain the transition matrix elements. These are then related to the analysing powers. An alternative method of analysing the data using asymptotic wave functions to obtain a value for  $\eta$ , the asymptotic D/S state ratio, is described in the final section of this chapter.

### 2.1 Three-body wave function.

This discussion follows closely the review paper of Delves (De67). Although it deals mainly with  ${}^3\text{H}$ , the conclusions also apply to  ${}^3\text{He}$  because the Coulomb interaction does not affect significantly the details of the wave function, its effect being limited to the binding energy ( $E_B({}^3\text{H}) = -8.492$  MeV,  $E_B({}^3\text{He}) = -7.728$  MeV) (FG82). In fact, the quantum numbers of these nuclei differ only in  $T_3$ , the projection of the isospin, which is related to the charge ( $T_3({}^3\text{He}) = +1/2$ ,  $T_3({}^3\text{H}) = -1/2$ ).

Since nuclear forces are non-central and isospin dependent, the only good quantum numbers of a nucleus are its total angular momentum  $J$ , its projection  $J_z$ , the parity  $\pi$ , and  $T_3$ . The wave functions are complicated by the fact that  $L$ , the orbital angular momentum, and  $S$ , the spin, are not conserved. However, since non-central forces are weak, wave functions with different  $L$  are not strongly mixed in light nuclei. The same is true for the spin. Therefore, wave functions with good  $L$  and  $S$  can be used as a basis in the description of three-body systems. For convenience, the components of the wave function are labelled by their associated  $L$  and  $S$ .

The weakness of the non-central forces also leads to the domination of one term in the ground state wave function. This is the term that remains if these forces are ignored and  $L$  and  $S$  become good quantum numbers. The properties of  ${}^3\text{H}$  and  ${}^3\text{He}$  should reflect this.

The ground state of  ${}^3\text{H}$  has  $J^\pi=1/2^+$ . This is determined by a measurement of the hyperfine structure of tritium. An isospin assignment of  $T=1/2$  is made based on the absence of a bound state of either the tri-neutron or  ${}^3\text{Li}$ ;  ${}^3\text{H}$  and  ${}^3\text{He}$  form an isospin doublet. The dominant term in the wave function has  $L=0$  and  $S=1/2$ . This is consistent with a study of the magnetic moments,  $\mu$ , of  ${}^3\text{H}$  and  ${}^3\text{He}$ . The orbital angular momentum does not make a contribution to  $\mu$  because  $L=0$  and the state is symmetric. For  ${}^3\text{H}$ , the spin contribution comes from the proton because the neutrons are



paired to  $S=0$ . The magnetic moment of  ${}^3\text{H}$  is  $\mu({}^3\text{H}) = 2.9788$  nuclear magnetons (NM); the proton has  $\mu_p = 2.7927$  NM. Similarly for  ${}^3\text{He}$ , only the neutron contributes to  $\mu$  and  $\mu({}^3\text{He}) = -2.1274$  NM. This is compared to  $\mu_n = -1.9130$  NM for the neutron. The discrepancy in these numbers is thought to be due to meson exchange currents. These should have the same magnitude for both nuclei with only a change in sign. Hence, taking an average of the magnetic moments will eliminate exchange effects; we get:

$$1/2 (\mu({}^3\text{H}) + \mu({}^3\text{He})) = 0.4257 \text{ NM}$$

$$1/2 (\mu_p + \mu_n) = 0.4399 \text{ NM}$$

The variance in these numbers of 3.2% gives a rough estimate of the contribution of other states (different L and S) to the ground state.

We now look at the three-nucleon wave function in more detail. Since we are dealing with a three-body system, there are 9 coordinates available for a description in configuration space. The motion of the center of mass is described by 3 coordinates, leaving only six. These are defined as follows:  $x_1 = r_{23}$  is the distance from particle 2 to particle 3; similarly,  $x_2 = r_{13}$  and  $x_3 = r_{12}$ .  $x_1$ ,  $x_2$ , and  $x_3$  form a triangle. The three remaining coordinates are the Euler angles  $(\alpha, \beta, \gamma)$  defining the orientation of the triangle with respect to an arbitrary set of axes. The wave function is written as follows:

$$\psi = S(x_1, x_2, x_3) Y(\alpha, \beta, \gamma) Z(\xi_1, \xi_2, \xi_3)$$

where S is called the internal wave function, Y is the Euler

angle wave function, and  $Z$  is the spin-isospin wave function.

The symmetry of the internal wave function with respect to interchange of two particles, is given by the permutation group of three objects. This group has three irreducible representations: one symmetric (S), one anti-symmetric (A), and one with mixed symmetry (M). The corresponding wave functions are:

$$F_S(1,2,3) = 1/6 (F(123)+F(213)+F(132)+F(321)+F(231)+F(312))$$

$$F_A(1,2,3) = 1/6 (F(123)-F(213)-F(132)-F(321)+F(231)+F(312))$$

$$F_{M1}(1,2,3) = 1/6(2F(123)+2F(213)-F(132)-F(321)-F(231)-F(312))$$

$$F_{M2}(1,2,3) = 1/6(2F(123)-2F(213)+F(132)+F(321)-F(231)-F(312))$$

where  $F$  is some function of  $x_1$ ,  $x_2$ , and  $x_3$  and  $F_{M1}$  and  $F_{M2}$  together span the mixed symmetry representation. The symmetric state (S) is favoured in the ground state for two reasons. Being symmetric, (S) has fewer nodes than (A) or (M), and therefore has a smaller average derivative. It follows that the kinetic energy of the (S) state is lower than for the other states. Furthermore, an attractive nuclear potential  $V(r)$  is maximum for small  $r$ . In this region, the symmetric wave function is larger than the anti-symmetric function which must go to zero at  $r=0$ ; the same is true, to a lesser degree, for the mixed symmetry state. The expectation value  $\langle \psi | V | \psi \rangle$  is larger for the (S) state which therefore has a larger binding energy. The symmetric state is favoured for both potential and kinetic energy considerations.

Three spin 1/2 particles can couple either to  $S=1/2$  or  $S=3/2$ . Since the ground state has  $J=1/2$ , the choice of  $L$  is limited. The possible states are shown in table 2.1; the spectroscopic notation  $^{2S+1}L_J$  is used. The Euler angle wave functions are given by the rotational functions  $D_{\mu M}^L(\alpha, \beta, \gamma)$  (De67). The parity of these functions is  $\pi = (-1)^\mu$ . Since the parity of the ground state is positive, only even values of  $\mu$  are allowed. Hence, there is one S-state:  $D_{00}^0(\alpha, \beta, \gamma)$  which is symmetric with respect to interchange of two particles. Only the  $\mu=0$  P-state is allowed; it is anti-symmetric. There are three possible D-states: one with  $\mu=0$ , two with  $|\mu|=2$ . The first is symmetric while the latter can be combined into one symmetric and one anti-symmetric function.

A classification of the spin-isospin wave functions has been done by Blatt (Bl53). The results are given here for  $T=1/2$ :

$S=1/2$  : one symmetric function.

one anti-symmetric function.

one set of two mixed symmetry functions.

$S=3/2$  : one set of two mixed symmetry functions.

The total wave function must be anti-symmetric; this determines the internal wave function once the Euler angle and spin-isospin wave functions have been chosen.

- The S-state has  $S=1/2$ ; there are three spin-isospin functions associated with  $S=1/2$ .

Table 2.1  
POSSIBLE STATES FOR  ${}^3\text{He}$

Possible combinations of orbital angular momentum  $L$  and spin  $S$  for the ground state of the three-body system which has total angular momentum  $J^\pi = 1/2^+$ .

The notation  ${}^{2S+1}L_J$  is used.

$S = 1/2, 3/2.$

---

$+ L = 0$	$S = 1/2$	${}^2S_{1/2}$
$+ L = 1$	$S = 1/2$	${}^2P_{1/2}$
	$S = 3/2$	${}^4P_{1/2}$
$+ L = 2$	$S = 3/2$	${}^4D_{1/2}$

- The D-state has  $S=3/2$ ; there is only one spin-isospin function allowed, but there are three Euler angle functions associated with the D-state.
- The P-state has both  $S=1/2$  and  $S=3/2$ ; for  $S=1/2$  there are three spin-isospin functions, while there is only one for  $S=3/2$ .

These results are summarized in table 2.2.

As mentioned above, the main component of the three-body wave function is the symmetric S-state; it is called the principal S-state and has a probability of approximately 90%. The Bartlett spin exchange force gives rise to the mixed symmetry state with a probability of about 1%; this state is designated by S'. The P-states result from the spin-orbit force and make up a very small part of the wave function (<1%); they are usually neglected. As in the deuteron, the tensor force mixes in the D-state; this makes up approximately 8% to 9% of the ground state. It is effects arising from this component of the wave function that are the subject of this thesis. The components of the ground state are summarized in table 2.3.

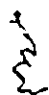
## 2.2 Effective two-body Radiative Capture Model.

The formalism for direct radiative capture has been reviewed by Weller and Roberson (WRSO). The model used here is the same one used by King et al, to fit the differential cross-section data (KRS3). The  ${}^1\text{H}(\bar{d},\gamma){}^3\text{He}$  reaction is the capture of a deuteron by a proton followed by the emission

Table 2.2

POSSIBLE TOTAL WAVE FUNCTIONS FOR  ${}^3\text{He}$ 

Possible combinations of the three parts of the wave function (internal, Euler angle, and spin-isospin), with the symmetry of these components with respect to two particle interchange.

	Internal	Euler	Spin-isospin
+ ${}^2\text{S}_{1/2}$	S	S ( $\mu=0$ )	A
	A		S
	M		M
+ ${}^2\text{P}_{1/2}$	S	A ( $\mu=0$ )	S
	A		A
	M		M
+ ${}^4\text{P}_{1/2}$	M	A ( $\mu=0$ )	M
+ ${}^4\text{D}_{1/2}$	M	S ( $\mu=0$ )	M
	M	S ( $\mu= 2 $ )	M
	M	A ( $\mu= 2 $ )	M

S: Symmetric  
 A: Anti-symmetric  
 M: Mixed symmetry

Table 2.3  
MAIN COMPONENTS OF THE  $^3\text{He}$  WAVE FUNCTION

- Principal S-state	= 90%
- Mixed symmetry state S'	= 1%
- P-state	< 1%
- D-state	8-9%

of a  $\gamma$ -ray. The final state of the  ${}^3\text{He}$  is a two body d+p state. Hence, the capture is independent of the nuclear interaction and involves only the electro-magnetic operator. Since the form of this operator is well-known, this reaction lends itself well to a study of the final bound state wave function.

As we have just seen, the ground state has many components due to non-central terms in the nuclear potential. The P and S' states will not be included in the following calculations; only the principal S-state ( $L=0$ ,  $S=1/2$ ) and the D-state ( $L=2$ ,  $S=3/2$ ) will be considered. This approximation still takes into account more than 98% of the wave function.

Since the deuteron has spin 1 and the proton spin  $1/2$ , the only possible values for the spin of the d+p state are  $S=1/2$  and  $S=3/2$ ;  $S$  is called the channel spin. Initially, only electric multipole transitions are considered because M1 radiation gives rise to transitions to the S' state which has low probability and because of technical difficulties explained below. The electric multipole operator has the form  $E\lambda = q_{\text{eff}} r^\lambda Y_\lambda^M(\theta, \phi)$  in the long wavelength approximation.  $q_{\text{eff}}$  is the effective charge which will be defined later,  $Y_\lambda^M$  is a spherical harmonic, and  $\lambda$  is the order of the transition. It is important to notice that the operator does not depend on spin. Hence, if the reaction proceeds through the  $S=3/2$  channel, the  $\gamma$  transition must be to the D-state. One must be careful in



making this assumption because it is only true if initial state interactions are ignored. A spin dependent potential in the initial state of the deuteron-proton system may cause mixing of the  $S=1/2$  and  $S=3/2$  states in the entrance channel. The resulting state would be free to decay to the  $S$  component of the ground state. However, this is thought to be a small effect for the tensor analysing powers and almost all of the  $S=3/2$  channel can be attributed to the presence of the  $D$ -state. These considerations are summarized in fig. 2.1.

As will be shown later, the tensor analysing power  $T_{20}$  is due to the interference between the  $S=3/2$  and the  $S=1/2$  channels. If there is no  $S=3/2$  amplitude, the analysing power is zero. This makes a measurement of  $T_{20}$  ideal for studying  $D$ -state effects in  ${}^3\text{He}$ .

Electric multipole transitions up to  $l=3$  are included in this calculation although only  $E1$  and  $E2$  transitions are shown to make a significant contribution. Considering the selection rules for electro-magnetic transitions and the spin and parity of the ground state of  ${}^3\text{He}$ , it is possible for the capture reaction to take place in the following intermediate scattering states:

$$E1: 1/2^-, 3/2^-$$

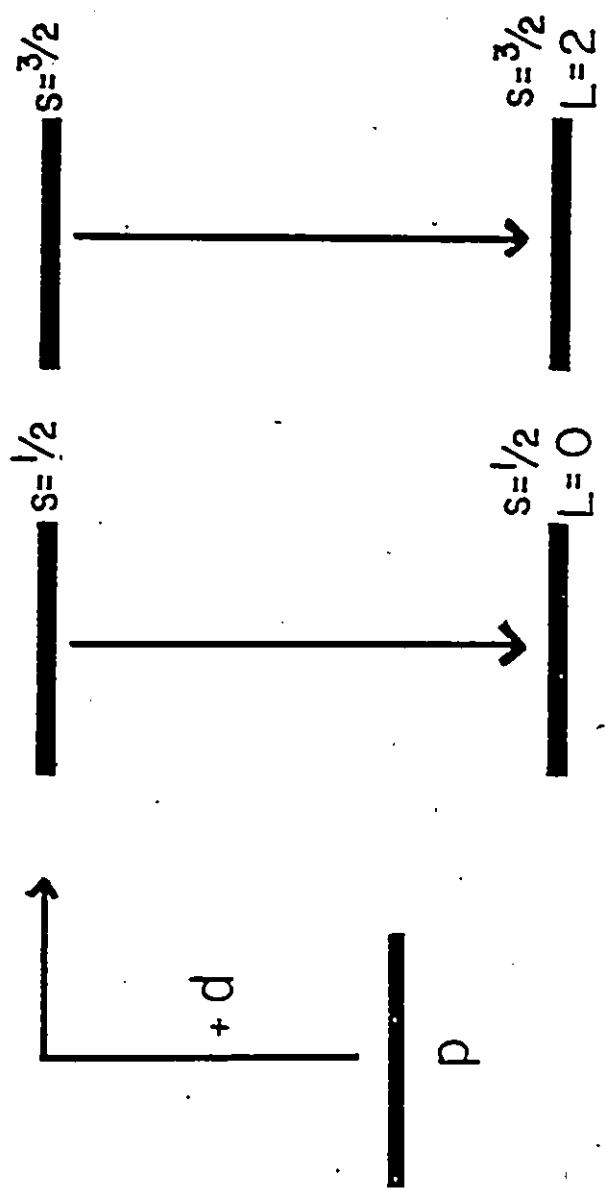
$$E2: 3/2^+, 5/2^+$$

$$E3: 5/2^-, 7/2^-$$

$$M1: 1/2^+, 3/2^+$$

There are 17 channels through which the reaction can proceed

Fig. 2.1 Illustration of the link between the D-state of  $^3\text{He}$  and the  $S = 3/2$  channel.



${}^3\text{He}$   
 $J^\pi = 1/2^+$

Table 2.4

## POSSIBLE TRANSITIONS

The reaction channels for E1, E2, E3, and M1 transitions are listed. L is the orbital angular momentum in the entrance channel, S is the channel spin, and J is the total angular momentum of the intermediate state.

L	S	J	$2S+1L_{2J+1}$	E $\ell$ , M $\ell$
0	1/2	1/2 <sup>+</sup>	$2S_2$	M1
	3/2	3/2 <sup>+</sup>	$4S_4$	E2, M1
1	1/2	3/2 <sup>-</sup>	$2P_4$	E1
		1/2 <sup>-</sup>	$2P_2$	E1
	3/2	5/2 <sup>-</sup>	$4P_6$	E3
		3/2 <sup>-</sup>	$4P_4$	E1
		1/2 <sup>-</sup>	$4P_2$	E1
2	1/2	5/2 <sup>+</sup>	$2D_6$	E2
		3/2 <sup>+</sup>	$2D_4$	E2, M1
	3/2	5/2 <sup>+</sup>	$4D_6$	E2
		3/2 <sup>+</sup>	$4D_4$	E2, M1
		1/2 <sup>+</sup>	$4D_2$	M1
3	1/2	7/2 <sup>-</sup>	$2F_8$	E3
		5/2 <sup>-</sup>	$2F_6$	E3
	3/2	7/2 <sup>-</sup>	$4F_8$	E3
		5/2 <sup>-</sup>	$4F_6$	E3
		3/2 <sup>-</sup>	$4F_4$	E1
4	3/2	5/2 <sup>+</sup>	$4G_6$	E2
5	3/2	7/2 <sup>-</sup>	$4H_8$	E3

if E1, E2, and E3 transitions are considered; they are listed in table 2.4 where they are labelled by the orbital angular momentum L, the spin S, and the total angular momentum J of the intermediate state. The notation  $^{2S+1}L_{2J+1}$  is used. This should not be confused with the states of table 2.1 which refer to the components of the ground state wave function. M1 transitions are also included for completeness.

The matrix elements for this reaction are written:

$\langle \phi(^3\text{He}); \gamma | \text{EM} | d+p; 0 \rangle$  where EM is the electro-magnetic operator. As seen previously,  $\text{EM} = E_L = q_{\text{eff}} r^L Y_L^M(\theta, \phi)$ .  $q_{\text{eff}}$ , the effective charge, varies with the order L of the transition. It is given by (BP77):

$$q_{\text{eff}}^L = \frac{A_2^L Z_1 + (-1)^L Z_2 A_1^L}{(A_1 + A_2)^L}$$

where the subscripts 1 and 2 refer to the projectile and the target. Therefore,  $q_{\text{eff}}(E1) = -0.333$ ,  $q_{\text{eff}}(E2) = 0.556$ , and  $q_{\text{eff}}(E3) = -0.259$ .  $|d+p; 0\rangle$  is a two-body wave function representing the scattering state of the deuteron and the proton, plus a vacuum for  $\gamma$ -rays. It is calculated using a distorted wave Born approximation (DWBA) with an optical potential. As in ref. (Ki83), the optical model parameters used were those of Guss. These are listed in table 2.5. The radial matrix elements were evaluated for the inverse reaction  $^2\text{H}(p, \gamma)^3\text{He}$ ; these should be the same as for  $^1\text{H}(d, \gamma)^3\text{He}$  if the energy of the incident particle is chosen

Table 2.5

## OPTICAL MODEL POTENTIAL

Potential used in the Distorted Wave Born Approximation for the entrance channel (Denoted pot.1).

$$V_0 = 90.75 - 0.4871 E_p \text{ MeV}$$

$$r_0 = 1.153 \text{ fm}$$

$$a_0 = 0.454 \text{ fm}$$

$$W_d = 6.54 - 0.10 E_p \text{ MeV} \quad (E_p > 10 \text{ MeV})$$

$$4.54 + 0.1005 E_p \text{ MeV} \quad (E_p < 10 \text{ MeV})$$

$$r_d = 1.104 \text{ fm}$$

$$a_d = 0.691 \text{ fm}$$

$$r_c = 1.3 \text{ fm}$$

---


$$V(r) = -V_0 f(a_0, r_0, r) + i 4 a_d W_d \delta/\delta r (f(a_d, r_d, r)) + V_c(r_c)$$

$$f(a_k, r_k, r) = [ 1 + \exp (r - r_k A^{1/3}/a_k) ]^{-1}$$

Note:  $E_p$  is the energy of the proton in the inverse reaction  ${}^2\text{H}(p,\gamma){}^3\text{He}$ .  $E_p = E_d/2$

to give the same center-of-mass energy in both cases ( $E_d = 19.8$  MeV,  $E_p = 9.9$  MeV). This is why the parameters of table 2.5 are quoted as a function of  $E_p$ .

The three-body wave functions  $\psi(^3\text{He})$  for the ground state of  $^3\text{He}$  were obtained from a Faddeev type calculation by Gibson and Lehman (GL84). The two-body  $^1S_0$  and  $^3S_1$ - $^3D_1$  separable interactions used in this calculation were chosen to fit two nucleon properties such as the deuteron quadrupole moment and the low energy S-wave two nucleon scattering parameters. In particular, different  $^3S_1$ - $^3D_1$  interactions which lead to a D-state probability in the deuteron,  $P_D(d)$ , of between 1% and 9% were used to generate a set of  $^3\text{He}$  wave functions. Since the D-state probability in the three nucleon system,  $P_D(^3\text{He})$ , is related to  $P_D(d)$  ( $P_D(^3\text{He}) = (1.31 \pm 0.02)P_D(d) - (0.2 \pm 0.1)$ ) (GL84) and since  $P_D(d)$  is an input parameter to the calculation, the  $^3\text{He}$  wave functions will be labelled by the corresponding value of  $P_D(d)$ . We should note that the wave functions of Gibson and Lehman are for  $^3\text{H}$ . However, as stated above, the  $^3\text{He}$  wave function should have the same shape as for  $^3\text{H}$ , the Coulomb interaction affecting only the binding energy (FG82).

Since we are considering direct radiative capture, we require not  $\psi(^3\text{He})$ , the three-body wave function, but the two-body d+p component of this function. This projection was done by Lehman by evaluating the overlap between  $\psi(^3\text{H})$  and the product of a deuteron and a neutron wave function (Le84). The functions he provides are in momentum space.

They must be converted to configuration space by a Fourier transformation. This is done using the product integration technique for Bessel functions of Lehman, Parke, and Maximon (LP81). These two-body  $d+p$  wave functions, denoted  $\phi(^3\text{He})$ , are the ones used in the calculation of the matrix elements. A summary of the D-state properties of these wave functions is given in table 2.6. It is important to note that, although there is a large variation in the amount of D-state in the three-body wave functions  $P_D(^3\text{He})$ , the corresponding D-state probability in the projected two-body wave functions  $P_D(d+p)$ , does not change very much. The significance of this point will become clear in chapter 6 when the dependence of  $T_{20}$  on  $P_D(d)$  is examined.

The radial matrix elements were calculated using the program DIRAC (We84), which is a direct radiative capture code. The results were used as input for the program CROSST (We84) which does the angular integration and gives the final values for the matrix elements. These are related to the analysing powers by Seyler and Weller (SW79b). As will be seen in chapter 3, the differential cross-section for a spin 1 projectile can be written:

$$\sigma(\theta) = \sigma_{\text{un}}(\theta) \left( 1 + \frac{3}{2} p_y A_y(\theta) + t_{20} T_{20}(\theta) + 2 \operatorname{Re}(t_{21}) T_{21} + 2 \operatorname{Re}(t_{22}) T_{22} \right)$$

where  $\sigma_{\text{un}}(\theta)$  is the unpolarized cross-section,  $p_y$  and  $t_{kq}$  are moments of the beam, and  $A_y$  and  $T_{kq}$  are the analysing powers which are properties of the reaction. The



Table 2.6  
D-STATE PROPERTIES OF THE  $^3\text{He}$  WAVE FUNCTIONS

Corresponding D-state probabilities for the deuteron, the three-body wave function, and the two-body projected wave function.

$P_D(d)$ (%)	$P_D(^3\text{He})$ (%)	$P_D(d+p)/P_S(d+p)$ (%)
1	0.74	0.32
2	2.16	0.72
3	3.65	1.00
4	5.08	1.19
5	6.49	1.33
6	7.83	1.43
7	9.12	1.50
8	10.33	1.55
9	11.52	1.58

cross-section can also be expressed as a Legendre polynomial expansion:

$$\sigma(\theta) = x/24 \sum_k ( a_k P_k + b_k P_k^1 P_y + c_k P_k t_{20} + d_k P_k^1 \text{Re}(t_{21}) + e_k P_k^2 \text{Re}(t_{22}) )$$

where  $x$  is the reduced wavelength of the projectile,  $P_k$  and  $P_k^m$  are the Legendre and associated Legendre polynomials ( $P_k = P_k(\cos \theta)$ ), and  $a_k$ ,  $b_k$ ,  $c_k$ ,  $d_k$ , and  $e_k$  are coefficients. By comparing these two equations for the cross-section, one can determine the analysing powers in terms of the coefficients:

$$T_{20}(\theta) = \frac{\sum_k c_k P_k}{\sum_k a_k P_k} \quad A_y(\theta) = \frac{2}{3} \frac{\sum_k b_k P_k^1}{\sum_k a_k P_k}$$

$$T_{21}(\theta) = \frac{1}{2} \frac{\sum_k d_k P_k^1}{\sum_k a_k P_k} \quad T_{22}(\theta) = \frac{1}{2} \frac{\sum_k e_k P_k^2}{\sum_k a_k P_k}$$

Seyler and Weller give expressions for the  $a_k$ ,  $b_k$ ,  $c_k$ ,  $d_k$ , and  $e_k$  coefficients (SW79b). For example:

$$a_k = \sum_{tt'} (-1)^{s-c+1} [ ] \hat{a} \hat{a}' \hat{L} \hat{L}' \hat{b}^2 \hat{b}'^2 \quad (k0, k'0 \quad k0)$$

$$W(kb, k'b'; sk) (L1, L'-1 \quad k0) W(Lb, L'b'; ck) \text{Re } RR'^*$$

The notation, as well as expressions for the other coefficients, can be found in ref. SW79b.  $R$  and  $R'$  are the matrix elements for the interfering channels calculated previously. The coefficients of  $\text{Re } RR'^*$  are calculated using the program LS (We84). Expressions for  $a_0 - a_4$  and  $c_0 - c_4$  are given in appendix B. All the terms of the equations for the  $c_k$  coef-

ficients depend on the  $S=3/2$  channel (i.e. at least one matrix element has a superscript 4).) If this channel has zero amplitude, all the  $c_k$  vanish and the tensor analysing power is identically zero. The situation is different for the  $a_k$  coefficients, where the two channels do not mix. Therefore, while D-state effects appear only as a perturbation in the differential cross-section, a D-state component in the  $^3\text{He}$  ground state is required for the analysing power to be non-zero.

### 2.3 Asymptotic D/S State Ratio

There is an alternative method of analysing the  $^1\text{H}(\vec{d}, \gamma)^3\text{He}$  reaction. As pointed out by Arriaga and Santos, the low energy tensor analysing powers are sensitive to the asymptotic region of the bound state wave function, and can therefore be used to determine the asymptotic D/S state ratio  $\eta$  (ACS4). Instead of using realistic wave functions generated from Faddeev equations, asymptotic functions are used for the final state  $\phi(^3\text{He})$  in the calculation of the matrix elements. This is justified if the incident energy is sufficiently low to lead to capture at large  $r$ . The validity of this assumption will be discussed in chapter 6. The asymptotic forms used are:

$$u_S = C_S \sqrt{\kappa/2\pi} \exp(-\kappa r) / r$$

$$u_D = C_D \sqrt{\kappa/2\pi} \exp(-\kappa r) / r \left( 1 + 3/\kappa r + 3/2 \kappa^2 r^2 \right)$$

where  $\kappa$  is the wave number corresponding to the deuteron separation energy in  ${}^3\text{He}$  ( $\kappa = 0.42 \text{ fm}^{-1}$ ), and  $C_S$  and  $C_D$  are the asymptotic normalization constants for the S and D states respectively. The asymptotic D/S state ratio  $\eta$  is defined as  $\eta = C_D/C_S$ . Arriaga and Santos find that  $T_{20}$  is proportional to  $\eta$ . Therefore, it should be possible to obtain a good value of this parameter. This is significant since  $\eta$  is known only through a determination of the DWBA parameter  $D_2$  for  $(d, {}^3\text{He})$  and  $(d, t)$  reactions where the deuteron acts as a spectator picking up a neutron or a proton in a mechanism similar to capture (KC79).  $D_2$  is related to  $\eta$  by the following equation:  $D_2 = \eta/\kappa^2$  (AS84). The present range for  $D_2$  is  $-0.22 \text{ fm}^2$  to  $-0.037 \text{ fm}^2$ . This corresponds to a range for  $\eta$  of  $-0.039$  to  $-0.065$ .

## Chapter 3: EXPERIMENTAL METHOD

This chapter deals with experimental technique only. A description of the instrumentation is delayed until chapter 4.

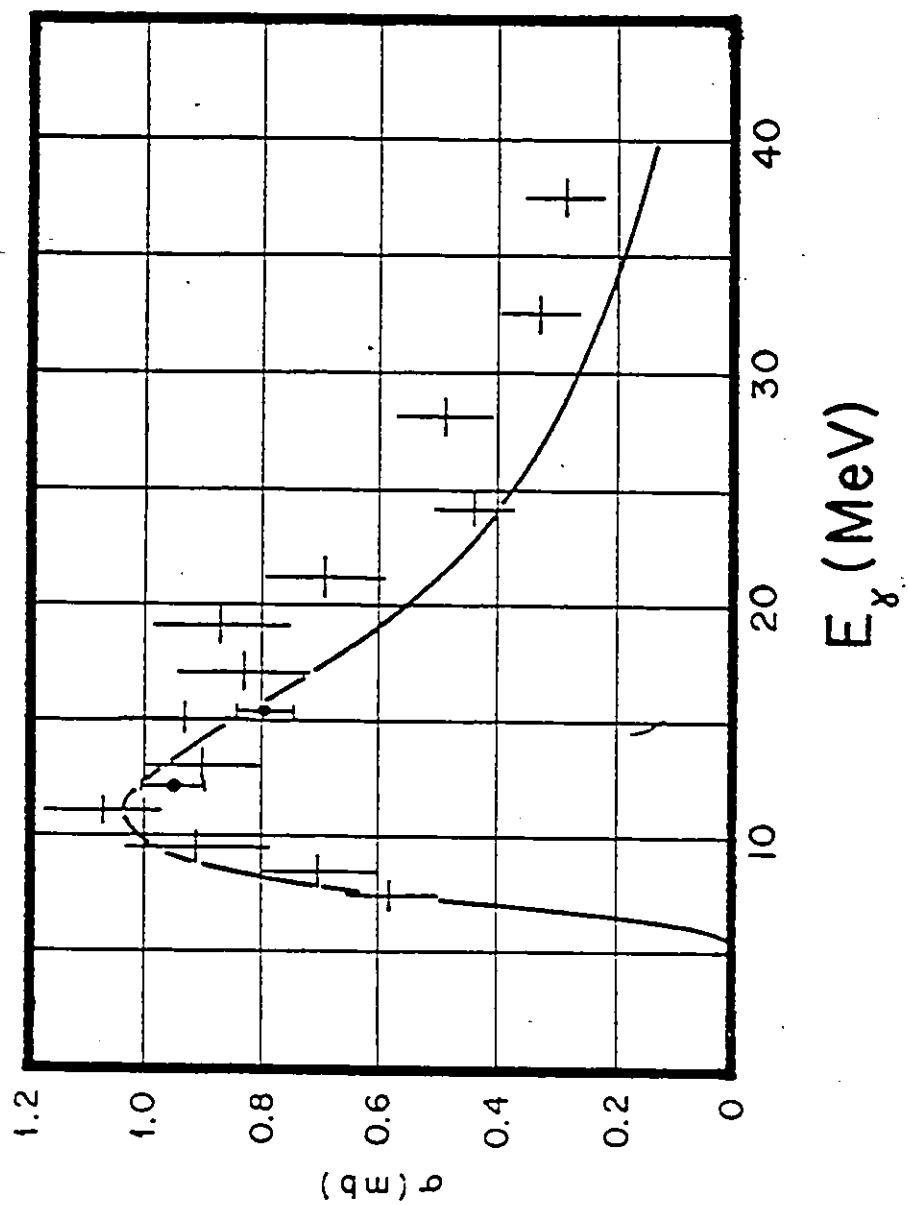
The first section explains how the choice of beam energy is related to the excitation function of the photo-disintegration of  $^3\text{He}$ . The reason for choosing to detect the recoiling  $^3\text{He}$  particles instead of the  $\gamma$ -rays is explained in section two. Section three examines the kinematics of the reaction. Since one of the particles involved is a  $\gamma$ -ray, relativistic kinematics must be used. Finally, a description of polarization in nuclear physics is given in section four.

### 3.1 Excitation Function.

The excitation function up to 40 MeV for the photo-disintegration of  $^3\text{He}$  is shown in fig. 3.1. The giant dipole resonance is the dominant feature of this graph. In order to take advantage of the largest cross-section possible, the experiment was done in the 12 MeV range of gamma-ray energy. As will be seen below, this corresponds to a beam energy of approximately 20 MeV for the  $^1\text{H}(\bar{d},\gamma)^3\text{He}$  reaction.

Fig. 3.1 Excitation Function. Excitation function for the photo-disintegration of  $^3\text{He}$  up to 40 MeV. The cross-section peaks around 11 or 12 MeV. (ref. KR83)

## EXCITATION FUNCTION



### 3.2 Recoil Method.

The angular distribution of the  $\gamma$ -rays can be determined uniquely from the energy distribution of the  $^3\text{He}$  particles. An Enge split-pole magnetic spectrograph was used to analyze the recoiling  $^3\text{He}$  nuclei. More details will be given in chapter 4. This method of obtaining  $\gamma$ -ray angular distributions avoids the problems associated with the high neutron background created by the deuteron beam in the NaI detectors. Time-of-flight discrimination against neutrons is insufficient to give a clean  $\gamma$ -ray spectrum. An added feature of the recoil method is that the full angular distribution of the  $\gamma$ -rays can be collected at once. However, since the  $^3\text{He}$  particles are constrained to a cone such that:  $0^\circ \leq \theta(^3\text{He}) \leq 2.6^\circ$ , problems associated with the beam as well as with small angle scattering from the beam must be solved.

The recoil method, although uncommon, is not new (BB70, MK74). This experiment was done previously with an unpolarized beam by Belt et al. (BB70). We chose to do the experiment for the same energy,  $E_d = 19.8$  MeV, as was used in this previous work.

### 3.3 Kinematics.

The equations in this section are derived in appendix A. The notation used must be defined. The reaction



${}^1\text{H}(\vec{d}, \gamma){}^3\text{He}$  is denoted 2(1,3)4: particle 1 strikes particle 2 resulting in the formation of particles 3 and 4. All quantities are expressed in units of energy to avoid the confusion introduced into the equations by the velocity of light  $c$ . Hence, for particle  $j$ :

$$M_j = m_j c^2 \quad ; \quad P_j = p_j c \quad ; \quad W_j = M_j + E_j = (M_j^2 + p_j^2)^{1/2}$$

where  $m_j$  is the rest mass,  $p_j$  is the momentum,  $E_j$  is the kinetic energy, and  $W_j$  is the total energy.

From equations A20 and A21, we have for the energy of the  $\gamma$ -ray in the center of mass frame:

$$E_\gamma(\text{cm}) = (a/2) [ M_1^2 + M_2^2 + 2 M_2 (M_1 + E_1) ]^{-1/2} \quad (3.1)$$

$$a = M_1^2 + M_2^2 + M_3^2 - M_4^2 + 2 M_2 (M_1 + E_1) \quad (3.2)$$

From the mass tables:

$$M_1 = M_d = 2.014102 \text{ amu} = 1876.10 \text{ MeV}$$

$$M_2 = M_p = 1.007825 \text{ amu} = 938.77 \text{ MeV}$$

$$M_3 = M_\gamma = 0$$

$$M_4 = M({}^3\text{He}) = 3.01603 \text{ amu} = 2809.77 \text{ MeV}$$

The beam energy is  $E_1 = 19.8 \text{ MeV}$ . Putting these quantities into equations (3.1) and (3.2) gives a  $\gamma$ -ray energy of 12.07 MeV. As previously noted, this corresponds to the peak of the giant dipole resonance.

The capture reaction can also be written  ${}^1\text{H}(\vec{d}, {}^3\text{He})\gamma$ . The indices 3 and 4 can be interchanged in equations A20 and

A21 to obtain an expression for  $W'_4$ :

$$W'_4 = \frac{M_1^2 + M_2^2 + M_4^2 - M_3^2 + 2 M_2 W_1}{2 (M_1^2 + M_2^2 + 2 M_2 (E_1 + M_1))^{1/2}} = 2809.40 \text{ MeV} \quad (3.3)$$

From eq. A23:

$$\cos \theta_4 = \frac{E_4 + M_4 - W'_4/\gamma}{s (E_4^2 + 2 M_4 E_4)^{1/2}} \quad (3.4)$$

$$\gamma = (1-s^2)^{-1/2} \quad (3.5)$$

$$s = P_1 / (W_1 + M_2) \quad (\text{eq. A15}) \quad (3.6)$$

Equation 3.6 can be re-written using:

$$W^2 = p^2 + M^2 \quad \rightarrow \quad p^2 = W^2 - M^2 = (E+M)^2 - M^2$$

$$s = (E_1^2 + 2 M_1 E_1)^{1/2} / (E_1 + M_1 + M_2) \quad (3.7)$$

Substituting numerical values into eqs. 3.4, 3.5, and 3.7, we obtain:

$$s = 0.09641 \quad ; \quad \gamma = 1.00468$$

$$\cos \theta_4 = \frac{E_4 + 13.061}{0.09641 (E_4^2 + 5618.7 E_4)^{1/2}} \quad (3.8)$$

This gives us a relationship between the scattering angle of a  $^3\text{He}$  particle and its energy. Equation A22 relates the

angle of the  $\gamma$ -ray in the CM frame to the energy of the  $^3\text{He}$  particle in the lab frame:

$$\cos \theta'_3 = 1/\beta W'_3 [(E_1 + M_1 + M_2 - M_4 - E_4) / \gamma - W'_3] \quad (3.9)$$

where  $W'_3$  is  $E_\gamma(\text{cm})$  of eq. 3.1 and is equal to 12.07 MeV. Numerical substitution into eq. 9 gives:

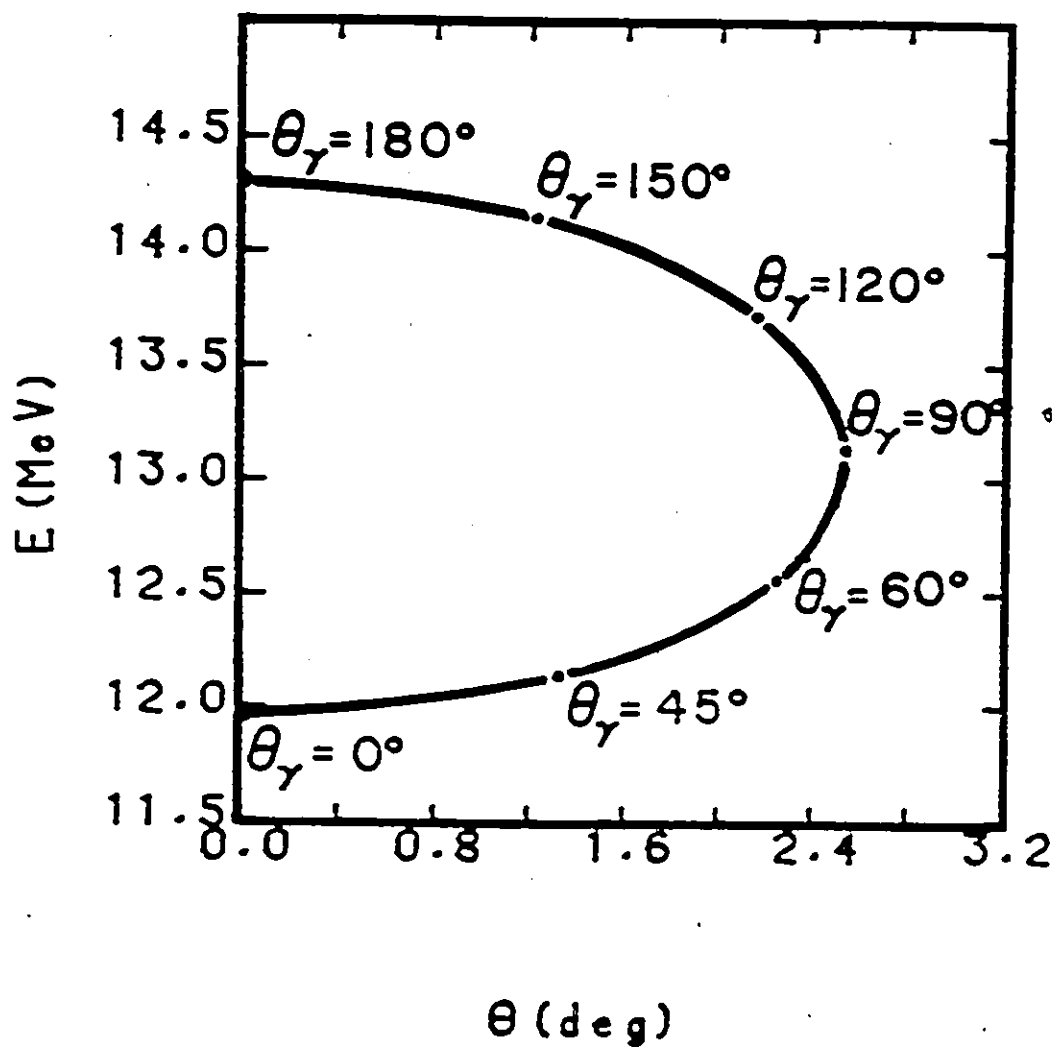
$$\begin{aligned} \cos \theta_\gamma(\text{cm}) &= 11.214 - 0.8532 E(^3\text{He}) & (3.10) \\ E_{\text{lab}}(^3\text{He}) &= 13.143 - 1.172 \cos \theta_\gamma \end{aligned}$$

These equations make the recoil method possible since they are linear in  $E(^3\text{He})$  and  $\cos \theta_\gamma$  giving a unique determination of  $\theta_\gamma$  if  $E(^3\text{He})$  is known. A graph of  $E(^3\text{He})$  versus  $\theta(^3\text{He})$  is plotted in fig. 3.2. Several  $\gamma$ -ray angles are also shown. Two points of interest experimentally are the energy and angular ranges of the  $^3\text{He}$  particles:

$$\begin{aligned} 12.0 \text{ MeV} &\ll E(^3\text{He}) \ll 14.3 \text{ MeV} \\ 0^\circ &\ll \theta(^3\text{He}) \ll 2.6^\circ \end{aligned}$$

The relatively small energy range makes it possible to accumulate differential cross-sections for many  $\gamma$ -ray angles at once, and to do so continuously with angle. However, the angular constraints on the  $^3\text{He}$  particles make them difficult to detect because of the presence of the beam.

Fig. 3.2 Kinematics for the  ${}^1\text{H}(\vec{d}, \gamma){}^3\text{He}$  Reaction. This graph shows the limitations on  ${}^3\text{He}$  energy and scattering angle. A few  $\gamma$ -ray angles in the center-of-mass frame are also shown.



### 3.4 Polarization.

We turn now to a discussion of polarization in nuclear physics. Many articles have been written on the subject (Si74, Da70, In70, In75, In80, La55, Go58, WA52). However, the treatment by M. Simonius is particularly good. In what follows, wave functions are designated by their spin only; all other quantum numbers are implied.

Consider a particle in state  $|\psi\rangle$ . If the states  $|\mu\rangle$  form an orthonormal basis in spin space, we can write  $|\psi\rangle = \sum_{\mu} a_{\mu} |\mu\rangle$ , where  $|a_{\mu}|^2$  is the probability of finding the particle in state  $|\mu\rangle$ . Two sets of basis vectors connected by a rotation only, are related by the Euler functions:

$$|\mu\rangle_{II} = \sum_{\mu'} D_{\mu',\mu}^S(\alpha, \beta, \gamma) |\mu'\rangle_I \quad (3.11)$$

where  $(\alpha, \beta, \gamma)$  are the Euler angles between the bases in spin space. ( $D_{mm'}^J(\alpha, \beta, \gamma) = \langle jm | e^{-i\alpha J_z} e^{-i\beta J_y} e^{-i\gamma J_z} | jm' \rangle$ )

Therefore, we have:

$$a_{\mu'}^{II} = \sum_{\mu} D_{\mu',\mu}^S a_{\mu}^I \quad (3.12)$$

We define the density matrix  $\rho$  as follows:

$$\rho_{\mu\mu'} = \langle a_{\mu} a_{\mu'}^* \rangle \quad (3.13)$$

where the brackets denote an ensemble average over the beam.

An alternate definition is:

$$\rho_{\mu\mu'} = 1/N \sum_{i=1}^N a_{\mu}^i a_{\mu'}^i \quad (3.14)$$

$\rho$  is normalized such that  $\text{Tr}(\rho) = 1$ . To understand why  $\rho$  is useful, we must consider the expectation value of  $A$ , where  $A$  is a hermitian operator acting on the spin part of the wave function.

$$\langle A \rangle_i = \langle \psi_i | A | \psi_i \rangle = \sum_{\mu\mu'} a_{\mu}^i a_{\mu'}^{i*} \langle \mu' | A | \mu \rangle$$

Averaging over all particles in the beam, we get:

$$\langle A \rangle = 1/N \sum_{i=1} \langle A \rangle_i = 1/N \sum_i \sum_{\mu\mu'} a_{\mu}^i a_{\mu'}^{i*} \langle \mu' | A | \mu \rangle$$

$$\langle A \rangle = \sum_{\mu\mu'} \rho_{\mu\mu'} A_{\mu'\mu}$$

$$\langle A \rangle = \text{Tr} (\rho A) \quad (3.15)$$

All spin observables can therefore be obtained from the density matrix and the operator in matrix form. Unfortunately, the density matrix is difficult to work with because of its complicated rotational properties involving two D functions:

$$\rho_{\mu\mu'}^I = \sum_{\nu\nu'} D_{\nu\mu}^{S*} D_{\nu'\mu'}^S \rho_{\nu\nu'}^I \quad (3.16)$$

To avoid these difficulties, a transformation to a new representation is made. The irreducible statistical tensors are defined as follows:

$$t_{kq} = \sqrt{2S+1} \sum_{\mu\mu'} (-1)^{S-\mu} \langle S \mu' S -\mu | kq \rangle \rho_{\mu\mu'} \quad (3.17)$$

with  $0 \leq k \leq 2S$ ;  $-k \leq q \leq k$ .

The quantity in brackets is a Clebsch-Gordan coefficient.

If we introduce  $\tau_{kq}$  such that:

$$(\tau_{kq})_{\mu\mu'} = \sqrt{2S+1} (-1)^{S-\mu} \langle S \mu' S -\mu | kq \rangle \quad (3.18)$$

then:

$$t_{kq} = \sum_{\mu\mu'} (\tau_{kq})_{\mu\mu'} \rho_{\mu\mu'} = \text{Tr} (\tau_{kq} \rho) = \langle \tau_{kq} \rangle$$

$\tau_{kq}$  is a tensor operator with expectation value  $t_{kq}$ . The latter is thus an observable of the beam.

The statistical tensor representation is chosen over the density matrix because of its simpler rotational

properties:

$$t_{kq}^{II} = \sum_{q'} D_{q'q}^k t_{kq'}^I \quad (3.19)$$

A further advantage of this representation is that tensors of different rank  $k$  are not mixed by rotations. This is important if the beam used in the experiment must have pure  $k$  (i.e. pure vector ( $k=1$ ) or pure tensor ( $k=2$ ) polarization).

Cartesian tensors are sometimes used instead of spherical tensors (Go58). However, since their use is usually restricted to  $S=1/2$  particles, they will not be discussed here.

Since the cross-section is an observable, we may write:  $\sigma = \text{Tr}(O(\sigma) \rho)$ , where  $O(\sigma)$  is an operator, and hence,  $\sigma$  depends linearly on the components of the density matrix. Since the  $t_{kq}$  are linearly related to the  $\rho_{\mu\mu'}$ ,  $\sigma$  is also a linear function of the spherical tensor moments, and we may write:

$$\sigma_{\text{pol}} = \sigma_{\text{un}} \sum_{kq} t_{kq} T_{kq}^* \quad (3.20)$$

The coefficients  $T_{kq}$  of this linear expansion of the cross-section are called the analysing powers and are characteristic of the reaction.  $T_{kq}$  is a measure of how the scatterer affects the  $t_{kq}$  component of the beam. The following equations from Simonius (Si74) are useful:

$$T_{kq} = (-1)^{k-q} T_{k-q} = (-1)^k T_{kq}^* \quad (3.21)$$

$$T_{k0} = 0 \text{ for odd } k \quad (3.22)$$

$$\sigma_{\text{pol}} = \sigma_{\text{un}} \sum_{kq} t_{kq} T_{kq}^* = \sum_{kq} \epsilon_k T_{kq} \text{Re}(\epsilon_k t_{kq}) \quad (3.23)$$

where  $\epsilon_k = 1$  for  $k$  even and  $\epsilon_k = i$  for  $k$  odd.



We can therefore write for spin 1 particles:

$$\begin{aligned} \sigma_{\text{pol}} = \sigma_{\text{un}} [ & T_{00} t_{00} + i T_{10} \text{Re}(it_{10}) + i T_{11} \text{Re}(it_{11}) \\ & + i T_{1-1} \text{Re}(it_{1-1}) + T_{20} \text{Re}(t_{20}) + T_{21} \text{Re}(t_{21}) \\ & + T_{2-1} \text{Re}(t_{2-1}) + T_{22} \text{Re}(t_{22}) + T_{2-2} \text{Re}(t_{2-2}) ] \end{aligned} \quad (3.24)$$

$T_{00} = 1$  ,  $t_{00} = 1$ , and eq. 3.21 and 3.22 give:

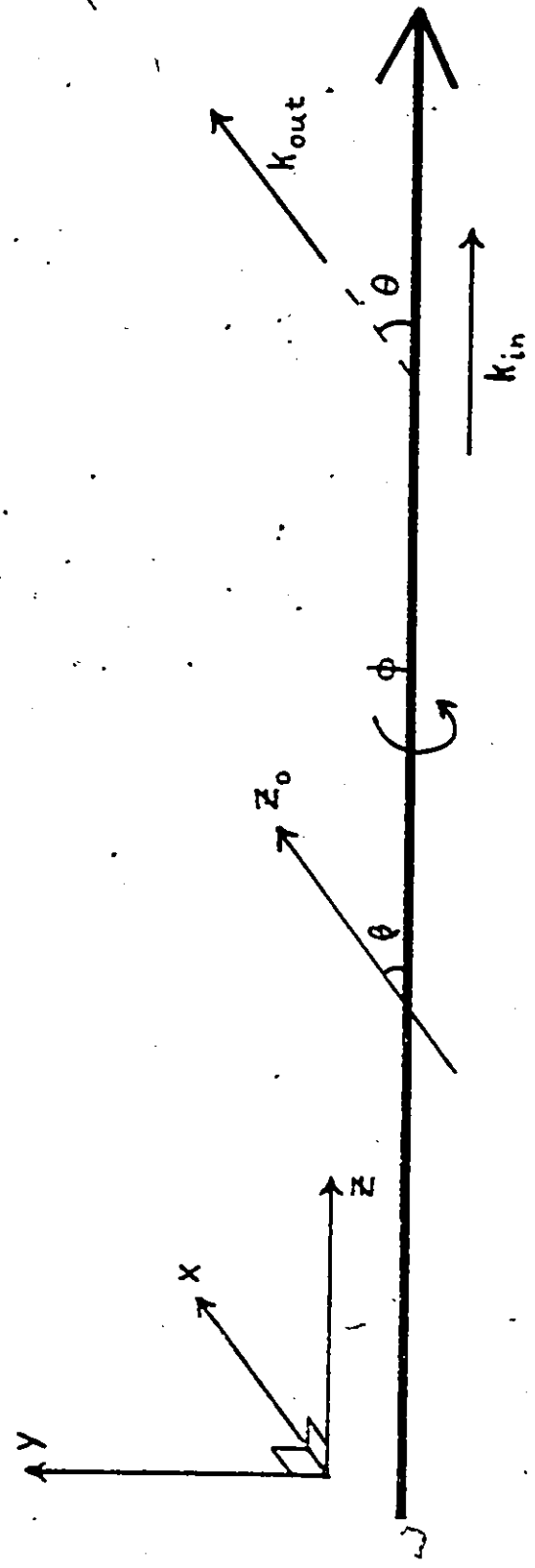
$$\begin{aligned} \sigma_{\text{pol}} = \sigma_{\text{un}} [ & 1 + 2i T_{11} \text{Re}(it_{11}) + T_{20} \text{Re}(t_{20}) \\ & + 2 T_{21} \text{Re}(t_{21}) + 2 T_{22} \text{Re}(t_{22}) ] \end{aligned} \quad (3.25)$$

If the beam is axially symmetric about the z-axis,  $t_{kq} = 0$  if  $q \neq 0$ . This is the case in the polarized ion source since the magnetic field defining the spin quantization axis is cylindrical with the beam as symmetry axis. Therefore only the  $t_{10}$  and  $t_{20}$  components of the beam are allowed. However, the other components can be created by rotating the spin axis. This occurs when the beam travels through the accelerator and the various magnets of the beam transport system. This rotation must be corrected as described in chapter 4.

The reference frame for polarized nuclear physics was standardized at an international conference in Madison, Wisconsin (In70). It is aptly named the Madison convention. The reader is referred to fig. 3.3 for a definition of the basis vectors.

Fig. 3.3 Madison Convention. Diagram of the reference frame normally used in polarization studies. The angles  $\theta$  and  $\phi$  defining the orientation of the spin quantization axis  $Z_0$  are shown.

# MADISON CONVENTION



$Z = k_{in}$  ;  $Y = k_{in} \times k_{out}$  ;  $X = Y \times Z$

$\theta =$  scattering angle

$\beta$  and  $\phi$  are the polar and azimuthal angles with respect to  $(X, Y, Z)$ .

Expressions for the beam moments  $t_{kq}$  as a function of the angles  $\beta$  and  $\phi$  as well as  $\hat{t}_{10}$  and  $\hat{t}_{20}$ , the values of  $t_{10}$  and  $t_{20}$  at the source, are given in ref.(Da70) on p.52. From these we can derive the following:

$$\text{Re}(it_{11}) = 1/\sqrt{2} \sin \beta \cos \phi \hat{t}_{10} \quad (3.26)$$

$$\text{Re}(t_{20}) = t_{20} = 1/2 (3 \cos^2 \beta - 1) \hat{t}_{20} \quad (3.27)$$

$$\text{Re}(t_{21}) = \sqrt{3/8} \sin 2\beta \sin \phi \hat{t}_{20} \quad (3.28)$$

$$\text{Re}(t_{22}) = -\sqrt{3/8} \sin^2 \beta \cos 2\phi \hat{t}_{20} \quad (3.29)$$

It is obvious that if  $\beta = 0$ , the only term that is not zero is  $t_{20}$ , and equation 3.25 becomes:

$$\sigma_{\text{pol}} = \sigma_{\text{un}} (1 + \hat{t}_{20} T_{20}) \quad (3.30)$$

Let  $t_{20}$  for an  $m=0$  ( $m=1$ ) beam of deuterons be  $t_0$  ( $t_1$ ), and  $\sigma_0$  ( $\sigma_1$ ) be the cross-section for this substate. We have:

$$\sigma_1 - \sigma_0 = \sigma_{\text{un}} (t_1 - t_0) T_{20} \quad (3.31)$$

$$\sigma_1 = \sigma_{\text{un}} (1 + t_1 T_{20}) \quad \sigma_1/t_1 = \sigma_{\text{un}} (1/t_1 + T_{20})$$

This, in conjunction with a similar equation for  $\sigma_0$  gives:

$$\sigma_1/t_1 - \sigma_0/t_0 = \sigma_{\text{un}} (1/t_1 - 1/t_0)$$

Hence:

$$\sigma_{\text{un}} = (\sigma_1 t_0 - \sigma_0 t_1) / (t_0 - t_1) \quad (3.32)$$

Equations 3.31 and 3.32 combine to give:

$$T_{20} = \frac{\sigma_1 - \sigma_0}{\sigma_0 t_1 - \sigma_1 t_0} \quad (3.33)$$

We have:

$$t_1 = (t_{20})_{m=1} = P / \sqrt{2}$$

$$t_0 = (t_{20})_{m=0} = -\sqrt{2} P$$

where  $P$  is the fraction of the beam that is polarized.

Finally:

$$T_{20} = \frac{\sigma_1 - \sigma_0}{P (\sqrt{2} \sigma_1 + \sigma_0 / \sqrt{2})} \quad (3.34)$$

This is the equation that will be used to calculate  $T_{20}$  from the yields with an  $m=0$  and an  $m=1$  deuteron beam.

It remains to find a method of monitoring the polarization  $P$  of the beam. This is done using a method developed at McMaster to resolve ambiguities in spin-parity assignments (KG75). The  $(\bar{d}, \alpha)$  reaction on an even-even target nucleus populates only unnatural parity states ( $\pi = (-1)^{J+1}$ ) if the  $\alpha$  particles are detected near zero degrees and the beam is in the  $m=0$  substate. Furthermore, and of more interest here, the tensor analysing power  $T_{20}$  of natural parity states is  $1/\sqrt{2}$  for a 100% polarized beam. This can be seen by setting  $\sigma_0=0$  and  $P=1$  in eq. 3.34. There is a known natural parity state in  $^{10}\text{B}$  at 3.59 MeV which is populated in the  $^{12}\text{C}(\bar{d}, \alpha)^{10}\text{B}$  reaction (KG75). Since the target contained carbon, this reaction also took place

during the experiment. A separate counter was used to monitor the cross-section for this state and the polarization could be found from equation 3.34:

$$P = \frac{\sigma_1 - \sigma_0}{T_{20} (\sqrt{2} \sigma_1 + \sigma_0 / \sqrt{2})}$$

$$P = \frac{\sigma_1 - \sigma_0}{\sigma_1 + \sigma_0 / 2} \quad (3.35)$$

In addition, the Quench Ratio (Q) method was used to check the polarization (Oh70). Q is the total current divided by the fraction of the beam that is unpolarized. The method for measuring Q will be explained in the next chapter. The polarization of the beam is deduced from the quench ratio as follows:

$$P = 1 - 1/Q \quad (3.36)$$

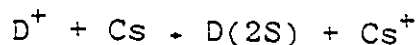
This equation is exact for the m=1 substate, and approximate for m=0 (Oh70). Since the first method described to monitor the polarization is more accurate than the quench ratio, the latter was used on-line to check stability only.

## Chapter 4: EXPERIMENTAL SET-UP

This chapter deals with the equipment and instrumentation involved in the study of the  $^1\text{H}(\vec{d}, \gamma)^3\text{He}$  reaction. The operation of the polarized ion source is described in section one. This is followed by a short description of the laboratory and the beam line. The arrangement of the detectors in the spectrograph is discussed in section three. The choice of position sensitive silicon detectors instead of a resistive wire gas counter is justified in section four. This is followed by a description of the electronics and the data acquisition system. Finally, the crucial point of precision steering is examined.

### 4.1 Polarized Ion Source.

The McMaster polarized ion source is of the Lamb shift type (Mc76, ML68). It is schematically represented in fig. 4.1. A standard duoplasmatron source produces a beam of positive deuterium ions. These undergo a charge exchange reaction in a caesium vapour canal:



At 500 eV, approximately 30% of the beam is in the atomic 2S state of deuterium, the rest being in the neutral ground state or remaining in ionic form.

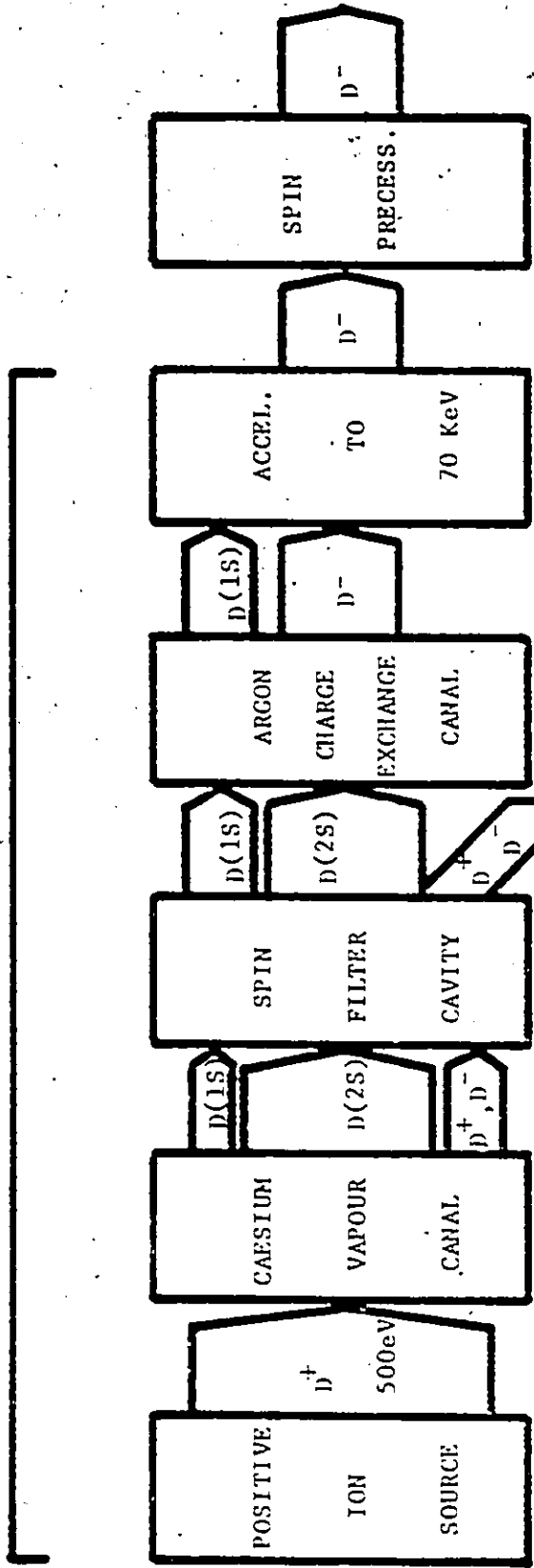
Fig. 4.1 Schematic of the polarized ion source. The magnetic substate is selected in the spin filter cavity.

(ref. Mc76)

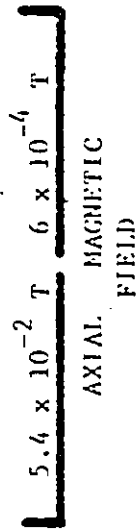


# POLARIZED ION SOURCE SCHEMATIC

DECK COMPONENTS



Note: The arrow sizes are not proportional to the beam species division.



The beam enters the spin filter cavity where the nuclear magnetic substate is selected. The 2S and 2P levels are split by the Lamb shift. If an external magnetic field is applied, two further degeneracies are lifted. The levels split according to their atomic magnetic substate  $m_J$ , and their nuclear magnetic substate  $m_I$ . This is shown in fig. 4.2. The 2S-state is metastable ( $t_{1/2} = 1/7$  s.) since it cannot decay to the ground-state by one photon emission. The 2P levels, however, have a negligible half-life since they can decay by an electric dipole transition. It is interesting to note that the energy of the 2S ( $m_J = -1/2$ ) levels, labelled s, is reduced to the point where they are degenerate with the 2P ( $m_J = +1/2$ ) levels, labelled e, at  $B = 0.0575$  T. A small transverse DC electric field  $\vec{E}_T$  can couple these states allowing the s levels to decay to the ground-state, leaving only the a states. The latter are coupled to the e levels by an R.F. electric field parallel to the quantization axis. For specific values of the magnetic field, with  $\vec{E}_T$  and the R.F. field constant, a resonance condition is established leaving particles in only one substate  $m_I$ ; the other two levels are quenched to the ground-state via the e levels. A graph of beam current versus magnetic field is plotted in fig. 4.3.

We now make a short digression to explain how the quench ratio  $Q$  is measured.  $Q$  is the ratio of the total beam current  $I_T$  to the unpolarized current  $I_{un}$ .  $I_T$  is measured with the magnetic field set on a resonance. To

Fig. 4.2 Diagram of the  $2S_{1/2}$  and  $2P_{1/2}$  levels of deuterium which are split by a magnetic field. The desired substate is obtained through a resonance condition produced by an axial magnetic field, a transverse electric field, and an RF electric field along the quantization axis (ref.Mc76).

# DEUTERIUM BREIT-RABI DIAGRAM

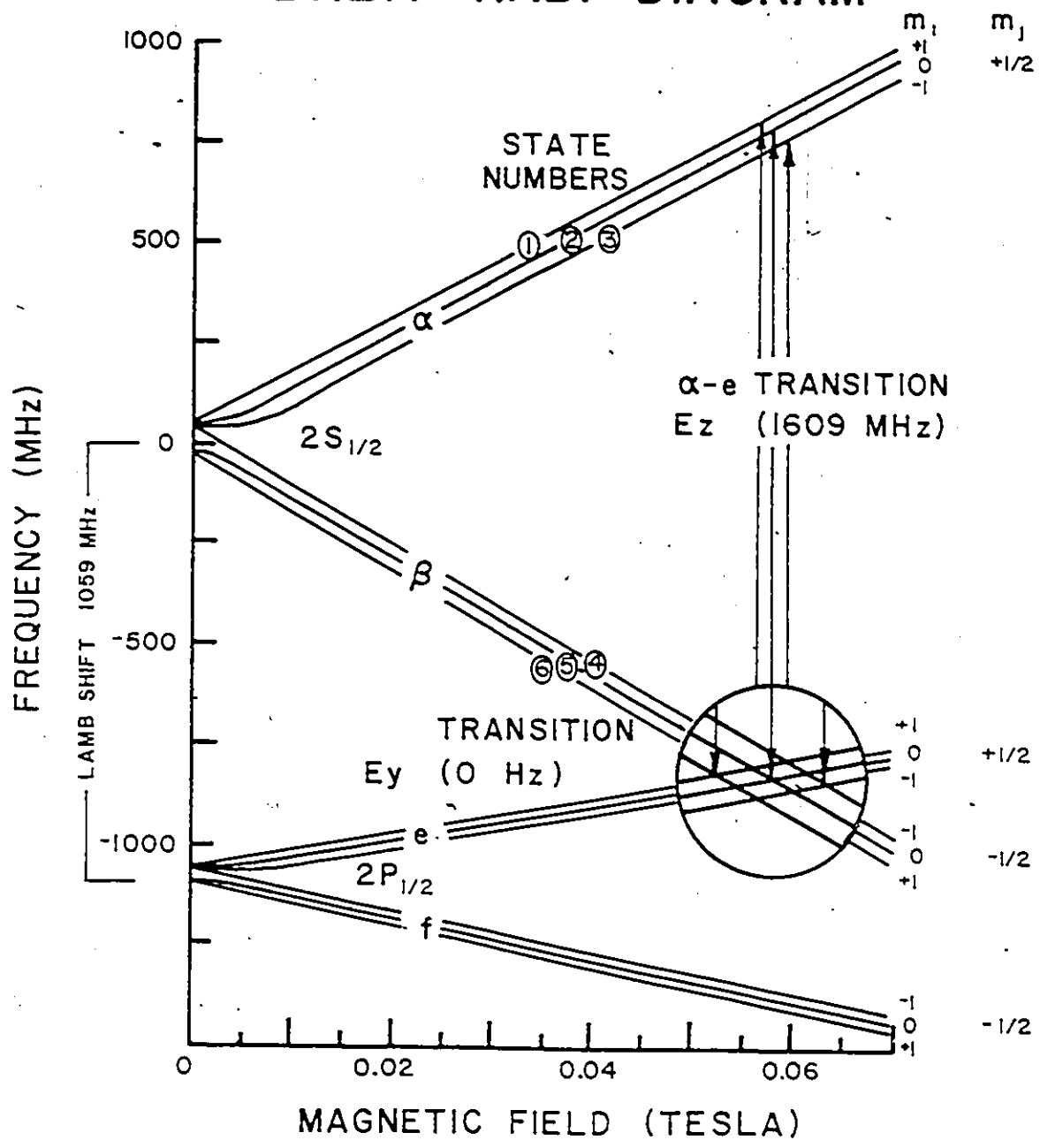
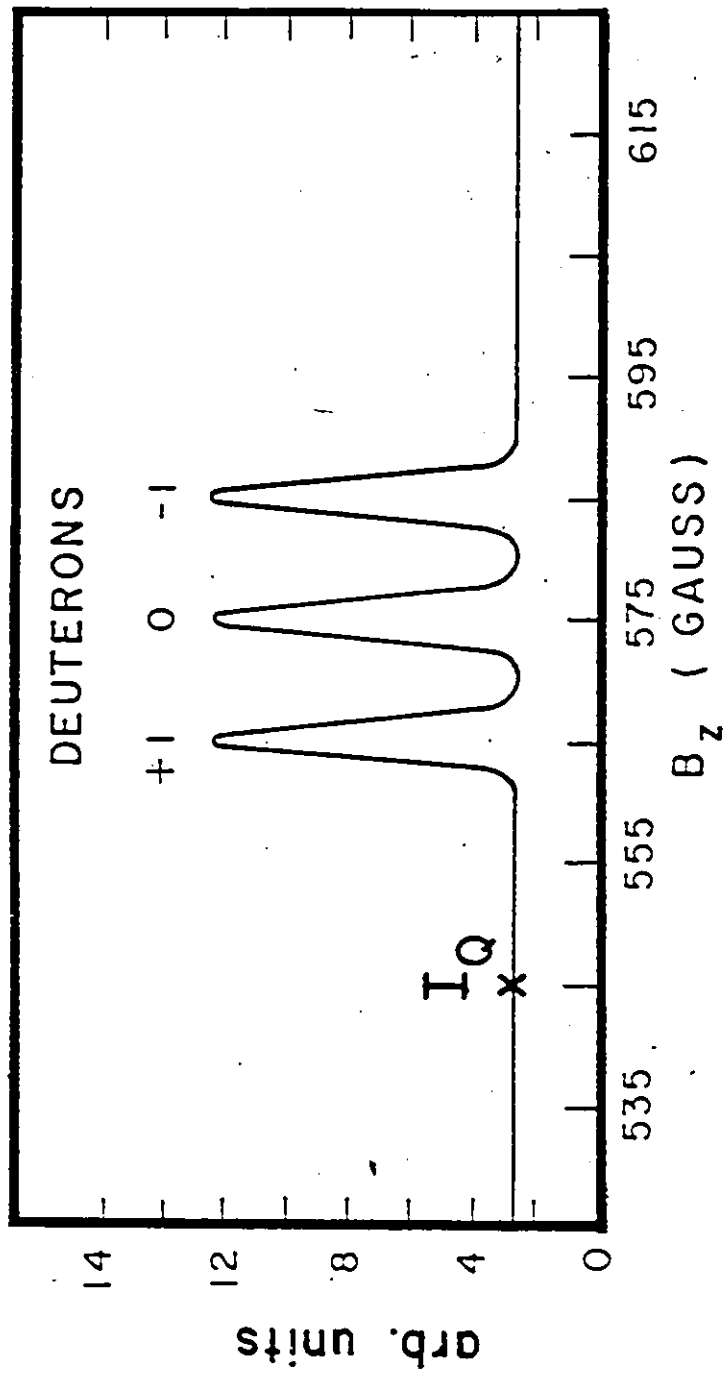


Fig. 4.3 Spin filter output current as a function of magnetic field  $\vec{B}$ . The three substates are well separated at  $B = 565$  G,  $575$  G, and  $585$  G for  $m = +1$ ,  $0$ , and  $-1$  respectively. The value of the field when measuring the unpolarized component of the beam to determine the quench ratio  $Q$ , is shown on the graph ( $I_Q$ ). (ref. Mc76)

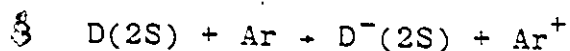
# SPIN FILTER OUTPUT CURRENT



obtain  $I_{un}$ , the field is lowered to a point far off resonance (fig.4.3). For this field, the three states are equally populated and the unpolarized component of the beam can be measured.

An added feature of the spin filter is that the transverse electric field deflects the extraneous charged particles, therefore removing an unpolarized component from the beam.

The neutral particles undergo a second charge exchange reaction in an argon canal:



making them suitable for injection into the accelerator. This reaction occurs at a much higher rate than the same reaction for the ground-state  $D(1S)$ ; this also contributes to the suppression of the unpolarized components of the beam. There is a final acceleration stage to 70 keV, as well as a spin axis re-alignment achieved in a Wien filter. As mentioned above, this correction is necessary to take into account the various magnetic fields which deflect the beam before it reaches the target.

Before calculating this correction, a brief description of the beam transport system is required.

#### 4.2 Beam Transport System.

The beam is accelerated to 19.8 MeV by a model FN Tandem Van de Graaff accelerator. This machine was upgraded in 1982. Spiral inclined field tubes were installed, and

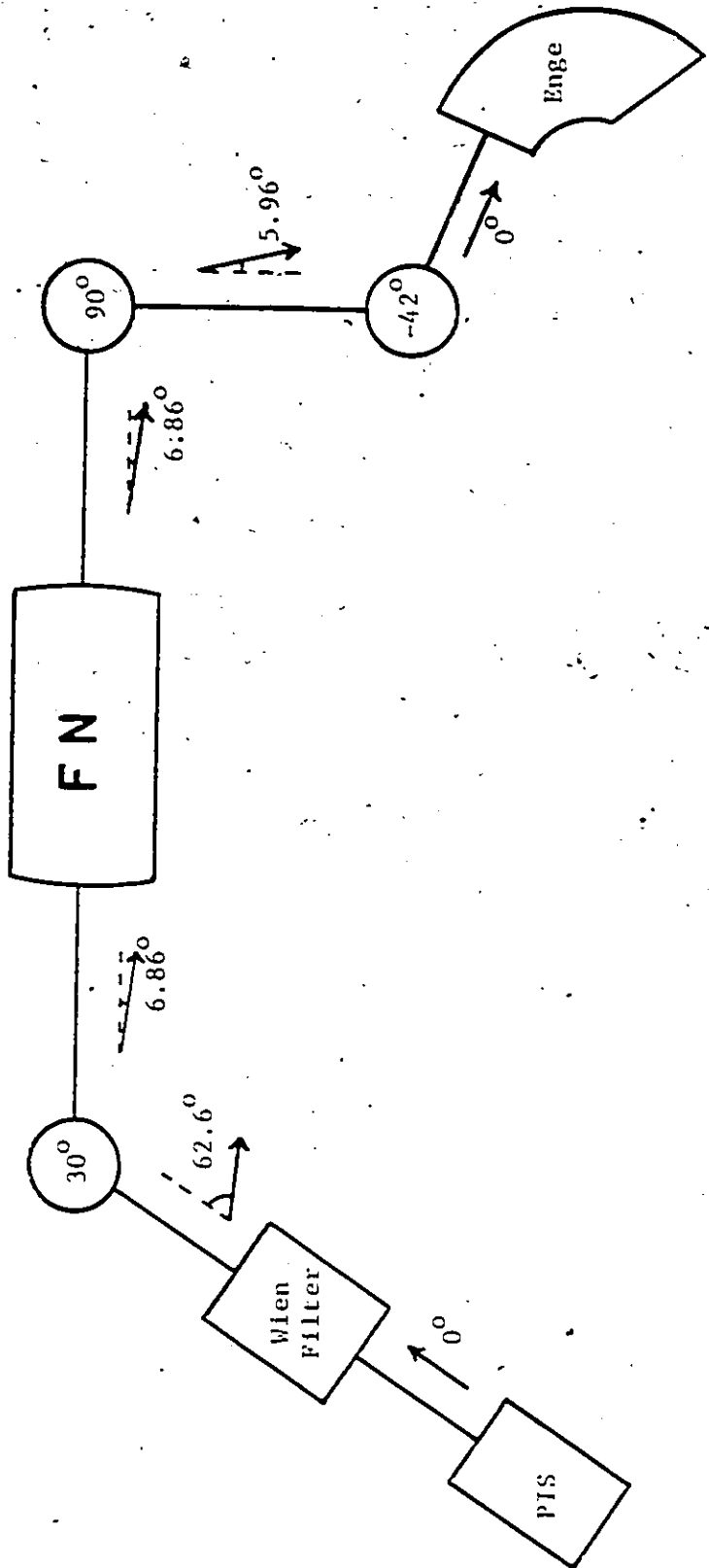
the standard belt charging system was replaced by a pellet inductive charging system manufactured by National Electrostatics Corporation. The Pelletron makes the charging of the terminal much smoother than with a belt while the new tubes help to prevent sparks by reducing instabilities in the field gradient. These modifications are important since it is only with these improvements that a terminal voltage of 10 MV can be achieved to obtain a beam energy of 20 MeV for deuterons. The correct energy of the deuterons is determined with a  $90^\circ$  analyzing magnet. A further bend of  $42^\circ$  is produced by a second magnet which selects the magnetic spectrograph beam line. This is summarized in fig. 4.4.

To measure the tensor analysing power  $T_{20}$  of a reaction, the quantization axis of the deuterons must be along the beam direction. This condition is met in the source because the field defining the quantization axis in the argon canal is axial and along the beam. However, as seen in fig. 4.4, the beam is deflected three times before it strikes the target. Hence, the quantization axis will not have the correct orientation unless it is pre-rotated by an amount which compensates for these deflections. The situation is complicated by the fact that the spin axis does not rotate by the same amount as the beam; this is due to Larmor precession. For deuterons, the spin axis rotates 0.357 times as fast as the beam. This rotation is in the same direction for positive ions, and in the opposite



Fig. 4.4 Spin Axis Alignment. Because the spin axis and the beam rotate differently, the spin must be pre-rotated by  $62.57^\circ$  in a Wien filter. The angles shown are between the quantization axis and the beam.

# SPIN AXIS ALIGNMENT



direction for negative ions. From fig. 4.4, we see that the beam rotates by  $(30^\circ + 90^\circ - 42^\circ) = 78^\circ$ . The spin axis deflects by  $0.857 (-30^\circ + 90^\circ - 42^\circ) = 15.43^\circ$ . Therefore, the quantization axis must be pre-rotated by  $62.57^\circ$  in the Wien filter. This is also shown in fig. 4.4.

### 4.3. Detector Configuration.

An Enge split-pole magnetic spectrograph was used to momentum analyze the outgoing particles in the  $^1\text{H}(\vec{d}, \gamma)^3\text{He}$  and  $^{12}\text{C}(\vec{d}, \alpha)^{10}\text{B}$  reactions. A charged particle ( $q = eZ$ ) travelling with velocity  $v$  in a magnetic field undergoes a force  $\vec{F}_M = eZ \vec{v} \times \vec{B}$ . If the field is perpendicular to the velocity,  $F_M = eZvB$ , the trajectory is circular since the force is always at right angles to the velocity. Hence, the particle also feels a centrifugal force  $F_C = mv^2/\rho$ . Equating  $F_M$  and  $F_C$ , we obtain:

$$p = (eZB) \rho \quad (4.1)$$

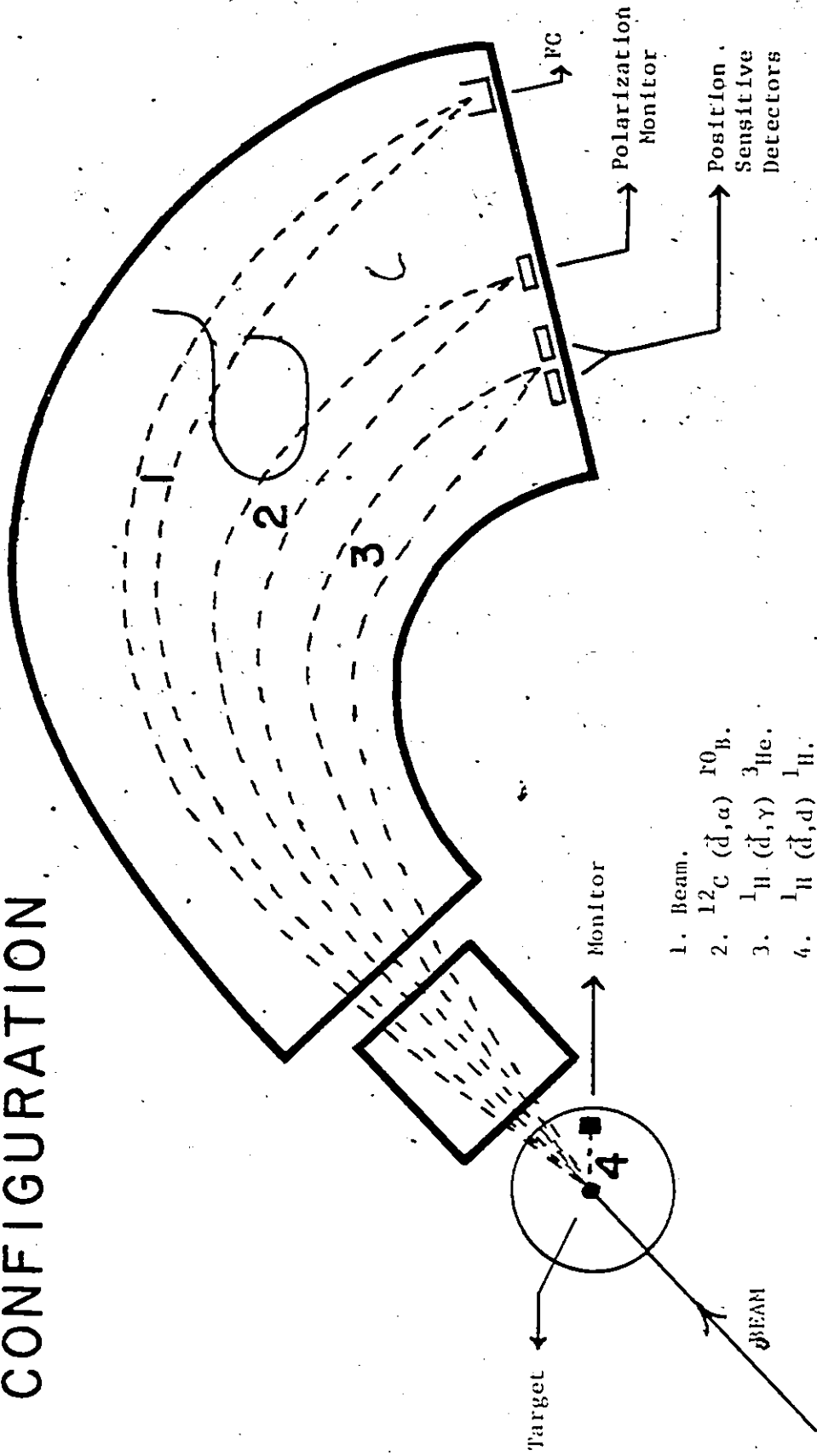
where  $p$  is the momentum of the particle. For known field and charge, the momentum can be determined by measuring  $\rho$ . More details will be given in chapter 5 in the section on calibration.

The detection system is shown in fig. 4.5. The  $^3\text{He}$  particles were focussed at the low radius of curvature ( $\rho$ ) end of the focal plane while the beam was collected in a Faraday cup at the high  $\rho$  end. The  $^3\text{He}$  detectors are described below.

The targets used were polyethylene films approxi-

Fig. 4.5 Detector Configuration. Diagram of the placement of the detectors used in the experiment. The beam was collected at the high  $\rho$  end of the focal plane by a Faraday cup. The  $^3\text{He}$  particles were focussed at the low  $\rho$  end onto two position sensitive silicon detectors. The  $^{12}\text{C}(\bar{d},\alpha)^{10}\text{B}$  reaction was used to monitor the beam polarization, while the  $^1\text{H}(\bar{d},d)^1\text{H}$  reaction was used to normalize the runs.

# DETECTOR CONFIGURATION



mately  $100 \mu\text{g}/\text{cm}^2$  thick. Since this is a hydrocarbon, it contains both hydrogen and carbon. Hence the  $^{12}\text{C}(\vec{d},\alpha)^{10}\text{B}$  reaction occurs simultaneously with the capture reaction. As explained in chapter 3, this is important to determine the polarization of the beam. The  $\alpha$  particles from this reaction were detected on the focal plane between the  $^3\text{He}$  and the Faraday cup by a position sensitive silicon detector (fig. 4.5).

The different runs were normalized using elastic deuteron scattering from hydrogen,  $^1\text{H}(\vec{d},d)^1\text{H}$ . The deuterons were monitored with a silicon surface barrier detector in the scattering chamber (fig. 4.5). An angle of  $21^\circ$  was chosen because the tensor analysing power of this reaction is small and does not vary much with angle for  $\theta = 21^\circ$  ( $T_{20} < 0.01$ ) (KG80). This eliminated the need to correct for polarization effects in the monitor.

As a final note about the spectrograph, the entrance apertures were left wide open, ( $V = 1.41 \text{ cm}$ ,  $H = 4.23 \text{ cm}$ , corresponding to an angular acceptance of  $4.3^\circ$ ) to reduce scattering and to allow the full angular range of  $^3\text{He}$  particles to be analyzed.

#### 4.4 Detectors.

To obtain an angular distribution for the capture  $\gamma$ -rays, the energy of the  $^3\text{He}$  particles must be determined. As we have just seen (eq. 4.1), the momentum of these particles is related to their radius of curvature and hence

to their position on the focal plane:

$$p = (eZB) \rho + E = p^2/2m = (eZB)^2/2m \rho^2 \quad (4.2)$$

Several types of detectors can be used to measure this position. Two of them are described here.

A resistive wire gas ionization counter was used initially. This consists of a 25 cm long chamber filled with a mixture of 90% argon and 10% methane. A thin nichrome wire, with homogeneous resistance, runs through this chamber (see fig. 4.6). A voltage of 1 kV is applied to this wire. Particles enter the counter through a very thin aluminized mylar window which does not degrade the energy significantly. They ionize the gas and the resulting charge is collected on the wire. Since the resistance is homogeneous, the charge collected at each end of the wire is inversely proportional to the distance. The position is determined from the following relation:

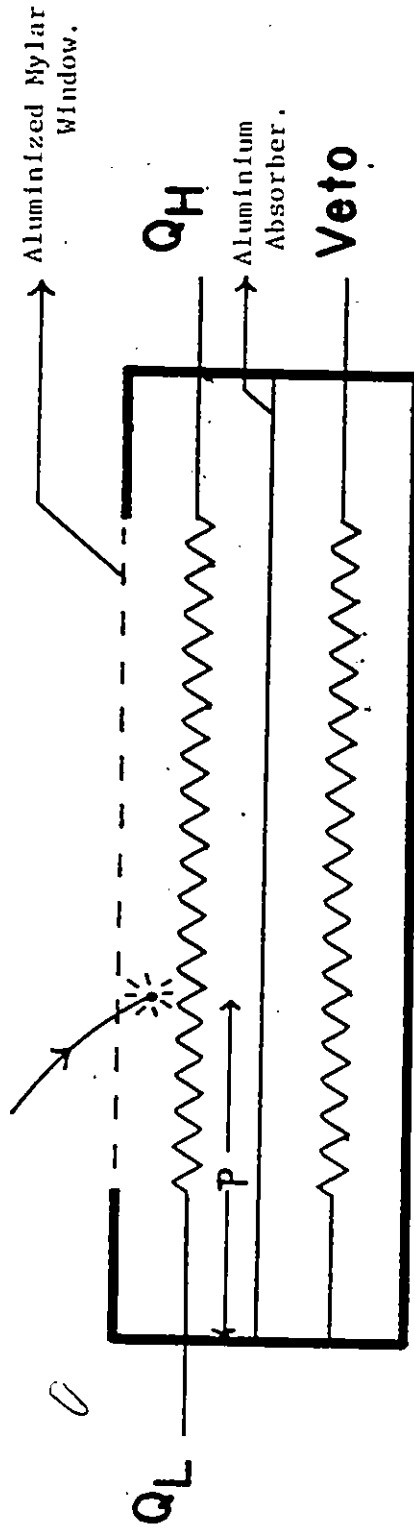
$$d_L = Q_H / (Q_H + Q_L)$$

where  $d_L$  is the distance from the end of the counter corresponding to low radius of curvature, and  $Q_H$  and  $Q_L$  are the charges collected at the high  $\rho$  and low  $\rho$  ends respectively (fig. 4.6). The position resolution is approximately 1.5 mm. Many types of particle enter the detector. Particle discrimination is achieved by considering the total energy lost  $\Delta E$  in the counter ( $\Delta E = Q_H + Q_L$ ):

Fig. 4.6 Resistive Wire Detector. Diagram of the two chambers of the gas ionization detector first used for this experiment. The position and energy loss information is derived from  $Q_L$  and  $Q_H$  the charges collected at the low  $\rho$  and high  $\rho$  ends of the resistive wire respectively. The aluminium absorber stops all but the deuterons and the back counter is used in anti-coincidence.



# RESISTIVE WIRE DETECTOR



$$P = Q_H / (Q_H + Q_L)$$

$$\Delta E = Q_L + Q_H$$

$$\Delta E \propto Z^2/v^2 = mZ^2/E \quad (\text{see Se77})$$

From eq. 4.2:  $E \propto Z^2/m$

Hence:  $\Delta E \propto m^2$  (4.3)

Thus we have:

$$\Delta E(\alpha) / \Delta E(d) \approx 4.0 \quad ; \quad \Delta E(^3\text{He}) / \Delta E(d) \approx 2.25$$

and the  $^3\text{He}$  particles are between the deuterons and the  $\alpha$  particles in the  $\Delta E$  spectrum. It should be noted that the inelastic deuteron peak is by far the largest in the spectrum. This is a problem because we require good  $\Delta E$  resolution to obtain a clean position spectrum for the  $^3\text{He}$  particles. The situation can be improved by the use of a second chamber separated from the first by an aluminium foil. The thickness of this foil is chosen to stop the  $^3\text{He}$  particles but not the deuterons. This is possible because the latter lose less energy (eq. 4.3). They are detected by a second wire and this signal is used in anticoincidence thus discriminating against deuterons. The resulting  $\Delta E$  spectrum is shown in fig. 4.7. Although the  $^3\text{He}$  peak is quite visible, the background in the position spectrum, caused by the tail of the deuteron peak, is too high to be acceptable. A different solution must be found.

It was decided to use two position sensitive silicon detectors. As discussed below, the main advantage of these detectors is their particle discrimination. They produce

Fig. 4.7 .  $\Delta E$ : Resistive Wire. Energy loss spectrum for the resistive wire detector, showing the  $^3\text{He}$  peak between the deuterons and the  $\alpha$ -particles.

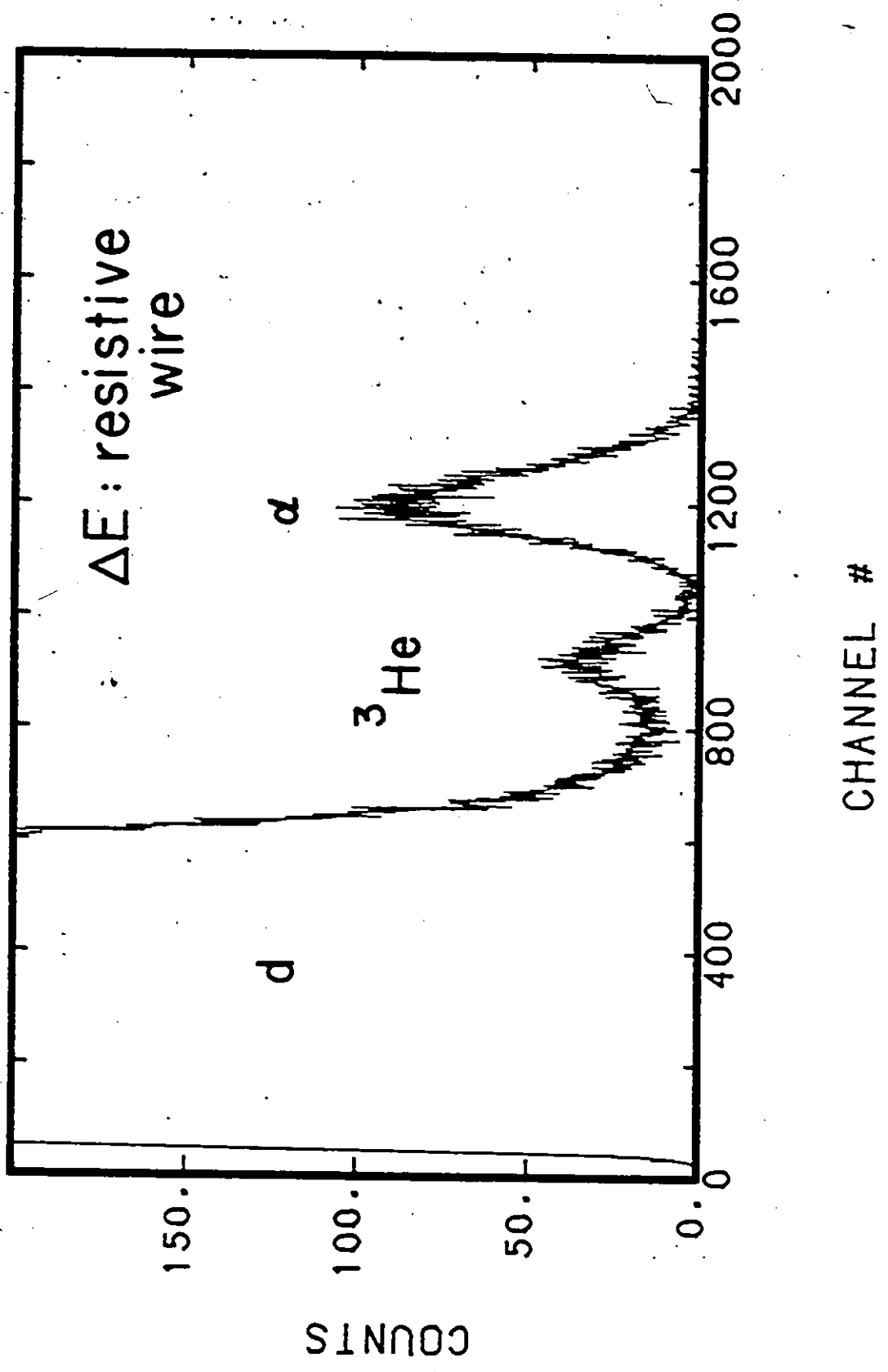
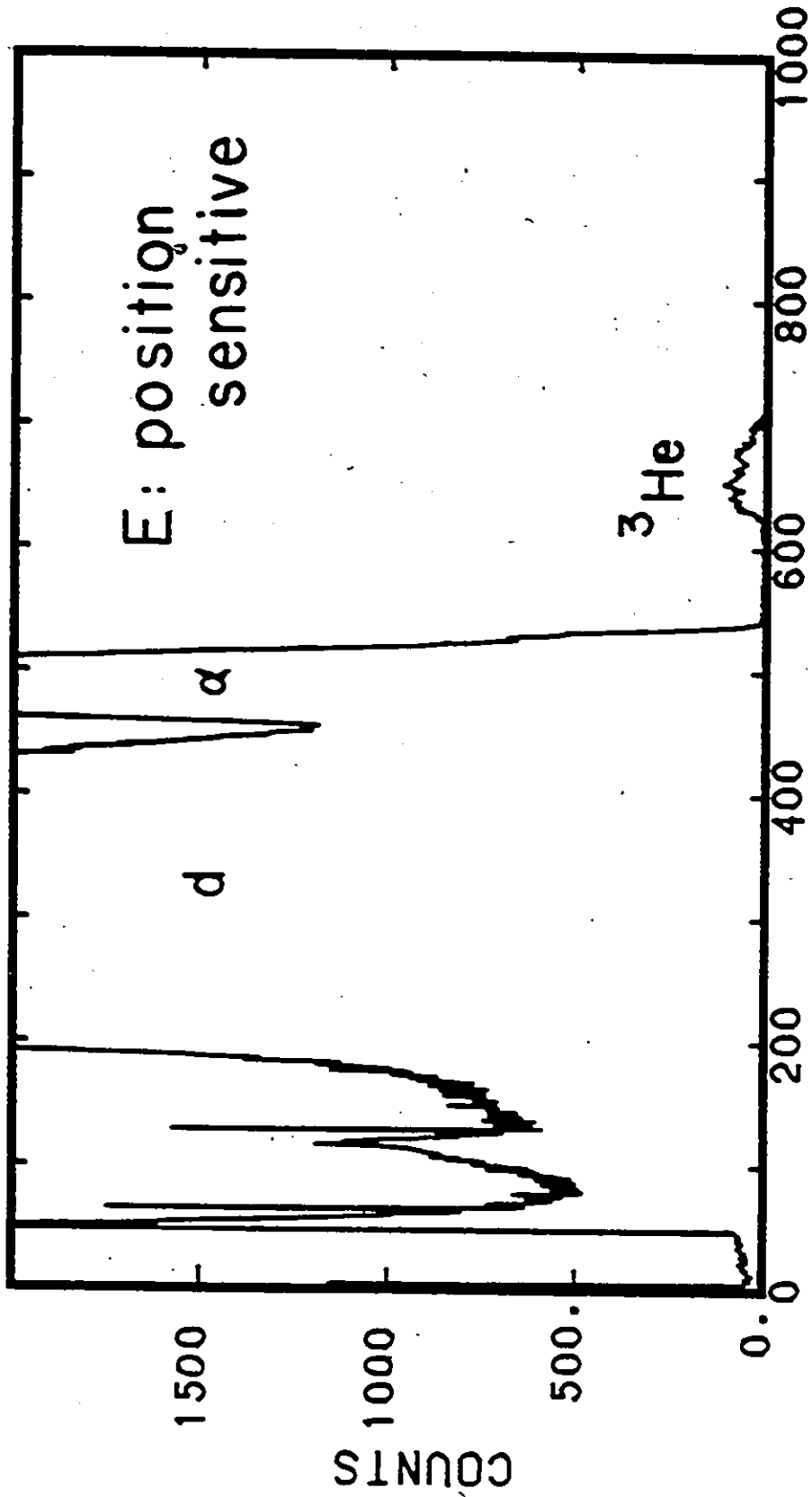


Fig. 4.8     E: Position Sensitive Detector.     Energy loss  
spectrum for the position sensitive silicon detectors  
showing a well resolved  $^3\text{He}$  peak.



two signals. The first is proportional to the energy deposited by the particles, while the second is proportional to the product of energy and position. The latter signal is taken off the back surface of the detector which works in much the same way as the resistive wire counter, except that one end is grounded and the signal is taken off the other. The position and energy resolution of these counters are 0.5 mm and 55 keV respectively although our resolution was worse due to target effects. The dimensions of the active volume for both detectors are: 45 mm x 8 mm x 100  $\mu$ . They are thick enough to stop all the particles produced in the experiment except protons which do not deposit enough energy to be a problem. Referring to equation 4.2, we have:

$$mE / Z^2 = \text{constant}$$

for a given radius of curvature. Therefore:

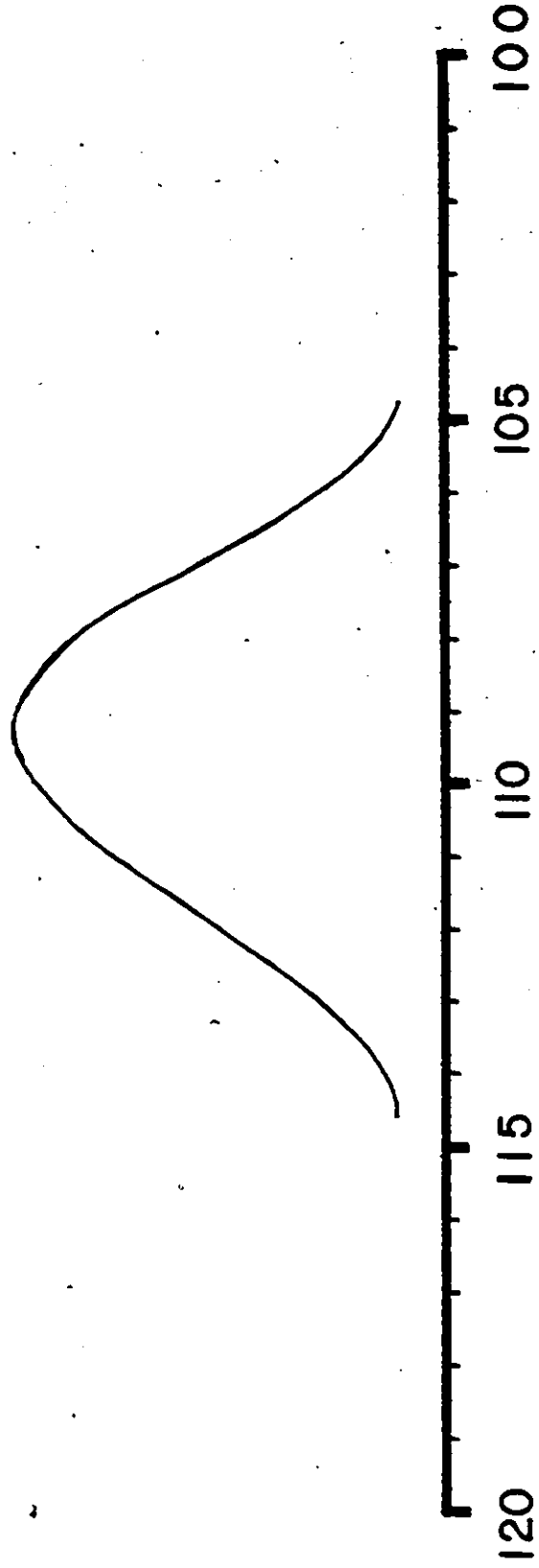
$$E(\alpha) / E(d) = 2 \quad ; \quad E(^3\text{He}) / E(d) = 8/3$$

Unlike for the resistive wire counter, the  $^3\text{He}$  particles have the highest energy in the spectrum which is shown in fig. 4.8. They are well resolved from the deuterons and  $\alpha$  particles resulting in a much cleaner position spectrum. The only drawback to these detectors is their length. The distribution of the  $^3\text{He}$  particles is calculated to be approximately 10 cm along the focal plane. However, the solid-state counters are only 4.5 cm long and it is not

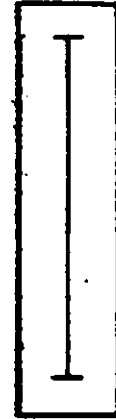
Fig. 4.9 Counter Positions. Diagram showing the placement of the position sensitive detectors with respect to the  $^3\text{He}$  distribution along the focal plane. The scale is for D in cm. The experiment was done in two bights in order to collect the full range of the  $^3\text{He}$  particles. The sensitive area of the detectors is denoted by the line in each box.



# COUNTER POSITIONS



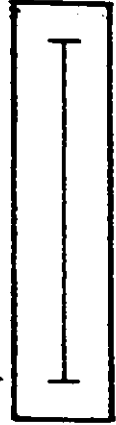
det. 1



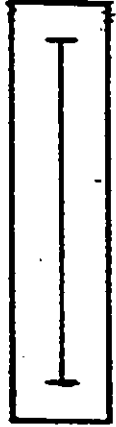
det. 2



det. 1



det. 2



POS. 1

POS. 2

possible to detect the full range at once. The experiment was done in two stages, with the detectors positioned as in fig. 4.9. The numbers shown are values of  $D$ , the distance along the focal plane from the high  $p$  end. Rather than varying the magnetic field in the spectrograph, the detectors were physically moved in order not to change the parameters affecting the  $^3\text{He}$  distribution.

#### 4.5 Electronics.

Schematics of the electronics used to process the signals from the solid-state detectors are shown in figs. 4.10 and 4.11. Separate coincidence circuits are required for each position sensitive detector. The two logic signals are "ORed" together and gate the first four analog to digital converters (ADC) which are read simultaneously by the computer (channel B). ADC's 4 and 5 are used for the monitor and the polarization monitor and are multiplexed into channel A. The software detects which ADC has fired by looking at the top four bits of the event word. The ADC - computer interface is done through an in-house ADC controller and a CAMAC crate. The computer used for both on-line data acquisition and off-line analysis was a VAX 11-750. The data acquisition software was written in EVAL (Event Analysis Language). A spectrum for the total energy loss ( $E$ ) is accumulated directly. The  $\text{Exp}$  value is divided by  $E$  to obtain a position spectrum. A two-dimensional  $E$  vs  $P$  spectrum is also provided.

Fig. 4.10 Electronics for the  $^3\text{He}$  detectors. The notation is as follows:

AMP - Amplifier.

LGS - Linear Gate and Stretcher.

TSCA - Timing Single Channel Analyser.

COINC - Coincidence Unit.

GDG - Gate and Delay Generator.

LSD - Logic Shaper and Delay.

ADC - Analog to Digital Converter.

The output of the LSD is used to gate ADC's 0, 1, 2, and 3 which are read simultaneously by the computer on channel B.

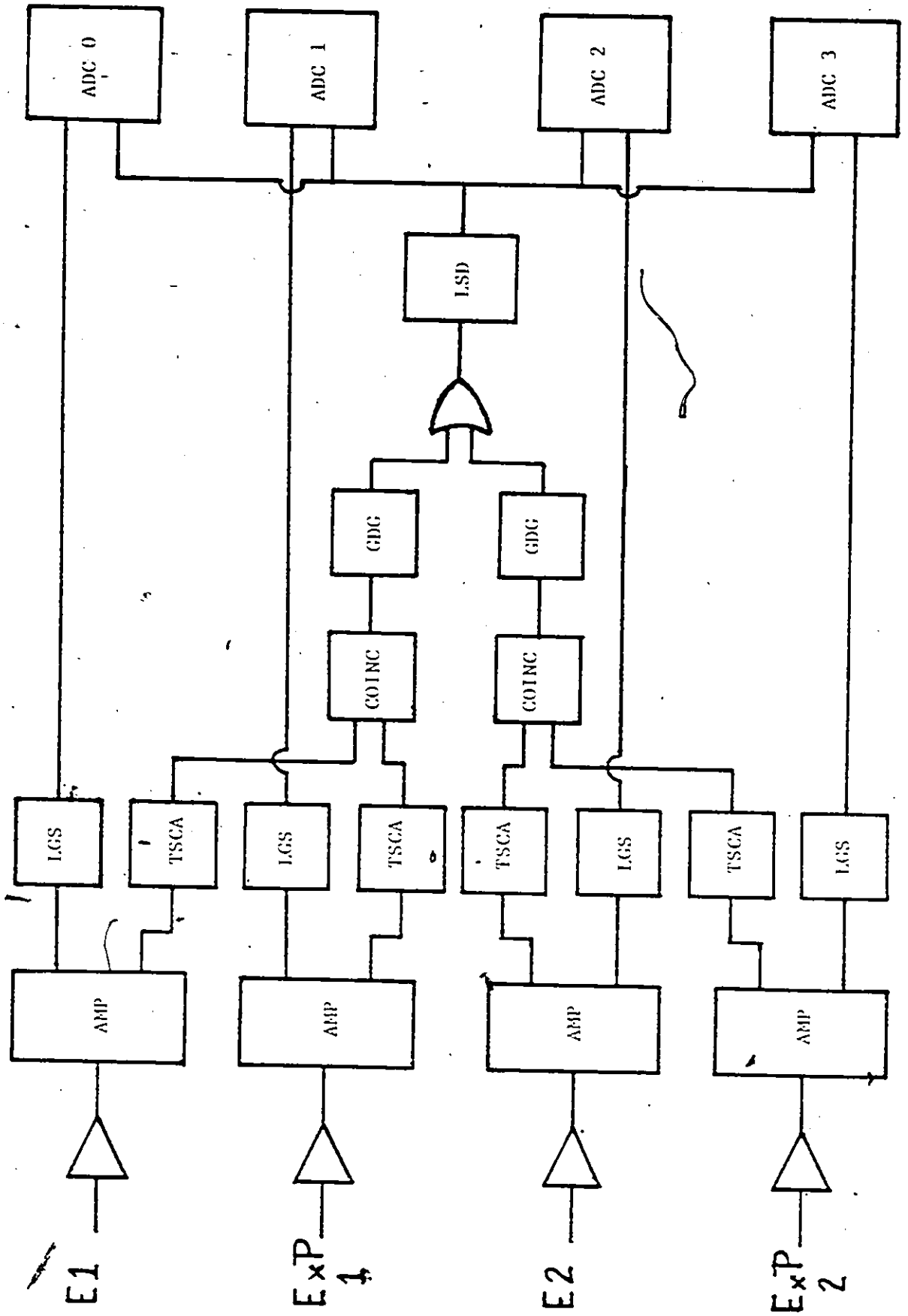
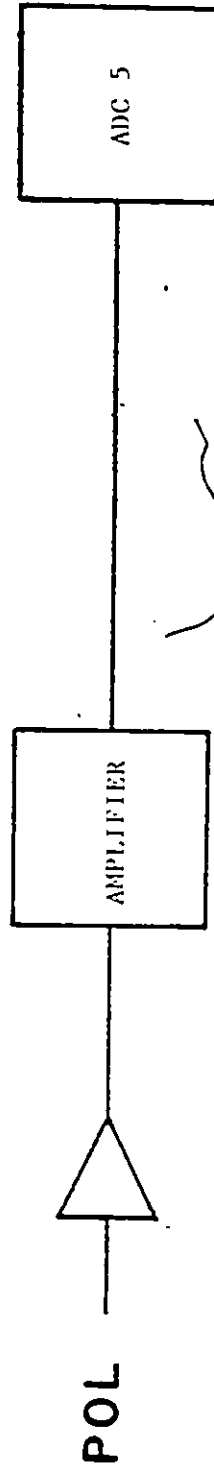
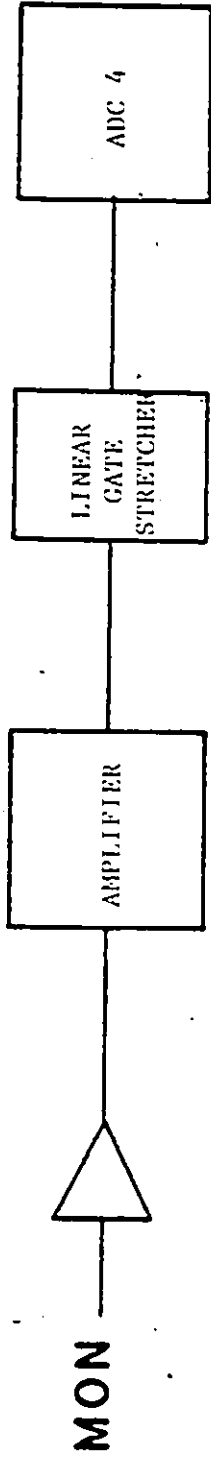


Fig. 4.11 Monitor Electronics. The monitors are input to ADC's 4 and 5 which are multiplexed into channel A of the computer interface.



Furthermore, gates can be set on both energy and E vs P to obtain position spectra for a specific particle type. Finally, all events were recorded on magnetic tape to allow for off-line analysis where the energy gates could be set precisely.

#### 4.6 Beam Steering.

Since the particles were being detected near zero degrees, it was important to have a well focussed beam to minimize multiple small angle elastic and inelastic scattering which might have been enough to mask the  $^3\text{He}$  distribution. To this end, the beam line was re-aligned and beam monitors were installed. Although these helped during diagnostic runs, a quartz viewer was more useful during the experiment proper.

Drawing on previous experience with scattering problems in  $(d,\alpha)$  reactions near zero degrees, it was decided to remove the Enge target chamber slits. A 1.5 mm by 3 mm aperture was placed in the target ladder and the current on it was minimized ( $< 1\text{nA}$ ). It was then removed. As a final step, the signals from the position sensitive detectors were observed on an oscilloscope while making small adjustments to the beam focussing. The count rate, determined by the intensity of the trace and due mostly to scattered deuterons, was minimized. This procedure gave a well resolved  $^3\text{He}$  peak and resulted in a low background in the position spectrum.

## Chapter 5: DATA ANALYSIS AND RESULTS.

This chapter explains in detail how values of  $T_{20}$  were extracted from the data. Section one gives experimental details. Sections two and three deal with the monitors and questions of normalization and beam polarization. This is followed by a description of the calibration procedure for the position sensitive detectors in section four and a study of the resolution in section five. The formula for calculating the error in  $T_{20}$  is derived in section six. Results for  $T_{20}$  are given in the final section.

### 5.1 Experimental Details.

Two separate experiments were done four months apart and gave the same results. The values of  $T_{20}$  were averaged, thereby reducing the error.

In the first experiment, six pairs of runs were done in the  $m=0$  and  $m=1$  substates of the beam with the detectors in position one, while seven pairs were done for position two. The average duration of each run was 1 1/2 hours to avoid problems associated with long term drifting in the polarized ion source. The beam current was approximately



30 nA at the beginning of the experiment dropping to about 20 nA at the end.

In the second experiment, four pairs of runs were carried out for position one and three pairs for position two. Due to the stability of the source in the first experiment, the duration of the runs was increased to 2 1/2 hours. The average beam current was 27 nA.

### 5.2 Monitor Detector.

A spectrum for the monitor detector is plotted in fig. 5.1. The  $^{10}\text{B}$  peaks come from the  $^{12}\text{C}(\text{d}, \alpha)^{10}\text{B}$  reaction. As mentioned earlier, elastically scattered deuterons from hydrogen were used to normalize the different runs. The correction factors thus determined agreed with the normalization using the Faraday cup to integrate the beam current (less than 1% difference).

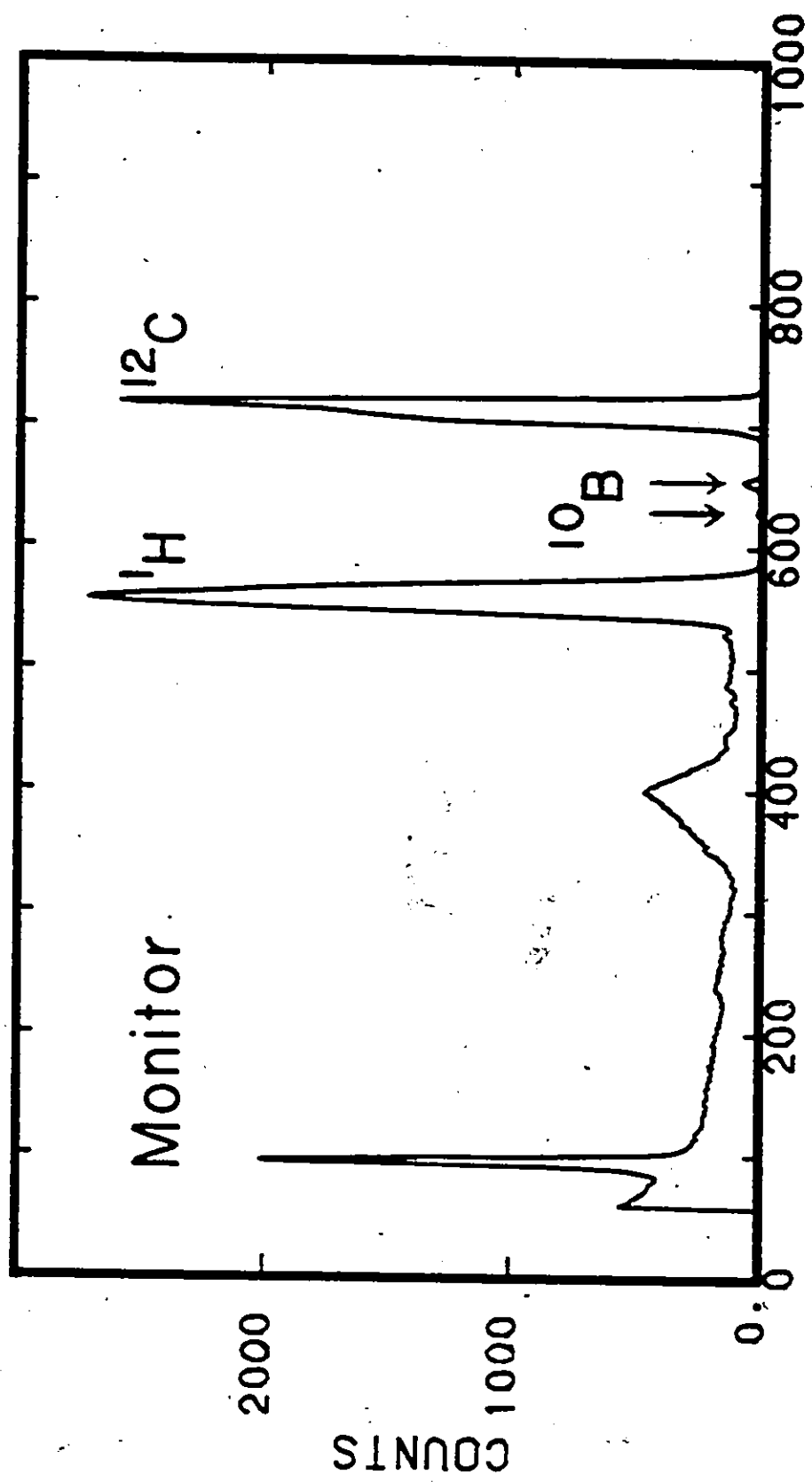
### 5.3 Polarization Monitor.

It was found that it is unnecessary to use a position sensitive detector to monitor the polarization because only the  $2^+$  excited state of  $^{10}\text{B}$  was present in the spectrum. Only the energy signal was used, thereby simplifying the electronics and the data acquisition programs.

Recalling equation 3-35, we have:

$$p = \frac{\sigma_1 - \sigma_0}{\sigma_1 + \sigma_0/2}$$

Fig. 5.1 Monitor Spectrum. Spectrum from the surface barrier detector mounted in the target chamber. The peak from the  ${}^1\text{H}(\vec{d},d){}^1\text{H}$  reaction was used to normalize the runs. The peak marked  ${}^{12}\text{C}$  is from the elastic scattering of deuterons from carbon, while the  ${}^{12}\text{C}(\vec{d},\alpha){}^{10}\text{B}$  peaks are denoted  ${}^{10}\text{B}$ .



CHANNEL #

where  $\sigma_1$  and  $\sigma_0$  are normalized to monitor counts. If  $R = \sigma_0/\sigma_1$ , this can be written:

$$P = \frac{1 - R}{1 + R/2} \quad (5.1)$$

This is the equation used to calculate the polarization of the beam.

We now calculate the error in P.

$$R = \sigma_0/\sigma_1 \quad \rightarrow \quad \left(\frac{\Delta R}{R}\right)^2 = \left(\frac{\Delta\sigma_0}{\sigma_0}\right)^2 + \left(\frac{\Delta\sigma_1}{\sigma_1}\right)^2$$

If we consider purely statistical errors,  $\Delta\sigma_i = \sqrt{\sigma_i}$  and:

$$\left(\frac{\Delta R}{R}\right)^2 = 1/\sigma_0 + 1/\sigma_1$$

from which we can derive:

$$(\Delta R)^2 = \sigma_0(\sigma_0 + \sigma_1) / \sigma_1^3 \quad (5.2)$$

Now:

$$P = \frac{1 - R}{1 + R/2}$$

The error in P is:

$$(\Delta P)^2 = (\delta P/\delta R)^2 (\Delta R)^2$$

Calculating this derivative, we get:

$$(\Delta P)^2 = \frac{9 (\Delta R)^2}{4 (1 + R/2)^4} \quad (5.3)$$

Substituting for  $(\Delta R)^2$  in equation 5.3, we obtain an expression for the error in the polarization as a function of the cross-section:

$$\Delta P = \frac{3}{2} \left( \frac{\sigma_0 (\sigma_0 + \sigma_1)}{\sigma_1^3} \right)^{1/2} \left( 1 + \frac{\sigma_0}{2\sigma_1} \right)^{-2} \quad (5.4)$$

The average value of P was 0.58 for the first experiment and 0.56 for the second. The quench ratio method gave corresponding values of 0.70 and 0.65. Previous experience has shown that the quench ratio over-estimates the polarization by as much as 0.10.

Equation 5.4 gives a negligible error for the polarization of each individual run ( $<0.01$ ). However, P varied by as much as 0.05 from the beginning of the experiment to the end, the quality of the beam deteriorating with time. Since, as will be shown later, the error in the polarization makes only a small contribution to the error in  $T_{20}$ , and taking into account all the uncertainties just mentioned,  $\Delta P$  was over-estimated to ensure that the true value of P was included in the range of error. A value of  $P = 0.6 \pm 0.1$  was used in the calculations.

#### 5.4 Calibration.

We now consider the problem of calibrating the position sensitive detectors. What we require is an equation relating the energy of the  $^3\text{He}$  particles to channel

number in the position spectrum. A  $^{228}\text{Th}$  source was used to produce  $\alpha$ -particles with an energy of 8.785 MeV. The source was placed in the target position and the  $\alpha$  particles were focussed onto the detectors. The numbers used here are for the second experiment.

Recalling equation 4.2, we have:

$$E = (ZeB_0)^2 / 2m \quad \rightarrow \quad B_0 = (\sqrt{2m} / Ze) \sqrt{E}$$

Putting in the mass and charge of the  $\alpha$  particle, we get:

$$B \text{ (Gauss)} \rho \text{ (cm)} = 1.44 \times 10^5 \sqrt{E} \text{ (MeV)} \quad (5.5)$$

The magnetic field was measured with an NMR probe for which the following equation holds:  $B \text{ (G)} = 234.9 f \text{ (MHz)}$ .

Substituting for B in equation 5.5, we get:

$$\rho(\alpha) = 613.11 \sqrt{E} / f \quad (5.6)$$

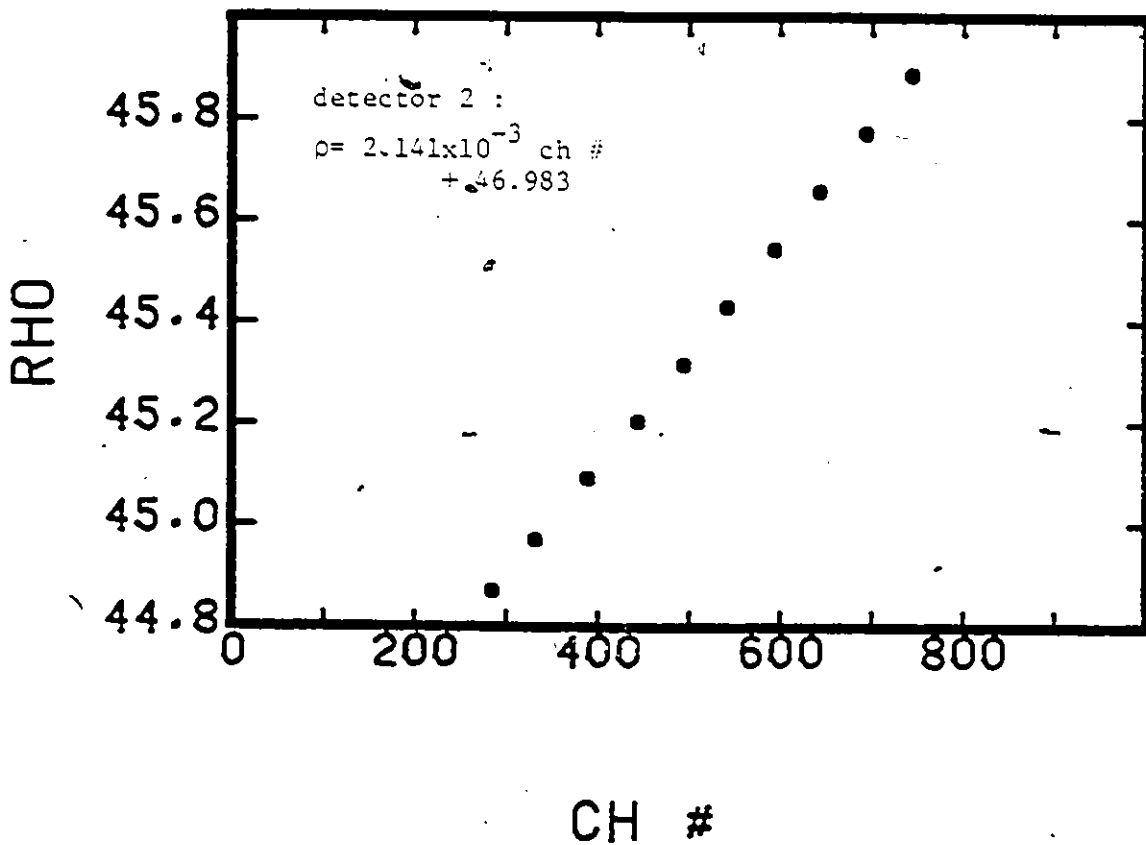
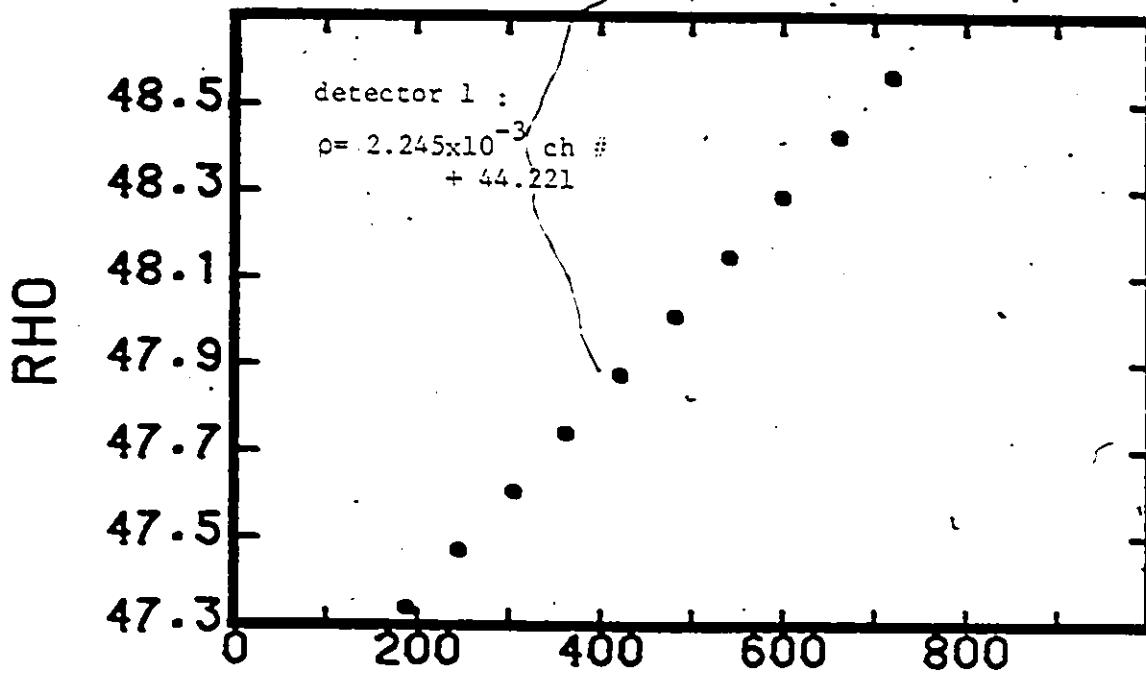
where  $\rho$  is in cm, E in MeV, and f in MHz. The field was varied and the position of the  $\alpha$  peak was noted for several points along each counter. Using equation 5.6, a plot of  $\rho$  vs channel number (ch) can be made (fig. 5.2). An equation for  $\rho$  as a function of channel number can be found from these graphs:

$$\text{detector 1: } \rho \text{ (cm)} = 2.2454 \times 10^{-3} \text{ ch} + 44.22 \quad (5.7)$$

$$\text{detector 2: } \rho \text{ (cm)} = 2.1410 \times 10^{-3} \text{ ch} + 46.98$$

These equations depend only on the geometry of the detection system and the gain of the amplifiers. Therefore, they do

Fig. 5.2 Calibration. Calibration curves for both detectors in position 2. The response is linear in  $\rho$  which is proportional to  $\sqrt{E}$ .





not change for different particle types. An equation similar to equation 5.6 can be derived for  ${}^3\text{He}$  particles:

$$\rho({}^3\text{He}) = 532.21 \sqrt{E} / f \quad (5.8)$$

The NMR frequency remained constant throughout the experiment at  $f = 42.271$  MHz. Therefore:

$$\rho({}^3\text{He}) = 12.59 \sqrt{E} \quad (5.9)$$

Combining equations 5.7 and 5.9, we obtain:

$$\text{detector 1: } E \text{ (MeV)} = ( 1.7835 \times 10^{-4} \text{ ch} + 3.512 )^2 \quad (5.10)$$

$$\text{detector 2: } E \text{ (MeV)} = ( 1.7005 \times 10^{-4} \text{ ch} + 3.732 )^2$$

Since the calibration was done with the detectors in position 2, these equations are not applicable to position 1. For the low  $\rho$  end of the focal plane, the following equation holds:

$$\rho = 88.4127 - 0.387575 D$$

where  $D$  is the distance from the high  $\rho$  end. The difference in the position of the detectors is known to be  $D = + 3.5$  cm (fig. 4.9), which corresponds to a difference in  $\rho$  of  $-1.357$  cm. Making this change to equations 5.7, we can obtain the analog of equations 5.10 for position 1:

$$\text{detector 1: } E \text{ (MeV)} = ( 1.7835 \times 10^{-4} \text{ ch} + 3.405 )^2 \quad (5.11)$$

$$\text{detector 2: } E \text{ (MeV)} = ( 1.7005 \times 10^{-4} \text{ ch} + 3.624 )^2$$

Given the limiting channel numbers, the energy range for each detector can be determined (see figs. 5.5-5.8):

Position 1:     -det. 1:  11.99 < E < 12.58 MeV

                  -det. 2:  13.36 < E < 14.10 MeV

Position 2:     -det. 1:  12.47 < E < 13.34 MeV

                  -det. 2:  14.16 < E < 14.37 MeV

One can see that the full range of  $^3\text{He}$  particles was detected (12.0-14.3 MeV).

### 5.5 Resolution.

We must now select the size of the intervals over which the  $^3\text{He}$  spectrum is to be integrated. This is determined by the resolution. The response function of the detectors can be determined by looking at the calibration spectra (figs. 5.3-5.4). These peaks are roughly 12 channels FWHM, with detector 1 being wider at the base of the peak ( $\approx 20$  ch). Therefore, a bin width of 25 channels should be well within resolution constraints. This would correspond to 66 bins across the  $^3\text{He}$  distribution. This is many more data points than are necessary and it was decided to divide the angular range into thirty 6 degree intervals.

Fig. 5.3 Resolution for Detector 1. The width of the peak  
is = 12 ch. FWHM, and = 20 ch. at the base.

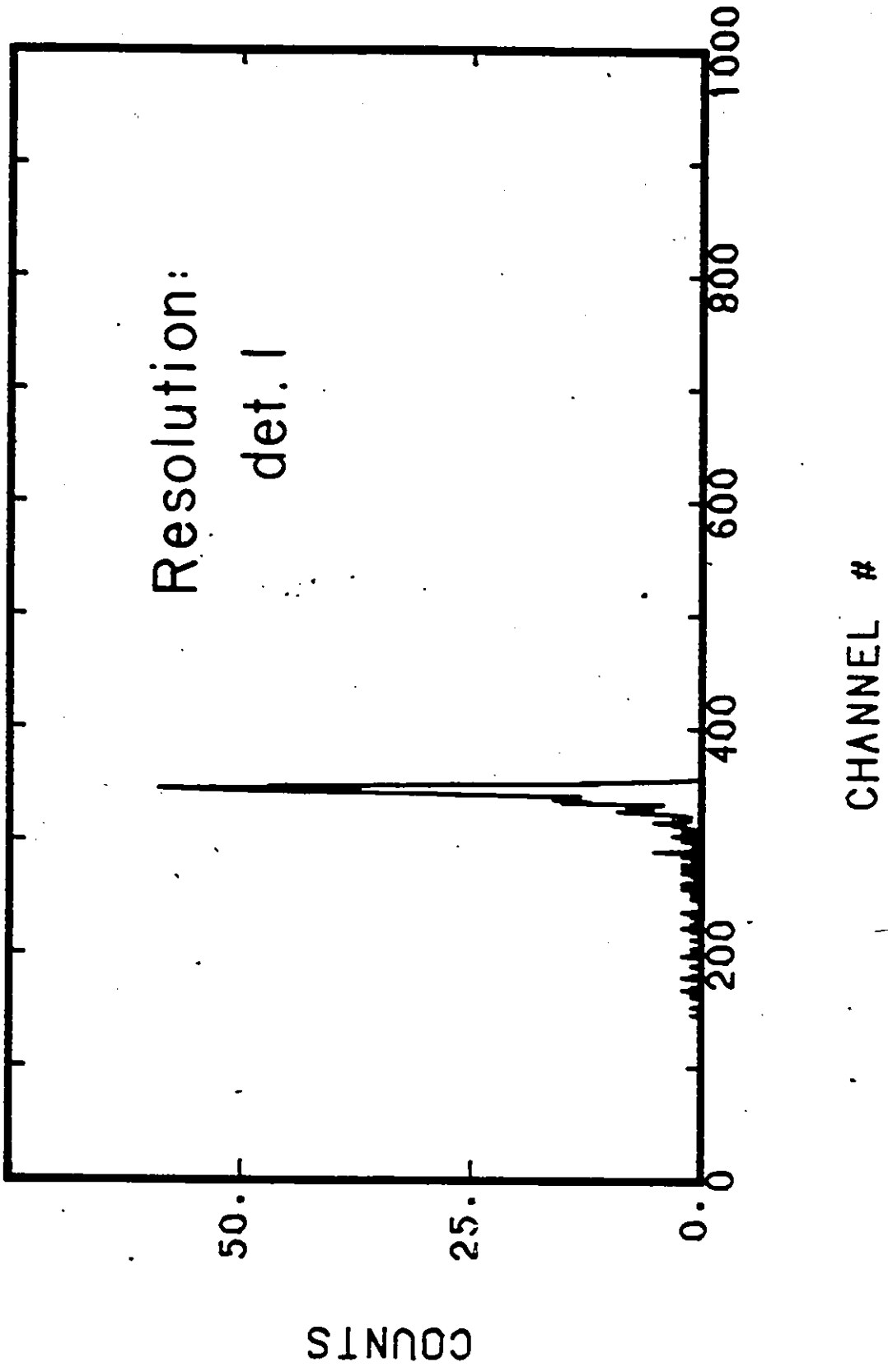
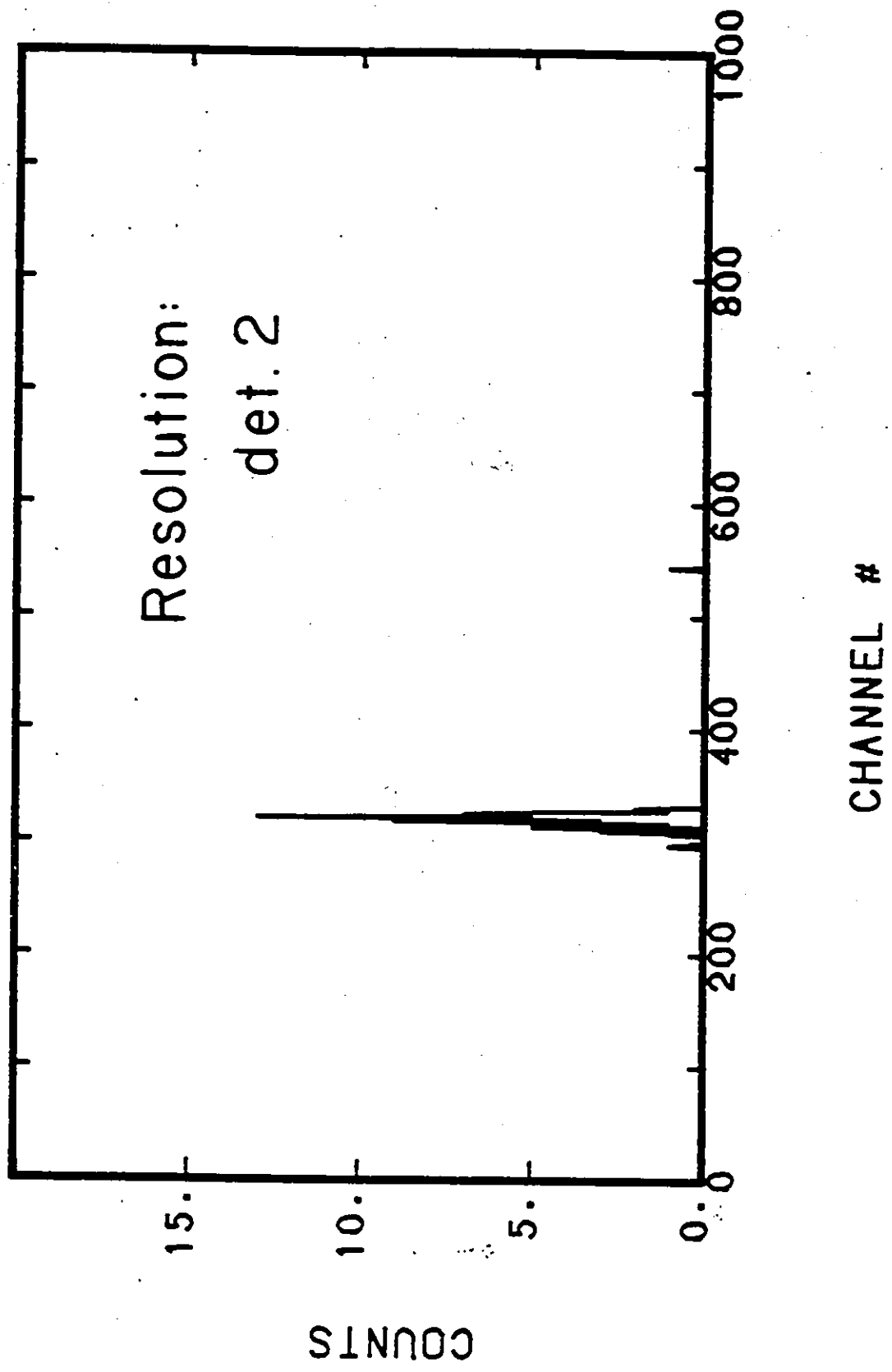


Fig. 5.4 Resolution for Detector 2. The width of the peak

is = 12 ch. FWHM.



Since the correspondence of  $\theta(\gamma)$  to channel number is not linear (see fig. 3.2), problems arise for small and large angles, where the bin width was increased.

### 5.6 Error in $T_{20}$

Before calculating the analysing powers, an expression for the error in  $T_{20}$  is derived. Recalling equation 3.34, we have:

$$T_{20} = \frac{\sigma_1 - \sigma_0}{P (\sqrt{2} \sigma_1 + \sigma_0 / \sqrt{2})} \quad (5.12)$$

where  $\sigma_0$  and  $\sigma_1$  are the yields for the  $m=0$  and the  $m=1$  substates respectively, and  $P$  is the polarization of the beam.

The error in  $T_{20}$  was calculated as follows:

$$(\Delta T_{20})^2 = \left( \frac{\delta T_{20}}{\delta \sigma_0} \right)^2 (\Delta \sigma_0)^2 + \left( \frac{\delta T_{20}}{\delta \sigma_1} \right)^2 (\Delta \sigma_1)^2 + \left( \frac{\delta T_{20}}{\delta P} \right)^2 (\Delta P)^2$$

where  $\Delta \sigma_0 = \sqrt{\sigma_0}$ ,  $\Delta \sigma_1 = \sqrt{\sigma_1}$ , and  $\Delta P = 0.1$ . The derivative with respect to  $P$  depends on  $\sigma_1 - \sigma_0$ , while the other two derivatives are proportional to  $\sigma_0$  and  $\sigma_1$ . Since the yields are large ( $500 < \sigma < 9000$ ) and the differences are small ( $20 < \sigma_1 - \sigma_0 < 300$ ), the error in  $P$  does not contribute significantly to the total error. The contribution from  $\Delta P$  is estimated to be less than 8%.

The expression used to calculate the error is:

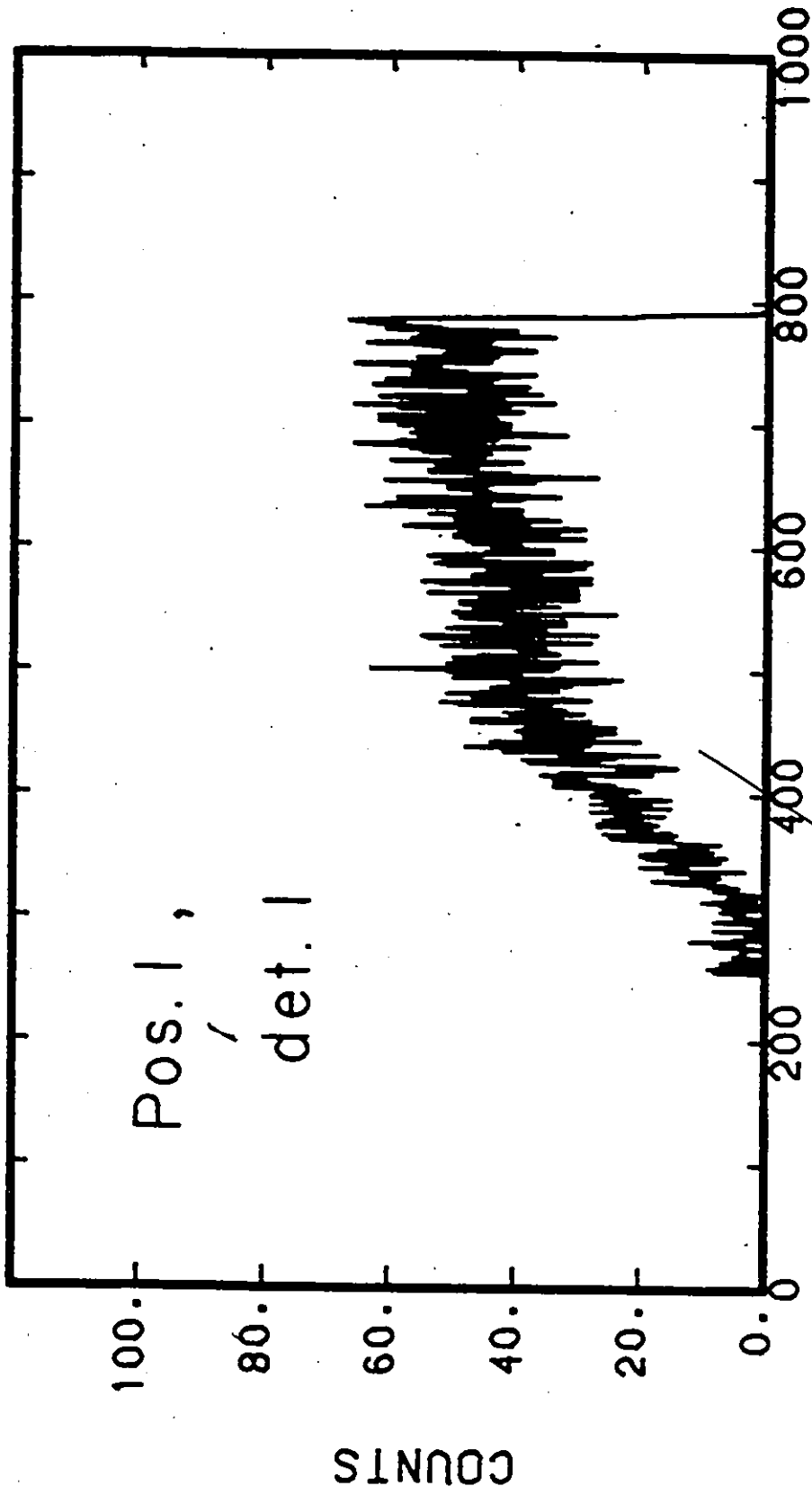
$$(\Delta T_{20})^2 = \frac{9 \sigma_1 \sigma_0 (\sigma_1 + \sigma_0)}{2 P^2 (\sigma_0/\sqrt{2} + \sqrt{2} \sigma_1)^4} + \frac{T_{20}^2}{P^2} (\Delta P)^2 \quad (5.13)$$

### 5.7 Results.

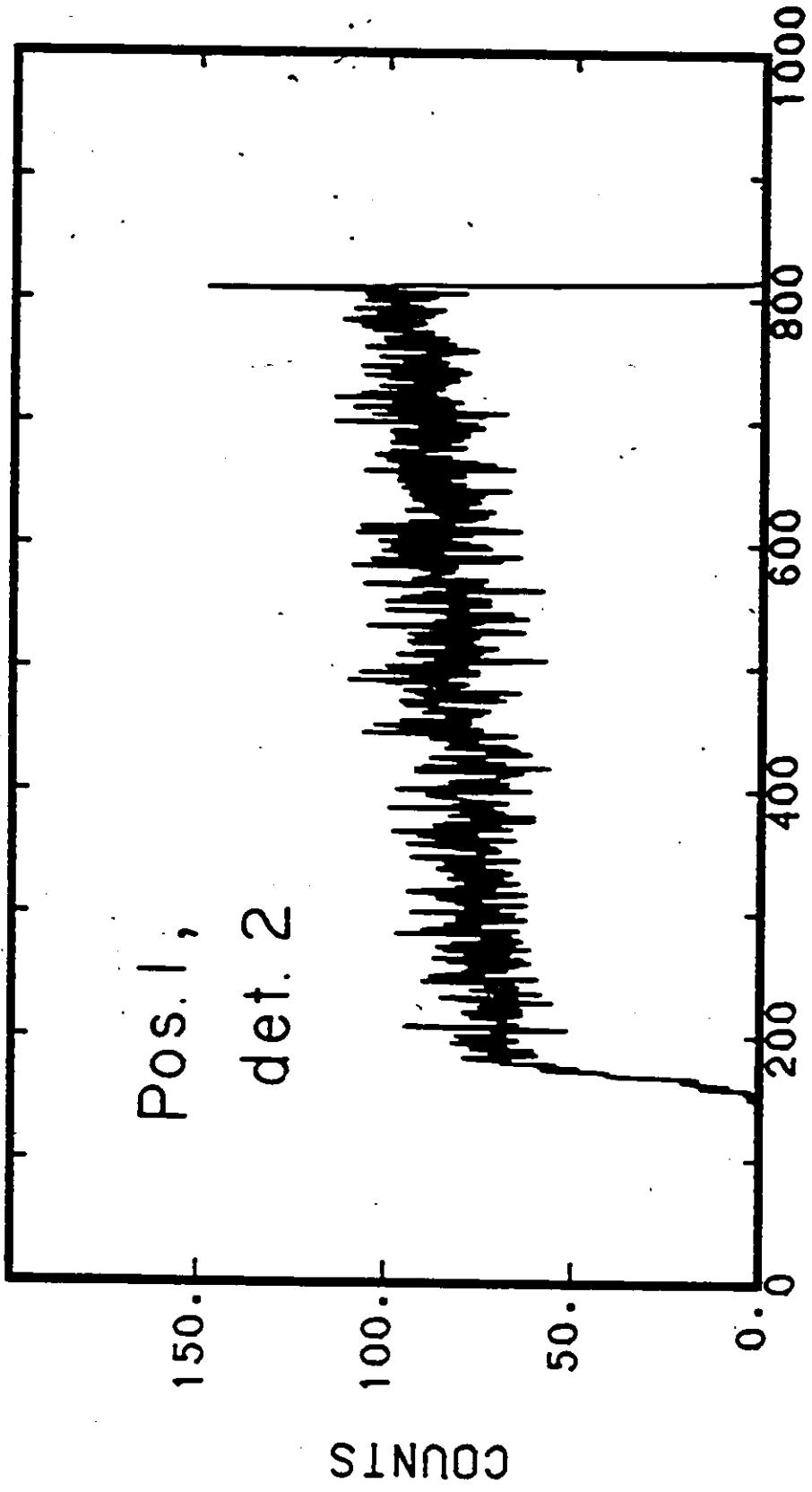
As mentioned at the beginning of this chapter, the magnetic substate of the deuteron was alternated every two hours on the average. The spectra for  $m=0$  and  $m=1$  were added separately and the results normalized to the monitor counts. This produced eight spectra: one for each of two detectors, for each of two substates, for each of two positions. The results for  $m=1$  are plotted in figures 5.5 to 5.8. The  $m=0$  spectra are not shown since they are similar to  $m=1$  and the difference is so small that it cannot be seen unless the plots are superimposed on a light table. The  $^3\text{He}$  position spectra were integrated for the bins described on page 70 to obtain the yields  $\sigma_0$  and  $\sigma_1$ . The angles defining these intervals were determined from the energies using equations 5.10 and 5.11. Values of  $\sigma_0$  and  $\sigma_1$  were then substituted into eqs. 5.12 and 5.13 to obtain  $T_{20} \pm \Delta T_{20}$ . The results for experiments one and two are listed in tables 5.1 and 5.2 respectively. The angle quoted is the angle corresponding to the middle of the interval. An averaging over  $\pm 3^\circ$  is assumed in the data, and no error is quoted for the angle. The two experiments were averaged giving a reduction in the errors by a factor of  $\sqrt{2}$ . The final values

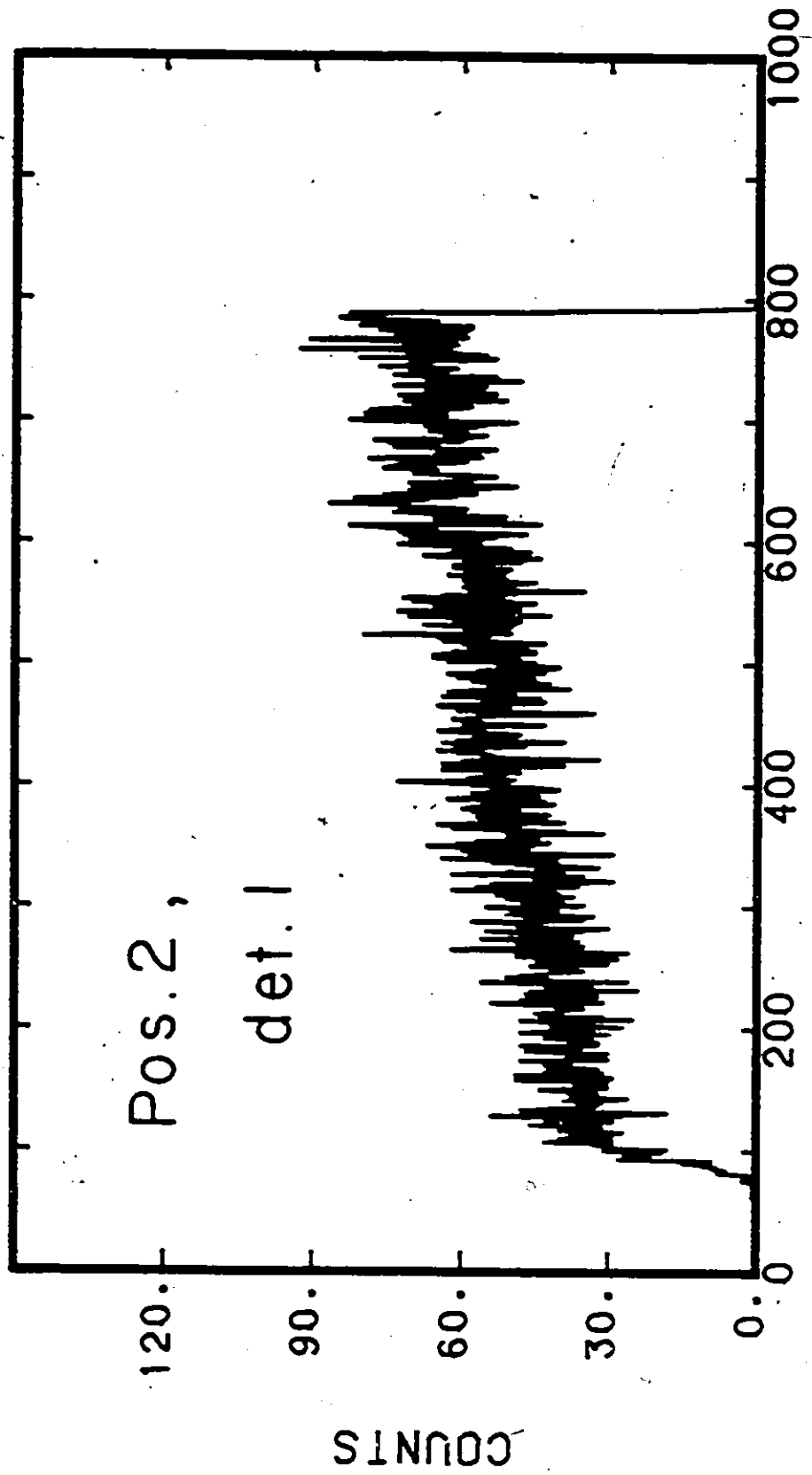


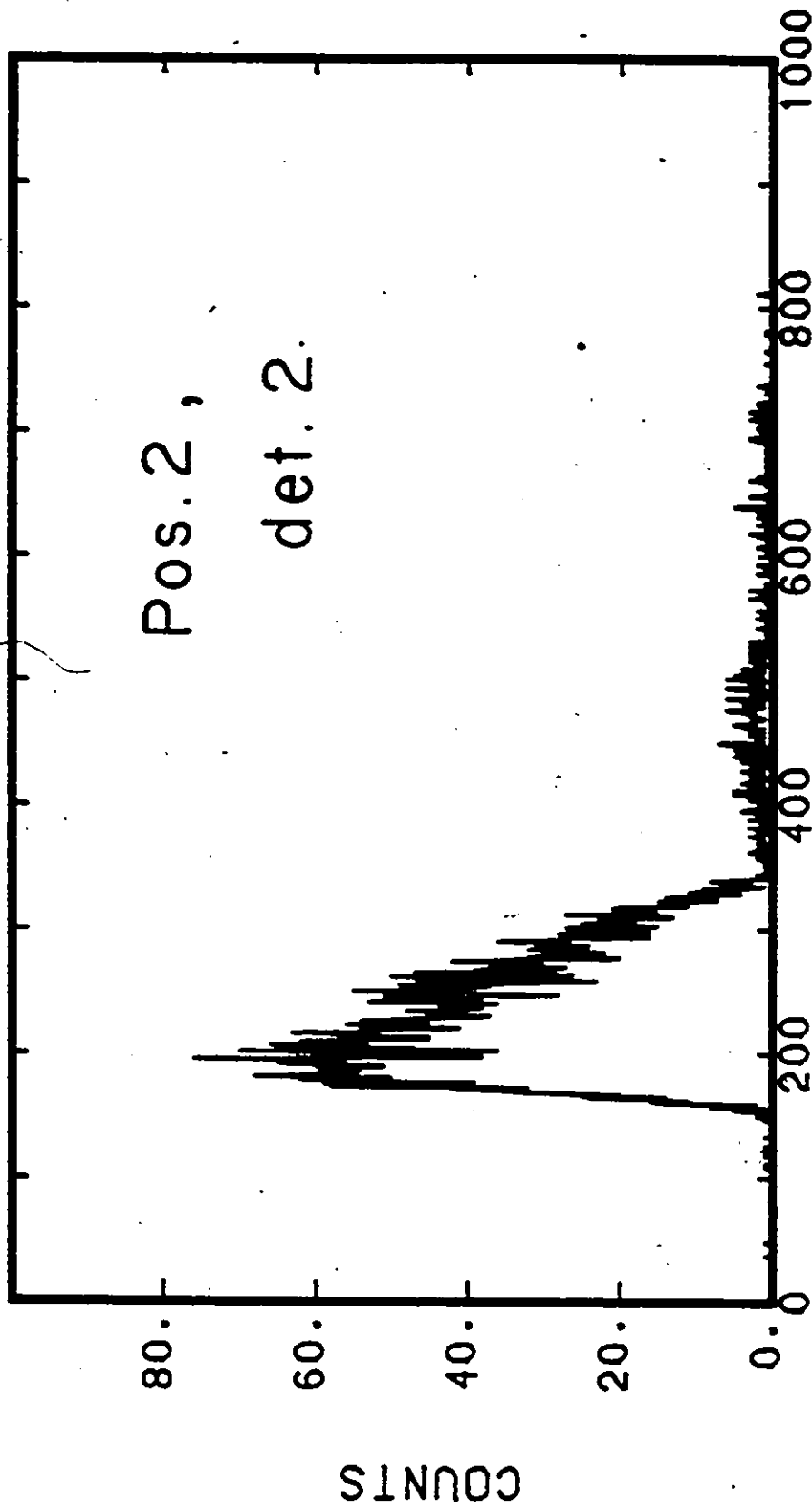
Figs. 5.5 to 5.8 Position Spectra. Total  $^3\text{He}$  position spectra summed over all the runs and normalized to monitor counts. Spectra are shown for both counters in both positions for an  $m = 1$  beam.



CHANNEL #







CHANNEL #

Table 5.1

VALUES OF  $T_{20}(\theta)$  FOR THE FIRST EXPERIMENT

$\theta$	$T_{20}$	$\Delta T_{20}$
15.6	-0.059	0.065
21.4	0.017	0.047
27.2	-0.093	0.030
33.2	-0.083	0.025
39.2	-0.126	0.023
45.2	-0.061	0.021
57.4	-0.062	0.019
63.4	-0.098	0.018
69.4	-0.062	0.015
81.4	-0.036	0.013
91.4	-0.052	0.021
99.4	-0.055	0.014
105.0	-0.060	0.013
111.0	-0.074	0.013
117.0	-0.039	0.013
123.0	-0.070	0.014
129.0	-0.044	0.014
135.0	-0.073	0.015
141.0	-0.037	0.014
145.8	-0.033	0.013
153.0	-0.007	0.019
158.9	-0.052	0.024
169.5	-0.010	0.026

Table 5.2  
VALUES OF  $T_{20}(\theta)$  FOR THE SECOND EXPERIMENT

$\theta$	$T_{20}$	$\Delta T_{20}$
15.6	0.044	0.071
21.4	-0.047	0.048
27.2	-0.047	0.036
33.2	-0.048	0.027
39.2	-0.068	0.024
45.2	-0.072	0.021
51.3	-0.069	0.019
57.3	-0.072	0.018
63.4	-0.099	0.020
69.4	-0.071	0.018
75.5	-0.034	0.016
81.4	-0.090	0.016
90.5	-0.051	0.010
98.0	-0.063	0.018
105.0	-0.072	0.014
111.0	-0.051	0.014
117.0	-0.067	0.014
123.0	-0.035	0.014
129.0	-0.056	0.014
135.0	-0.048	0.015
142.0	-0.064	0.015
153.0	-0.081	0.023
170.8	-0.039	0.027

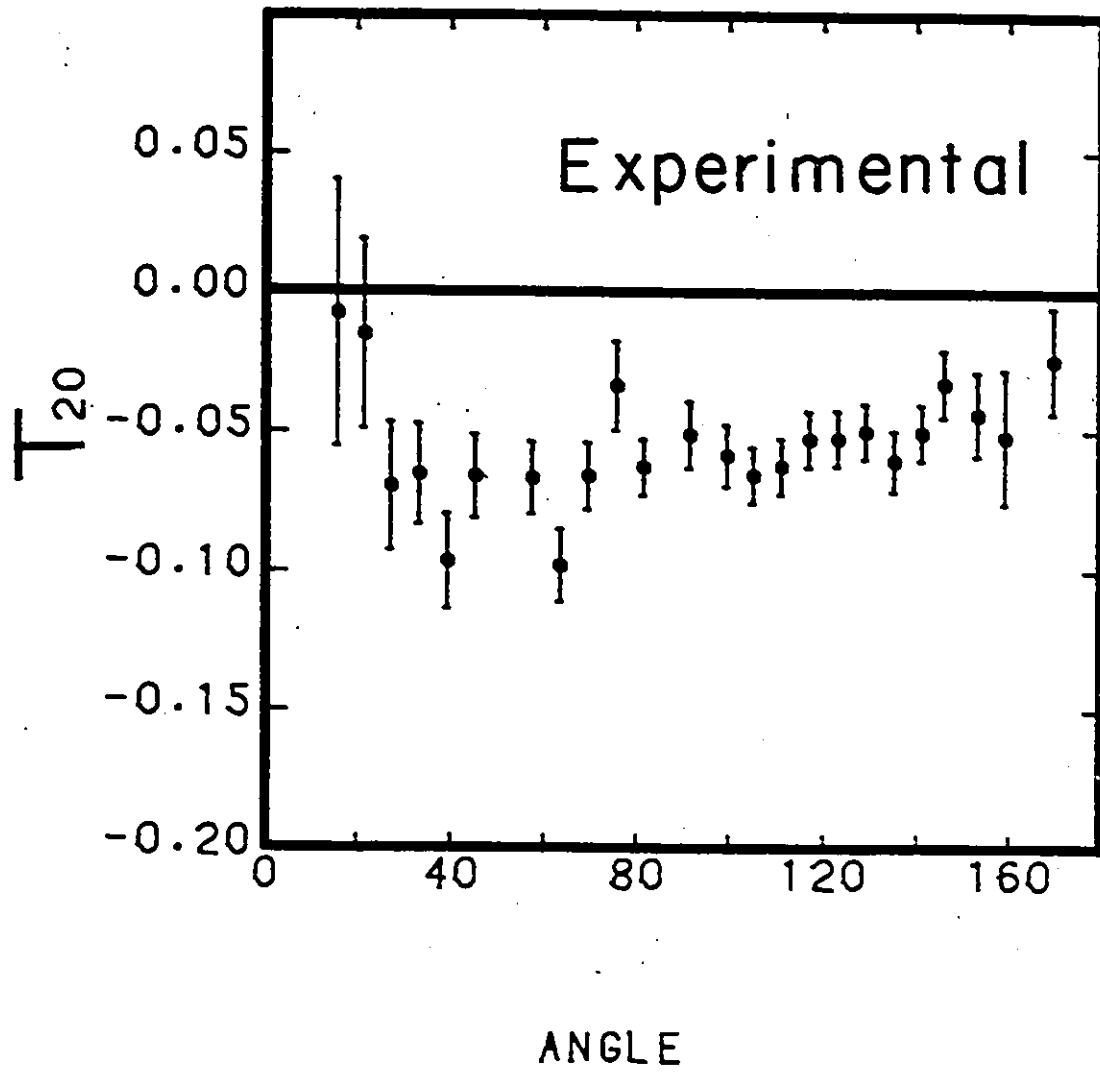
Table 5.3

RESULTS FOR  $T_{20}(\theta)$  AVERAGED OVER THE TWO RUNS

$\theta$	$T_{20}$	$\Delta T_{20}$
15.6	-0.012	0.048
21.4	-0.014	0.034
27.2	-0.074	0.023
33.2	-0.067	0.018
39.2	-0.098	0.017
45.2	-0.067	0.015
51.3	-0.069	0.019
57.3	-0.067	0.013
63.4	-0.098	0.013
69.4	-0.066	0.012
75.5	-0.034	0.016
81.4	-0.057	0.010
91.4	-0.051	0.009
99.4	-0.058	0.011
105.0	-0.066	0.010
111.0	-0.063	0.010
117.0	-0.052	0.010
123.0	-0.053	0.010
129.0	-0.050	0.010
135.0	-0.061	0.011
141.0	-0.050	0.010
145.8	-0.033	0.012
153.0	-0.037	0.015
159.0	-0.052	0.024
169.5	-0.024	0.019



Fig. 5.9 Experimental Results. Graph of the angular distribution of  $T_{20}$ . It is fairly flat with an average value of between -0.06 and -0.07.



of  $T_{20}(\theta)$  are quoted in table 5.3 and plotted in fig. 5.9.

## Chapter 6: COMPARISON WITH THEORY.

In this chapter, the results for  $T_{20}(\theta)$  are compared with the calculation described in chapter 2. The wave functions which were used are shown in section one. There follows a description of how the calculation depends on the order of the electric multipole transitions, on which partial waves are included in the entrance channel, on the optical potential used, and on the percentage D-state in the deuteron which is related to  $P_D(^3\text{He})$ . A correction for the M1 transitions is described in section seven. Theoretical predictions for the angular distributions of other analysing powers are shown in section eight. Finally, the question of the asymptotic D/S state ratio is considered in the last section.

### 6.1 Wave Functions.

As mentioned previously, the  $^3\text{He}$  wave functions are labelled by the amount of D-state present in the deuteron ( $P_D(d)$ ). This is because  $P_D(d)$  determines the interaction which generates the three-body wave functions. Furthermore, there exists a linear relationship between  $P_D(d)$  and  $P_D(^3\text{He})$ :

$$P_D(^3\text{He}) = (1.31 \pm 0.02) P_D(d) - (0.2 \pm 0.1).$$

---

Fig. 6.1 S-States. Comparison of S-state two-body projected wave functions. In the peak region the sequence is, from top to bottom:  $P_D(d) = 2\%$ ,  $4\%$ ,  $7\%$ , and  $9\%$ , while it is reversed in the tail.

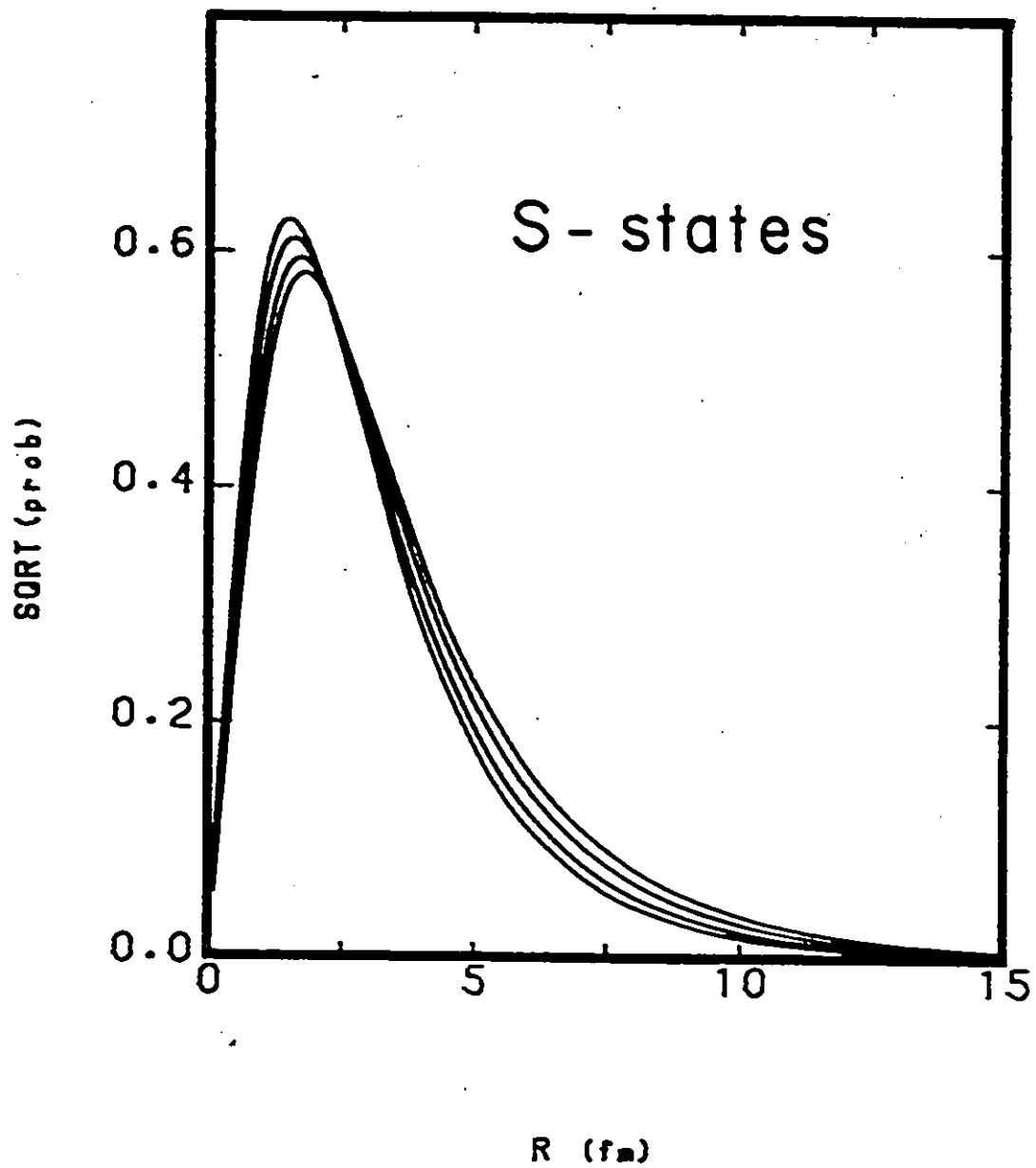
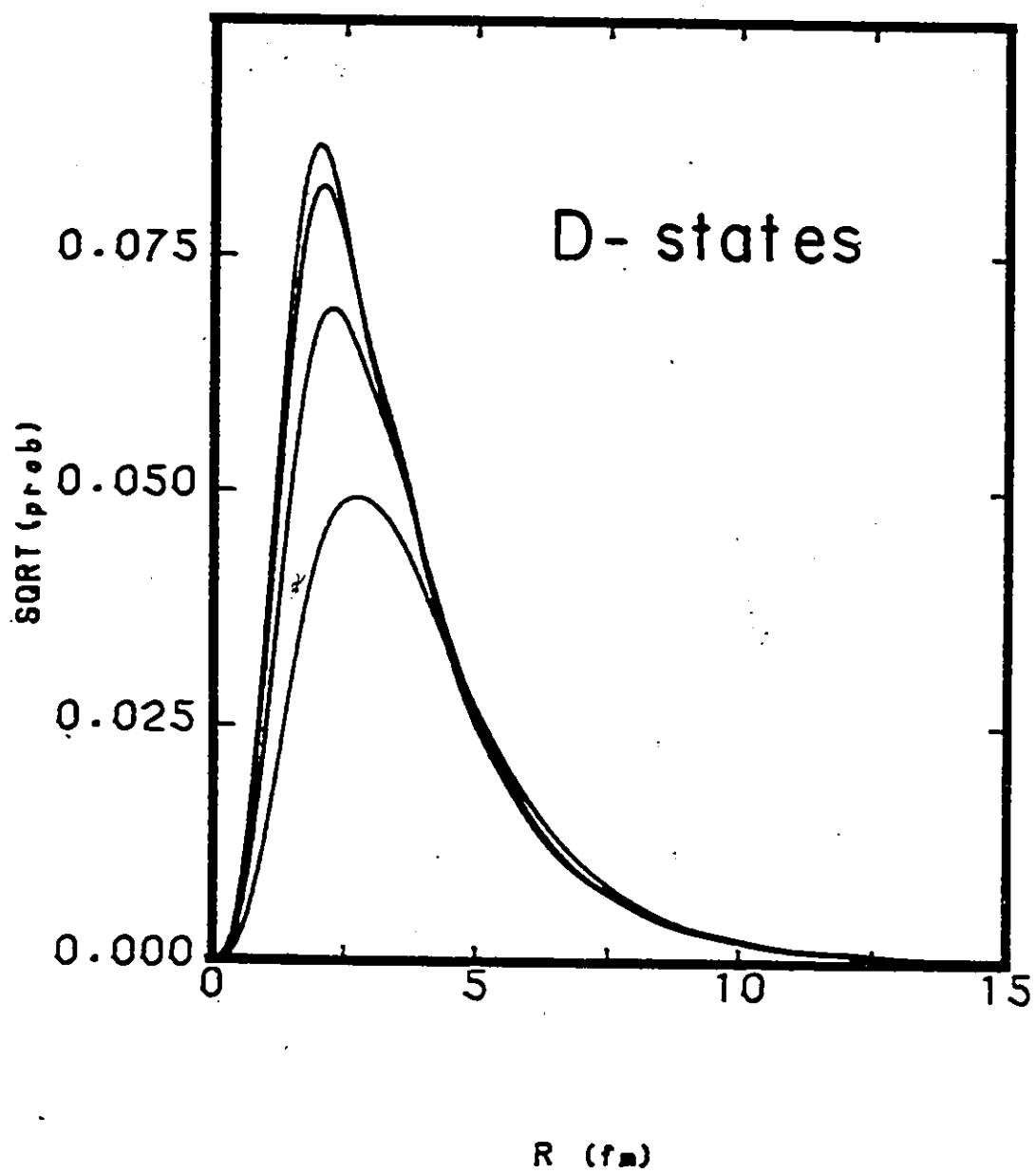


Fig. 6.2 D-States. Comparison of D-state two-body  
projected wave functions. The sequence is, from bottom to  
top:  $P_D(d) = 2\%$ ,  $4\%$ ,  $7\%$ , and  $9\%$ .





The wave functions for the S and D states corresponding to  $P_D(d) = 2\%$ ,  $4\%$ ,  $7\%$ , and  $9\%$  are plotted in figures 6.1 and 6.2 respectively. They are normalized such that:  $u_S(r)^2 + u_D(r)^2 = 1$ , and must be divided by  $r$  to obtain the true wave functions  $f_S$  and  $f_D$ .

Unless otherwise stated, the following calculations were done with the  $P_D(d) = 7\%$  wave function.

### 6.2 Dependence on the Order of the Transition.

For a beam of energy 19.8 MeV, we have seen that the reaction occurs at the peak of the giant dipole resonance (GDR). Hence, we expect the dominant transitions to be electric dipole (E1). However, the angular distribution for  $T_{20}(\theta)$  is not symmetric about  $90^\circ$ . This indicates that electric quadrupole transitions (E2) must be included. For completeness, a calculation was done adding the contribution from electric octupole transitions (E3). The results of these calculations are plotted in figure 6.3. It is obvious that E1 and E2 transitions are important. The inclusion of E3, however, does not change the angular distribution significantly, its effect showing up only as a thickening of the E1 + E2 curve. E3 transitions are therefore ignored in the remaining calculations.

### 6.3 Dependence on Partial Waves.

Partial waves up to  $L=4$  ( $L=5$  for E3) were considered in the entrance channel. Table 2.4 shows that odd

Fig. 6.3 Transition Dependence. Dependence of  $T_{20}(\theta)$  on the order of the electro-magnetic transition. The dashed curve is for E1 only, the solid curve is for E1 + E2, and the inclusion of E3 shows up only as a thickening of this line.

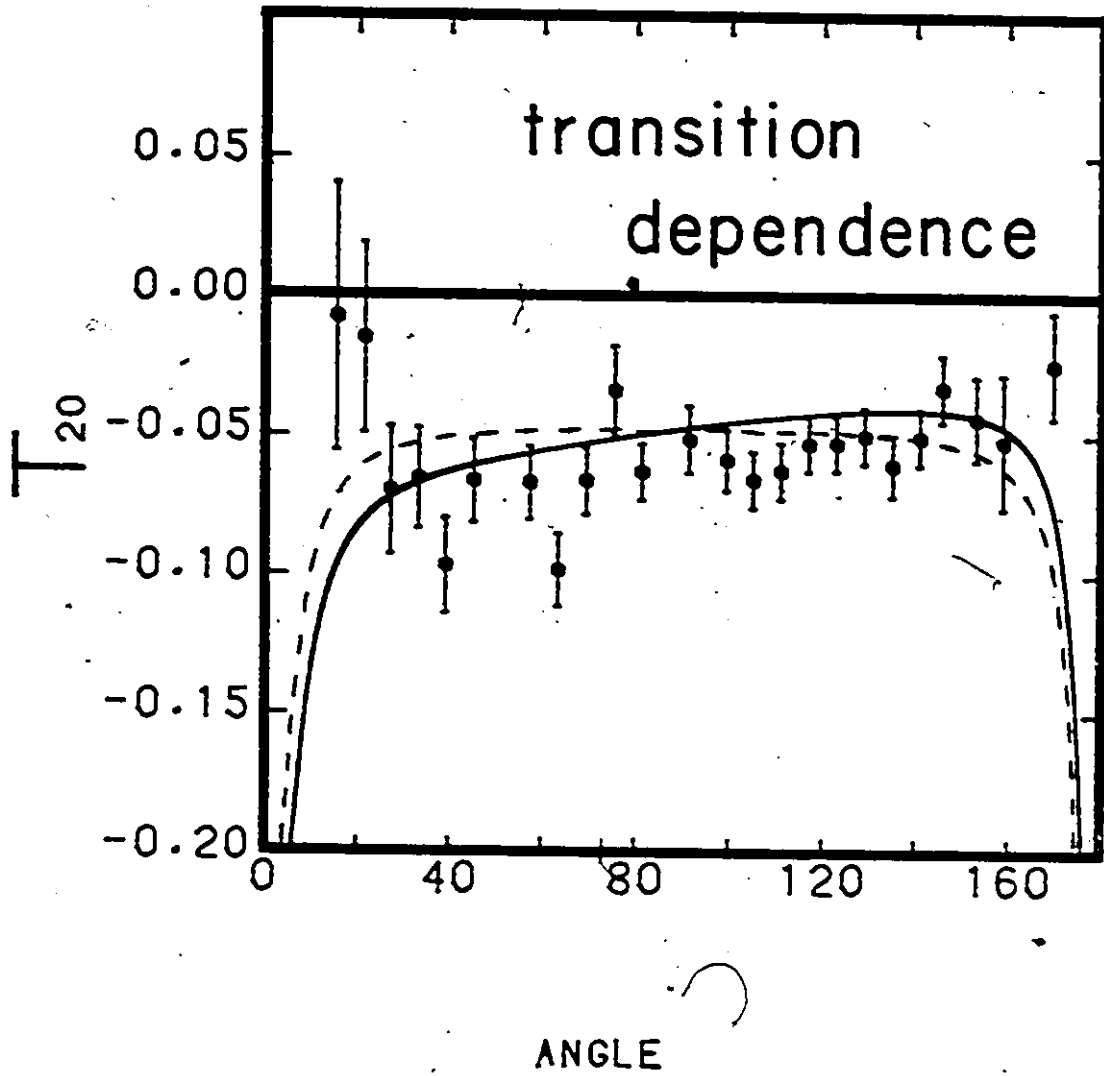
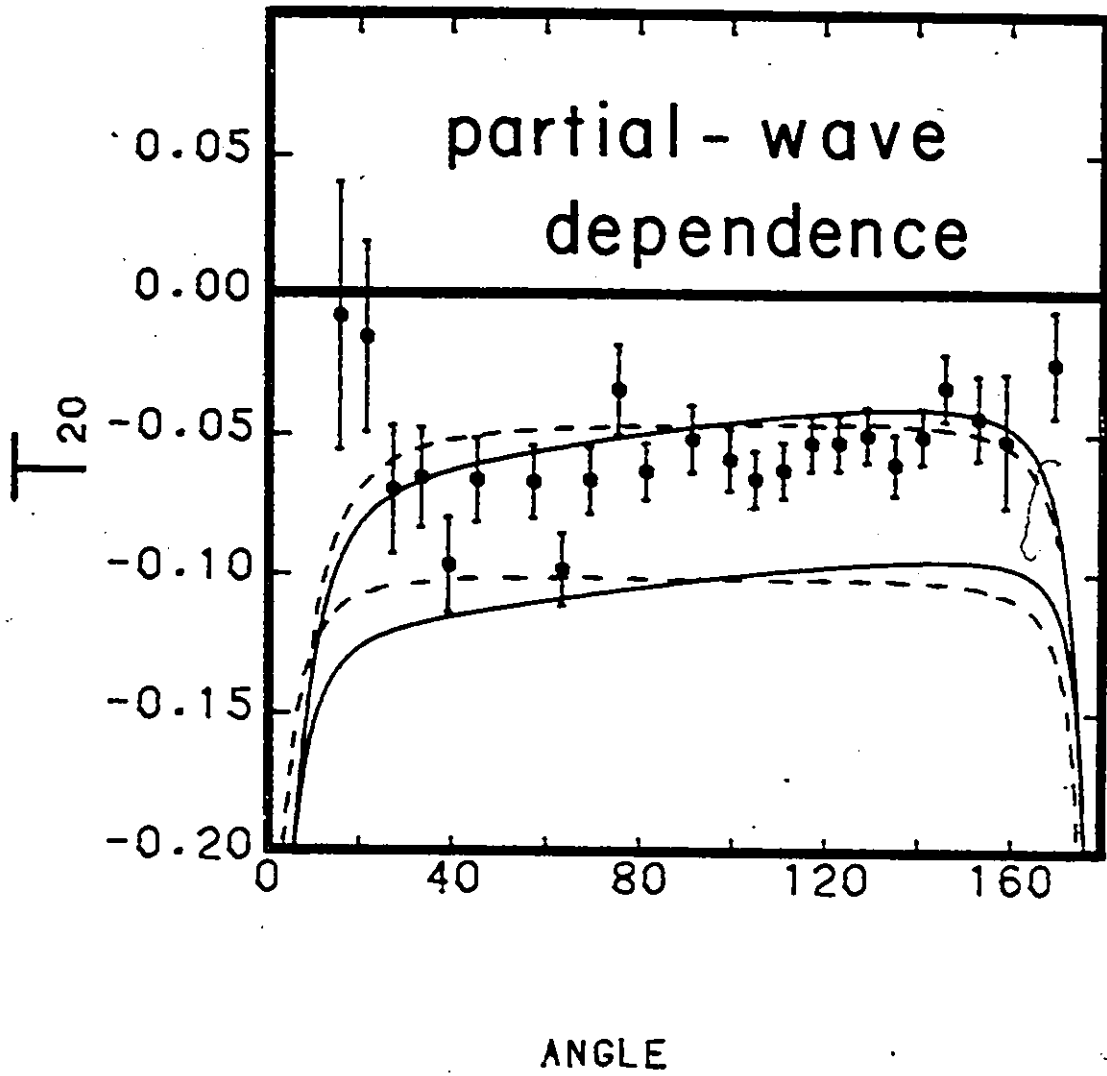




Fig. 6.4 Partial Wave Dependence.  $T_{20}(\theta)$  for different partial waves in the entrance channel. The lower dashed curve is for P-waves only. The lower solid curve is for P+D waves. The upper dashed curve is for S+P+D+F waves, and the upper solid curve is for S+P+D+F+G waves.



partial waves are associated with E1 transitions, while even partial waves correspond to E2. This is to conserve parity in the reaction.

The following notation is used: S-wave (L=0), P-wave (L=1), D-wave (L=2), F-wave (L=3), G-wave (L=4). Calculations were done for the following combinations of partial waves: P, P+D, S+P+D, S+P+D+F, and S+P+D+F+G. The results are plotted in fig. 6.4. The S-wave is not important and the P+D and S+P+D curve are identical. The inclusion of F and G waves is obviously important; the F-wave to obtain the correct magnitude, and the G-wave to re-gain the asymmetry about  $90^\circ$  lost with the inclusion of the F-wave. A semi-classical argument for this can be made. Let the deuteron approach the proton with momentum  $\vec{p}$  at an impact parameter  $\vec{R}$ . The orbital angular momentum is  $\vec{L} = \vec{p} \times \vec{R}$ . Since  $\vec{p}$  and  $\vec{R}$  are perpendicular,  $\vec{p} \times \vec{R} = pR$ , and  $L^2 = p^2 R^2$ . Substituting for  $p^2$  from  $E = p^2/2m$ , we obtain:  $L^2 = 2mER^2$ . From quantum mechanics,  $L^2 = L(L+1) h^2$ . Combining these two equations, we get:  $L(L+1) h^2 = 2mER^2$ . Multiplying both sides by  $c^2$  and putting in numerical values:

$$m_d c^2 = 1876.1 \text{ MeV}, \quad E = 19.8 \text{ MeV}, \quad hc = 197 \text{ MeV-fm}$$

we obtain:

$$L(L+1) = 1.914 R^2 \quad (R \text{ in fm})$$

S-wave: L=0	→	R > 0.00 fm
P-wave: L=1	→	R > 1.02 fm
D-wave: L=2	→	R > 1.82 fm

F-wave:  $L=3$  +  $R > 2.50$  fm

G-wave:  $L=4$  +  $R > 3.23$  fm

It will be shown that 70% of the E1 transition amplitude is between 2.5 fm and 6.0 fm. Hence, most of the capture occurs in the tail of the wave function, and it is not surprising that F and G waves are important.

#### 6.4 Dependence on the Optical Potential.

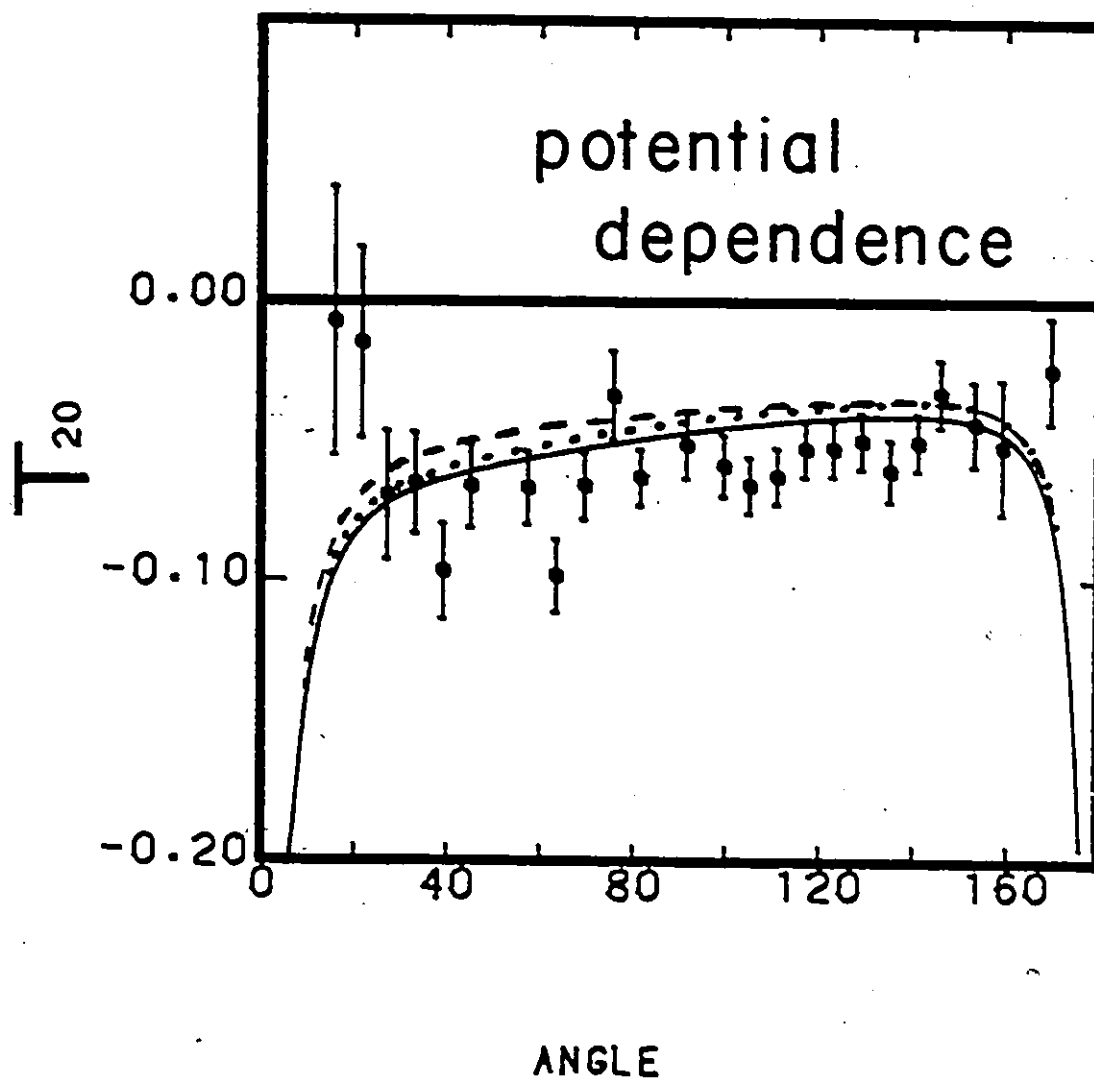
As previously mentioned, the initial state wave function was calculated from the Distorted Wave Born Approximation (DWBA). The optical potential parameters are listed in table 2.5 (pot.1). A second potential, pot.2, taken from reference (Ki83), was also used to see if the calculation is sensitive to the optical parameters. The results are plotted in fig. 6.5 and one can see that there is not much difference between the two potentials. The third curve on this graph was obtained by setting the optical potential parameters to zero, thereby mimicking a plane wave (PW) in the entrance channel. Again, not much difference is observed, even in this extreme approximation.

#### 6.5 Dependence on $P_D(d)$ .

With these preliminary calculations done, we can now study the dependence of the angular distribution of  $T_{20}$  on the D-state probability. Taking into account the results of the previous sections, potential one was used with partial waves up to  $L=4$  and E1 and E2 transitions included. Curves

Fig. 6.5 Potential Dependence.  $T_{20}(\theta)$  for different optical potentials. The solid curve is for potential 1, while the dashed curve is for potential 2. The dotted curve corresponds to a plane wave approximation.





for  $P_D(d) = 2\%$ ,  $4\%$ ,  $7\%$ , and  $9\%$  are shown in fig. 6.6. The disagreement for large and small angles will be discussed in section eight. Contrary to what was expected, the calculation does not show much sensitivity to the D-state probability. To understand this one must look at the wave functions and the matrix elements. If the radial integral is broken into sections, the following can be deduced for the E1 P-wave transition amplitude:

- =70% of it is between 2.5 fm and 6.0 fm
- =20% is inside 2.5 fm
- =10% is inside 2.0 fm

The wave functions are not much different in the interval from 2.5 fm to 6.0 fm (see figs. 6.1, 6.2). This is true for both the S and D states. Most of the variation occurs inside 2.5 fm. The observed deviation in the calculated angular distributions therefore arises from small differences in the tail of the wave functions, with only a small contribution from the interior. The sensitivity to  $P_D(d)$  is also reduced by the use of two-body projected wave functions. Table 2.6 shows that although a variation in  $P_D(d)$  from 2% to 9% results in a  $P_D(^3\text{He})$  of between 2.16% and 11.52%, the difference in the D-state probability for the two-body wave functions is only 0.72% to 1.58%. Comparing the values of  $P_D$  for the 4% and 7% wave functions, we get:

$$P_7(d) / P_4(d) = 1.75$$

$$P_7(^3\text{He}) / P_4(^3\text{He}) = 1.80$$

Fig. 6.6  $P_D(d)$  Dependence.  $T_{20}(\theta)$  for different D-state probabilities. The solid curves are for  $P_D(d) = 4\%$  (upper) and  $P_D(d) = 7\%$  (lower). The dashed curve corresponds to  $P_D(d) = 2\%$ , while the dotted curve is for  $P_D(d) = 9\%$ .

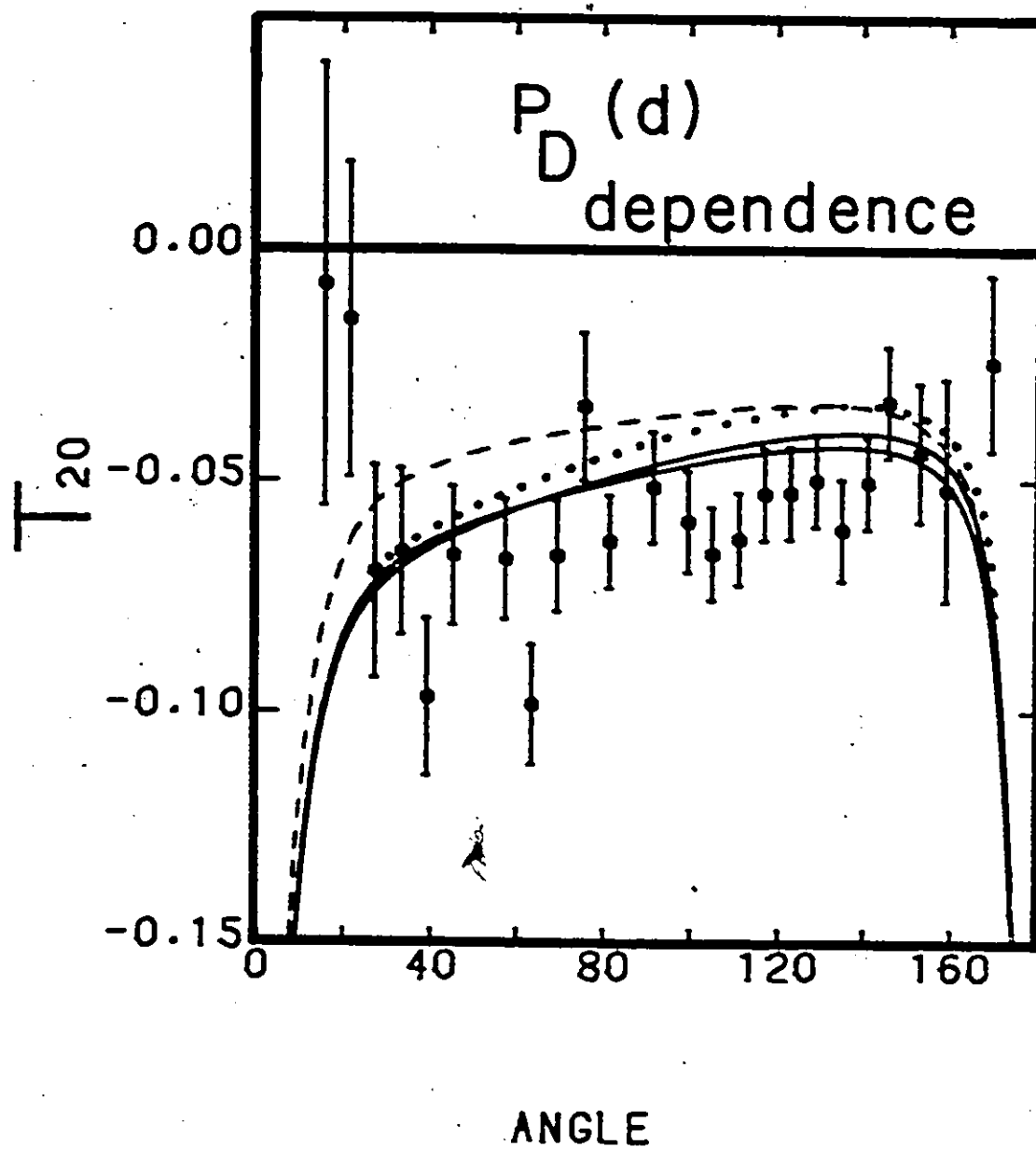
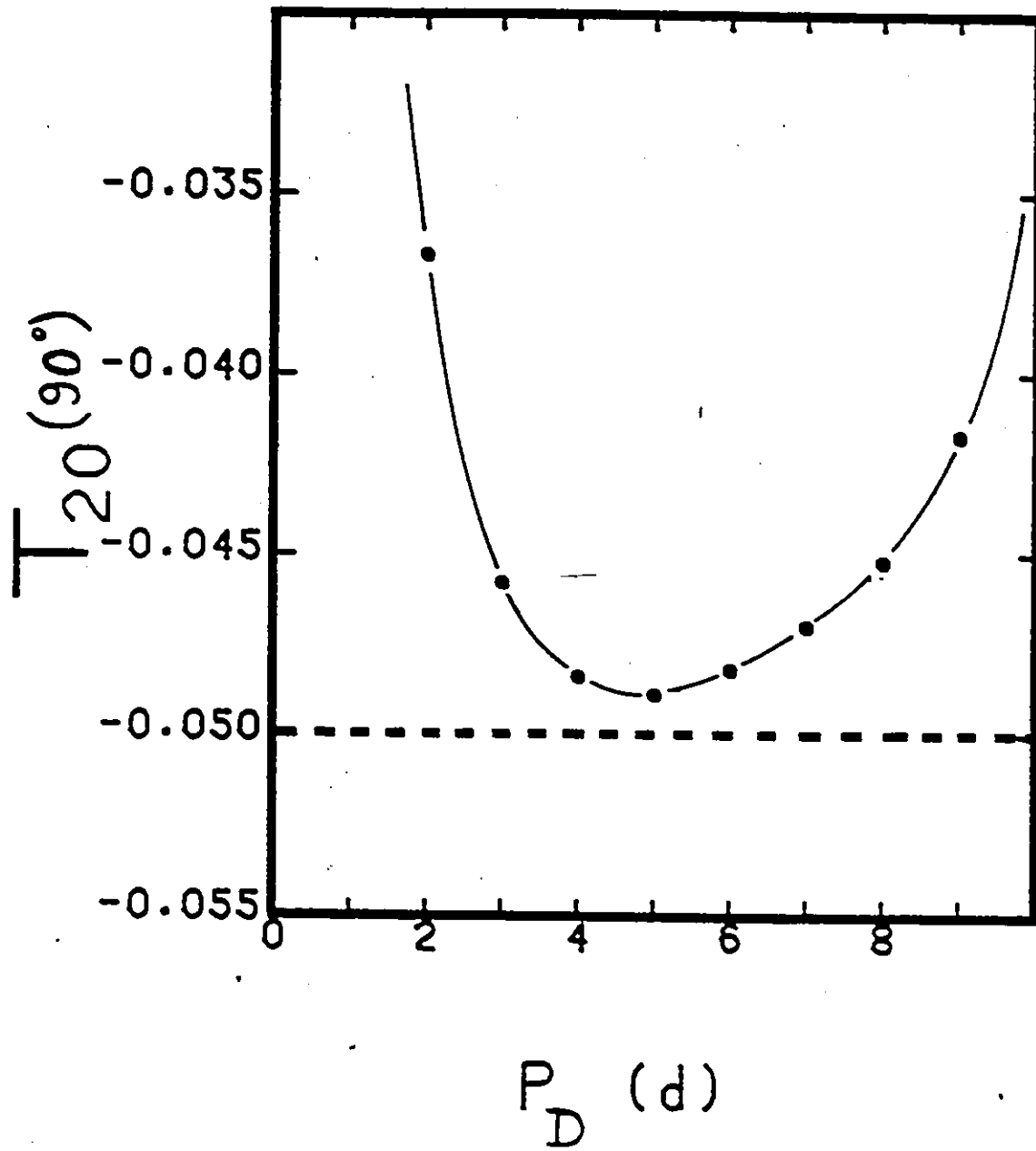


Fig. 6.7  $\underline{T_{20}(90^\circ)}$ .  $T_{20}$  at  $\theta = 90^\circ$  for  $2\% \leq P_D(d) \leq 9\%$ .

The dashed line is one standard deviation from the experimental value of  $T_{20}(90^\circ)$ .



$$P_7(d+p) / P_4(d+p) = 1.25$$

Although the sensitivity to the D-state is not as large as expected, a range for  $P_D$  can be inferred by the data. It is clear that the curves for the 4% and 7% wave functions fit the data better than the curves for 2% and 9%. A plot of the analysing power at  $90^\circ$  as a function of  $P_D(d)$  is shown in fig. 6.7. The horizontal line is one standard deviation from the experimental value of  $T_{20}(90^\circ)$ . Taking into account these two figures, the range of  $P_D(d)$  deduced is:

$$0.04 \leq P_D(d) \leq 0.07$$

#### 6.6 Second Calculation.

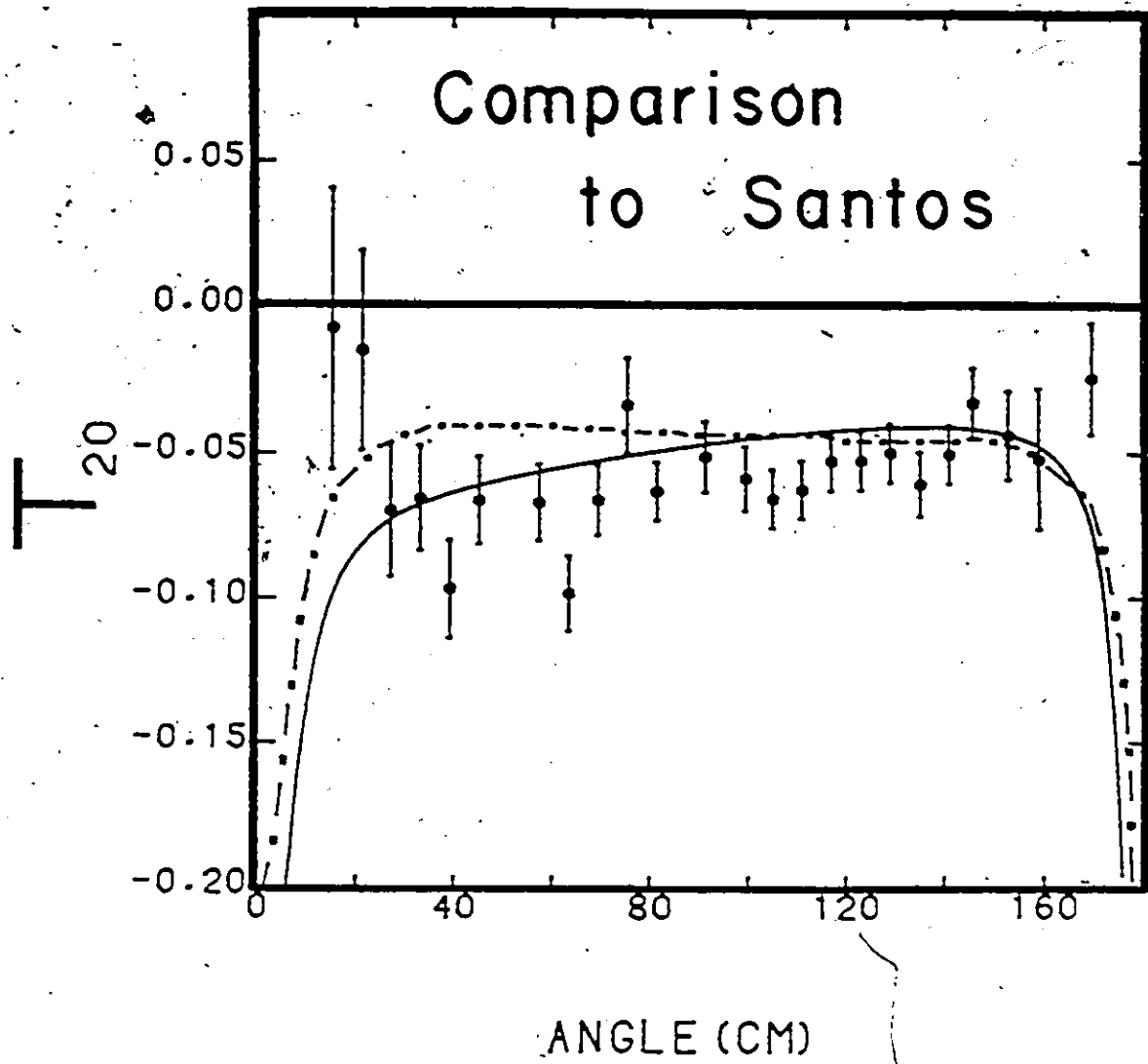
A calculation using a different wave function was done by F. Santos (Sa84). The model used is described in (AS84). The wave function of Sasakawa and Sawada (SS79) was used in the calculation and the results are shown in fig.6.8 where they are compared to the best fit for our calculation with Gibson and Lehman's wave functions. Santos generates only one curve corresponding to a D-state probability of 8.02% in the three-body wave function.

#### 6.7 M1 correction.

As mentioned above, the agreement of the calculation with the data breaks down badly at large and small angles ( $\theta \leq 25^\circ$ ,  $\theta \gg 155^\circ$ ). This is thought to be due to the

Fig. 6.8 Comparison to Santos. Comparison of the best fit for the present model to the calculation of Arriaga and Santos (dot-dashed curve) which uses the wave function of Sasakawa and Sawada.





omission of M1 transitions (AD81). The M1 matrix elements are difficult to calculate because the initial and final states are not orthogonal. This is because they are obtained from two separate calculations using different Hamiltonians: a DWBA model for the initial state and Faddeev equations for the bound state. This leads to spurious M1 strength. The situation is not as serious for the electric multipoles because the  $r^2$  term in the operator allows transitions between radially orthogonal states and the spurious strength from the non-orthogonality is only a perturbation. Before a calculation including M1 terms can be done, the wave functions must be orthogonalized. This is not a trivial operation with numerical functions.

Instead of attempting this tedious calculation, the M1 matrix elements were treated as parameters and were fitted to the data. A standard least-squares fitting program was unable to converge in a reasonable time. The following procedure was used to obtain the best values for the amplitudes and relative phases of the M1 matrix elements.

Table 2.4 shows the possible M1 transitions, of which there are five. If we restrict ourselves to S-wave capture, only the  ${}^2S_2$  and  ${}^4S_4$  matrix elements remain. These will be denoted A and B respectively. The  $a_k$  and  $c_k$  coefficients given in appendix B are modified as follows:

$$a_0 = a_0(\text{old}) + 0.333 A^2 + 0.667 B^2$$

$$a_1 = a_1(\text{old}) - 0.667 \ ^2P_2A - 0.471 \ ^4P_2B + 0.667 \ ^2P_4A \\ - 1.491 \ ^4P_4B$$

$$a_2 = a_2(\text{old}) - 1.155 \ ^2D_4A - 1.155 \ ^4D_4B + 1.155 \ ^2D_6A \\ - 2.160 \ ^4D_6B$$

$$a_3 = a_3(\text{old})$$

$$a_4 = a_4(\text{old})$$

$$c_0 = c_0(\text{old})$$

$$c_1 = c_1(\text{old}) - 0.471 \ ^2P_2B - 0.667 \ ^4P_2A + 0.333 \ ^4P_2B \\ + 0.471 \ ^2P_4B - 0.211 \ ^4P_4A - 0.843 \ ^4P_4B \\ + 0.632 \ ^4F_4A - 0.632 \ ^4F_4B$$

$$c_2 = c_2(\text{old}) + 0.471 \ AB + 0.236 \ B^2 - 0.816 \ ^2D_4B + 0.816 \ ^4S_4A \\ - 0.816 \ ^4S_4B + 0.816 \ ^4D_4A + 0.816 \ ^2D_6B \\ - 0.436 \ ^4D_6A - 1.091 \ ^4D_6B + 1.069 \ ^4G_6A \\ - 1.069 \ ^4G_6B$$

$$c_3 = c_3(\text{old})$$

$$c_4 = c_4(\text{old})$$

where the phases have been omitted as in appendix B (i.e.  $0.667 \ ^2P_2A = 0.667 \ ^2P_2A \cos(\phi(^2P_2) - \phi(A))$ ). For the best fit without M1 ( $P_D(d) = 7\%$ ), the matrix elements are listed in table 6.1. Putting these values into the above equations, and using  $\cos(\alpha - \beta) = \cos \alpha \cos \beta + \sin \alpha \sin \beta$ , we get:

$$a_0 = a_0(\text{old}) + 0.333 \ A^2 + 0.667 \ B^2$$

$$a_1 = a_1(\text{old})$$

$$a_2 = a_2(\text{old})$$

Table 6.1.

MATRIX ELEMENTS FOR  $P_D(d) = 7\%$ 

Amplitudes and relative phases of the matrix elements obtained from the  $P_D(d) = 7\%$  wave function.

Matrix Element	Amplitude	Relative phase
$2P_2$	0.98836	208.94
$2P_4$	0.98836	208.94
$4P_2$	0.12421	31.54
$4P_4$	0.03928	211.54
$4F_4$	0.04659	185.60
$2D_4$	0.09628	5.59
$2D_6$	0.09628	5.59
$4S_4$	0.00502	128.04
$4D_4$	0.00681	185.81
$4D_6$	0.00364	5.81
$4G_6$	0.00370	6.01

$$a_3 = a_3(\text{old})$$

$$a_4 = a_4(\text{old})$$

$$c_0 = c_0(\text{old})$$

$$c_1 = c_1(\text{old}) - 0.09285 A \cos \phi_A - 0.04187 A \sin \phi_A \\ + 0.09277 B \cos \phi_B + 0.04183 B \sin \phi_B$$

$$c_2 = c_2(\text{old}) + 0.471 AB \cos(\phi_A - \phi_B) + 0.236 B^2 \\ + 0.00536 A \cos \phi_A + 0.00406 A \sin \phi_A \\ - 0.00536 B \cos \phi_B - 0.00406 B \sin \phi_B$$

$$c_3 = c_3(\text{old})$$

$$c_4 = c_4(\text{old})$$

The values of  $a_k(\text{old})$  and  $c_k(\text{old})$  for  $P_D(d)=7\%$  are listed in table 6.2.

The equation for  $a_0$  is ignored since  $a_0$  affects only the total cross-section and therefore is simply an overall normalization. The following constraints are made on  $T_{20}$ :

$$T_{20}(0^\circ) = 0 \quad \rightarrow \quad \sum_k c_k = 0 \quad \rightarrow \quad c_1 + c_2 = 0.05401$$

$$T_{20}(180^\circ) = 0 \quad \rightarrow \quad \sum_k (-1)^k c_k = 0 \quad \rightarrow \quad c_2 - c_1 = 0.04129$$

These give:

$$c_1 = 0.00636$$

$$c_2 = 0.04765$$

Therefore, we have two equations and four unknowns. To reduce the number of variables, we consider the shape of the Legendre polynomials involved:

$$P_1(\cos \theta) = \cos \theta$$

$$P_2(\cos \theta) = 1/2 (3 \cos^2 \theta - 1)$$

$P_2$  is symmetric about  $90^\circ$  and large for extreme angles,

Table 6.2

 $a_k$  AND  $c_k$  COEFFICIENTS FOR  $P_D = 7\%$ 

$$a_0 = 1.0000$$

$$a_1 = -0.3035$$

$$a_2 = -0.9631$$

$$a_3 = 0.3023$$

$$a_4 = -0.0265$$

$$c_0 = -0.04760$$

$$c_1 = 0.00683$$

$$c_2 = 0.04400$$

$$c_3 = -0.00636$$

$$c_4 = -0.00005$$

while  $P_1$  is anti-symmetric about  $90^\circ$ . If we wish to change the values of  $T_{20}(\theta)$  for small and large angles, but not the shape of the curve between  $25^\circ$  and  $155^\circ$ , we must have  $\Delta c_1 = 0$  and  $\Delta c_2$  a maximum. Taking the derivative of the expression for  $c_1$  with respect to  $\phi_A$  and  $\phi_B$  equal to zero, we get:

$$\phi_A = -65.73^\circ \text{ or } 114.27^\circ ; \quad \phi_B = -65.71^\circ \text{ or } 114.27^\circ$$

We choose the combination of these which maximizes  $\Delta c_2$  for a given amplitude of the matrix elements. As a final approximation, let  $B = A/10$  which is consistent with the ratio of the amplitudes of the  $S = 3/2$  to  $S = 1/2$  channel in all previous calculations. Taking all this into account, we choose:

$$\phi_A = \phi_B = 114.28^\circ$$

$$\Delta c_2 = 0.04946 A^2 + 0.00135 A$$

For  $\Delta c_2 = 0.04765 - 0.044 = 0.00365$ , we get  $A = 0.2584$ . It was found that these parameters do not give symmetric angular distributions at extreme angles where the contributions of  $M_1$  are now large. A further iteration on the phase angles was done and the following equations were used to generate  $T_{20}(\theta)$  curves:

$$\phi_A = \phi_B = 113^\circ ; \quad B = A/10$$

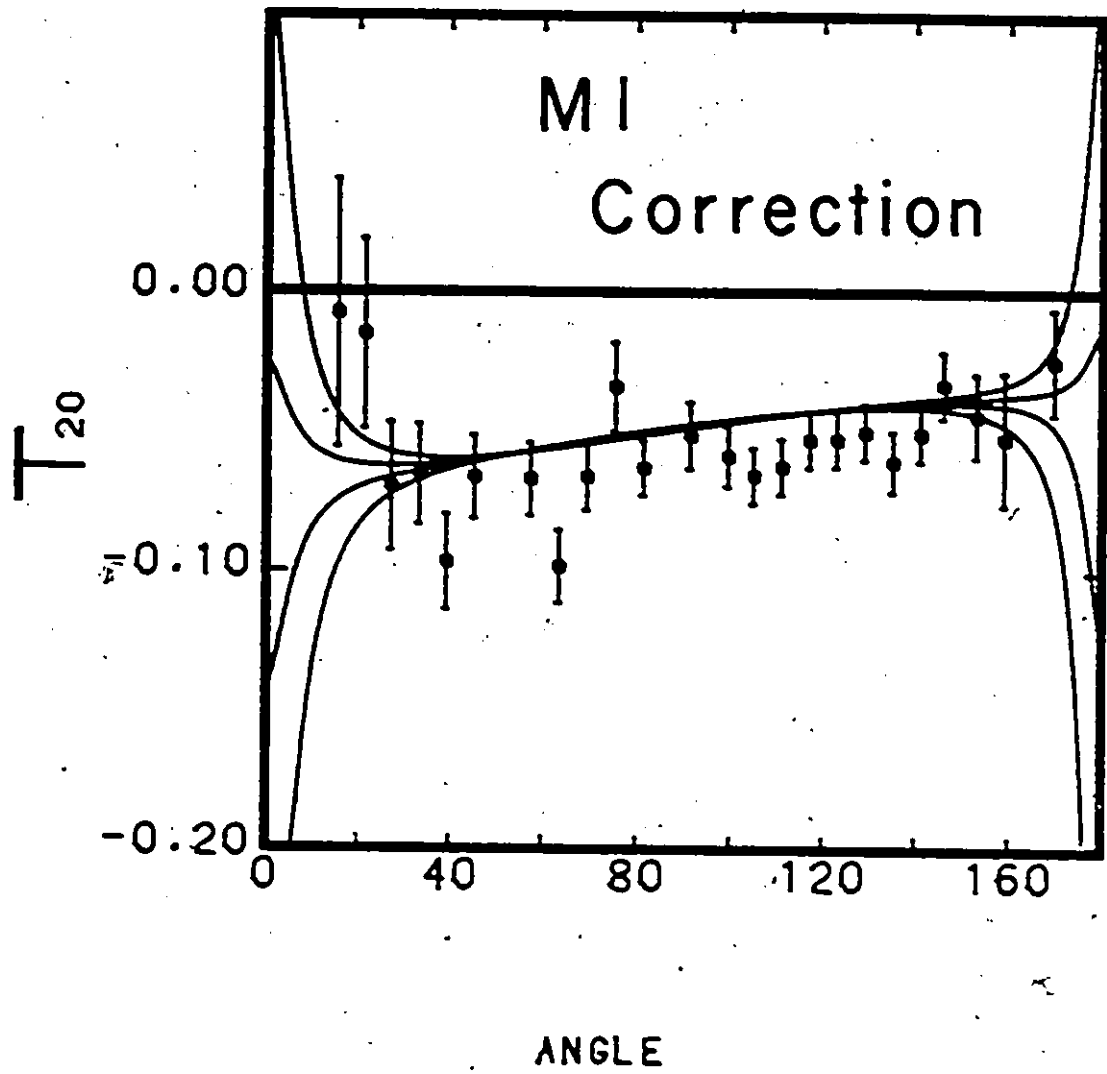
$$c_1 = 0.00683 - 0.002036 A$$

$$c_2 = 0.044 + 0.001479 A + 0.04946 A^2$$

Plots of  $T_{20}(\theta)$  for different values of  $A$  are shown in fig. 6.9. One can see that  $A = 0.30$  is sufficient to remove the disagreement at extreme angles.

Fig. 6.9 M1 Correction. The M1 matrix elements are treated as parameters. The curves correspond to (from top to bottom):  $A = 0.30, 0.25, 0.20,$  and  $0.0$ . A contribution to the total cross-section of 3% ( $A = 0.30$ ) by the M1 transitions is sufficient to account for the extreme angle discrepancies.





Finally, we calculate what M1 strength corresponds to  $A = 0.30$ . To do so, we consider the  $a_0$  coefficient:

$$\begin{aligned}
 a_0 = & 0.333 \ ^2P_2^2 + 0.333 \ ^4P_2^2 + 0.667 \ ^2P_4^2 + 0.667 \ ^4P_4^2 \\
 & + 0.667 \ ^4F_4^2 + 0.667 \ ^2D_4^2 + 0.667 \ ^4S_4^2 \\
 & + 0.667 \ ^4D_4^2 + \ ^2D_6^2 + \ ^4D_6^2 + \ ^4G_6^2 \\
 & + 0.333 \ A^2 + 0.667 \ B^2
 \end{aligned}$$

where the P and F matrix elements are E1, the S, D, and G elements are E2, and the A and B elements are M1. The value of the matrix elements can be found in table 6.1, with  $A = 0.3$  and  $B = 0.03$ . We get:

$$a_0 = 0.984474 (E1) + 0.01554 (E2) + 0.0306 (M1) = 1.0306$$

Re-normalizing the matrix elements by  $\sqrt{1.0306}$ , we get:

$$a_0 = 0.95525 (E1) + 0.01207 (E2) + 0.02969 (M1) = 1.00$$

and hence the relative strengths of the transitions are:

$$E1 : 95.5\%$$

$$E2 : 1.5\%$$

$$M1 : 3.0\%$$

Although this calculation has many approximations, it does show that it is possible for M1 transitions with a total strength of only 3% to remove the disagreement between theory and experiment at extreme angles.

### 6.8 $T_{21}$ , $T_{22}$ , $\sigma(\theta)$ .

The matrix elements for E1 and E2 transitions with  $P_D(d) = 7\%$  were used to calculate the other tensor analysing powers  $T_{21}$  and  $T_{22}$ , and the differential cross-section  $\sigma(\theta)$ . The vector analysing power  $A_y$  (or  $iT_{11}$ ) was not calculated because spin-orbit effects in the entrance channel should be important in this case. Results for  $T_{21}$  are shown in fig. 6.10, while  $T_{22}$  is plotted in fig. 6.11. Attempts were made to extract the differential cross-section from the data. The correction that must be made due to the entrance slits of the spectrograph is described by Belt (Be70). Problems were encountered because of a contamination of the spectrum near  $90^\circ$  by the  $^{16}\text{O}(\bar{d}, ^3\text{He})^{15}\text{N}$  reaction. This is also why two data points in this angular region were ignored in the  $T_{20}$  analysis. The angular distribution of the differential cross-section is therefore distorted. Since the cross-section has been well studied (BB70), it was not deemed necessary to pursue this point. Nevertheless, a calculation of the cross-section was done and is shown in fig. 6.12. This agrees with the calculation of King and the reader is referred to KR83 for a detailed discussion of the differential cross-section.

### 6.9 Asymptotic D/S State Ratio.

As described in chapter 2, it should be possible to extract a value for the asymptotic D/S state ratio  $\eta$ . The asymptotic wave functions are given on page 23. The above

Fig. 6.10 Calculated  $T_{21}$ . The  $P_D(d) = 7\%$  wave function was used.

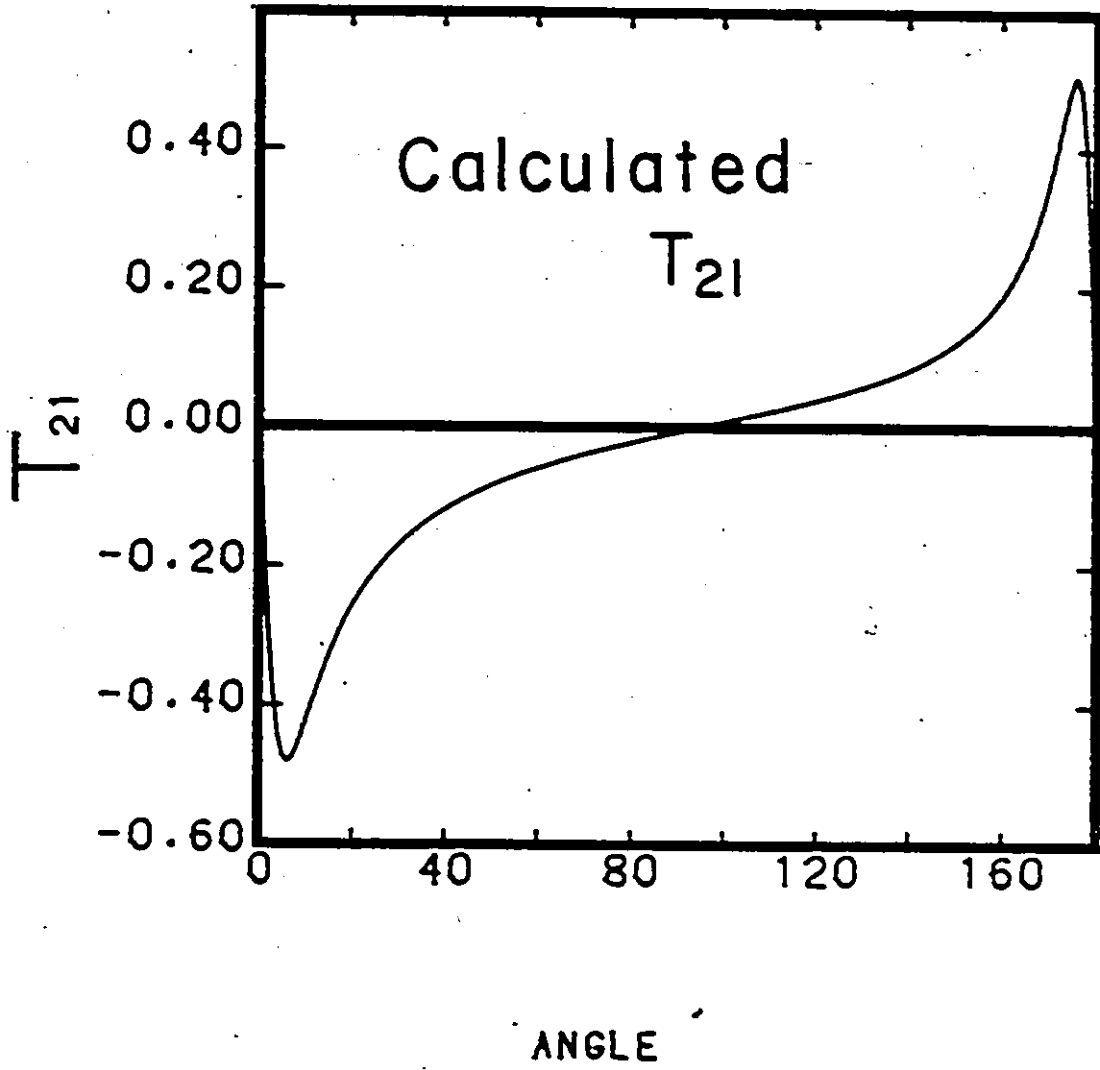
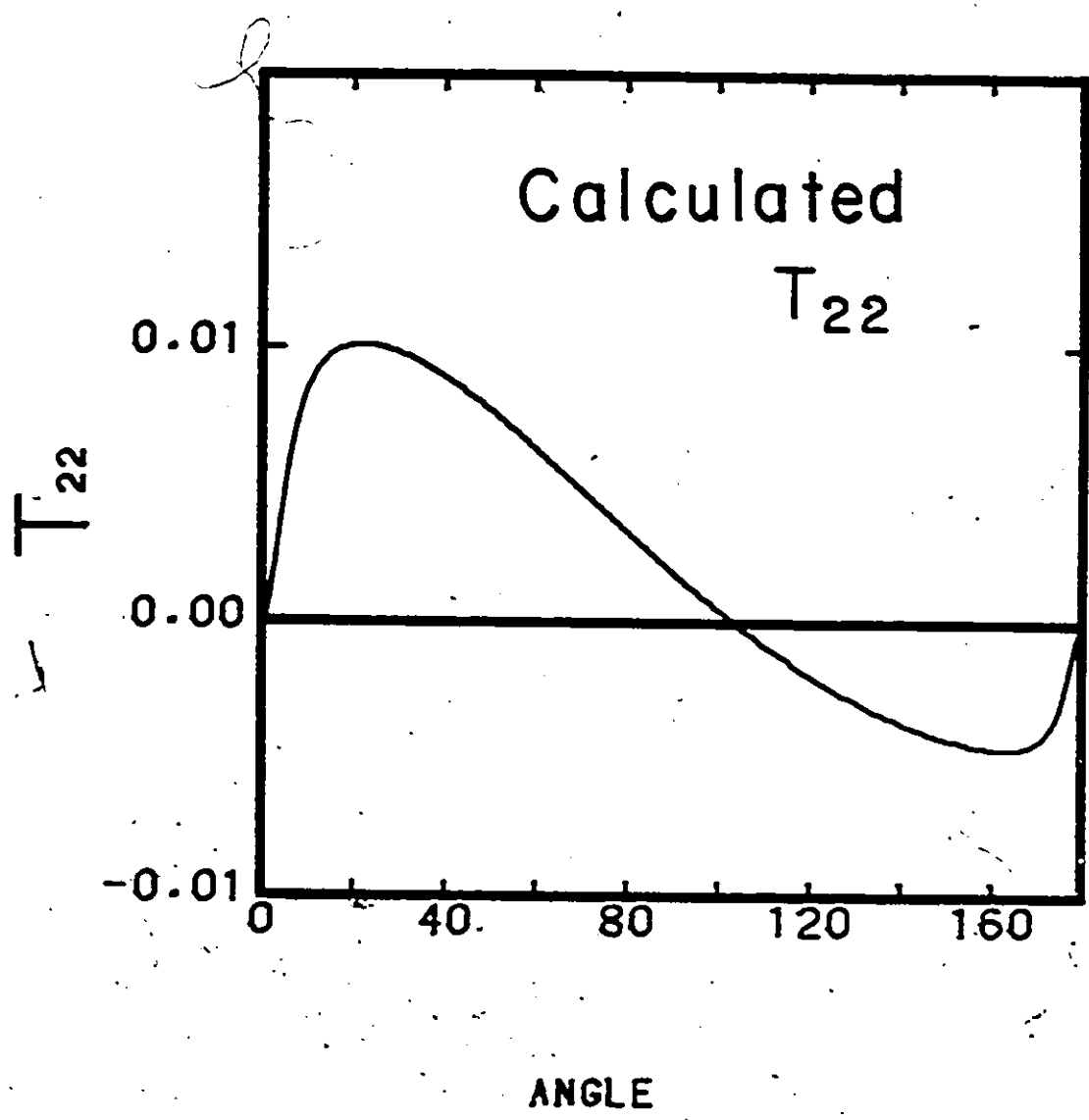
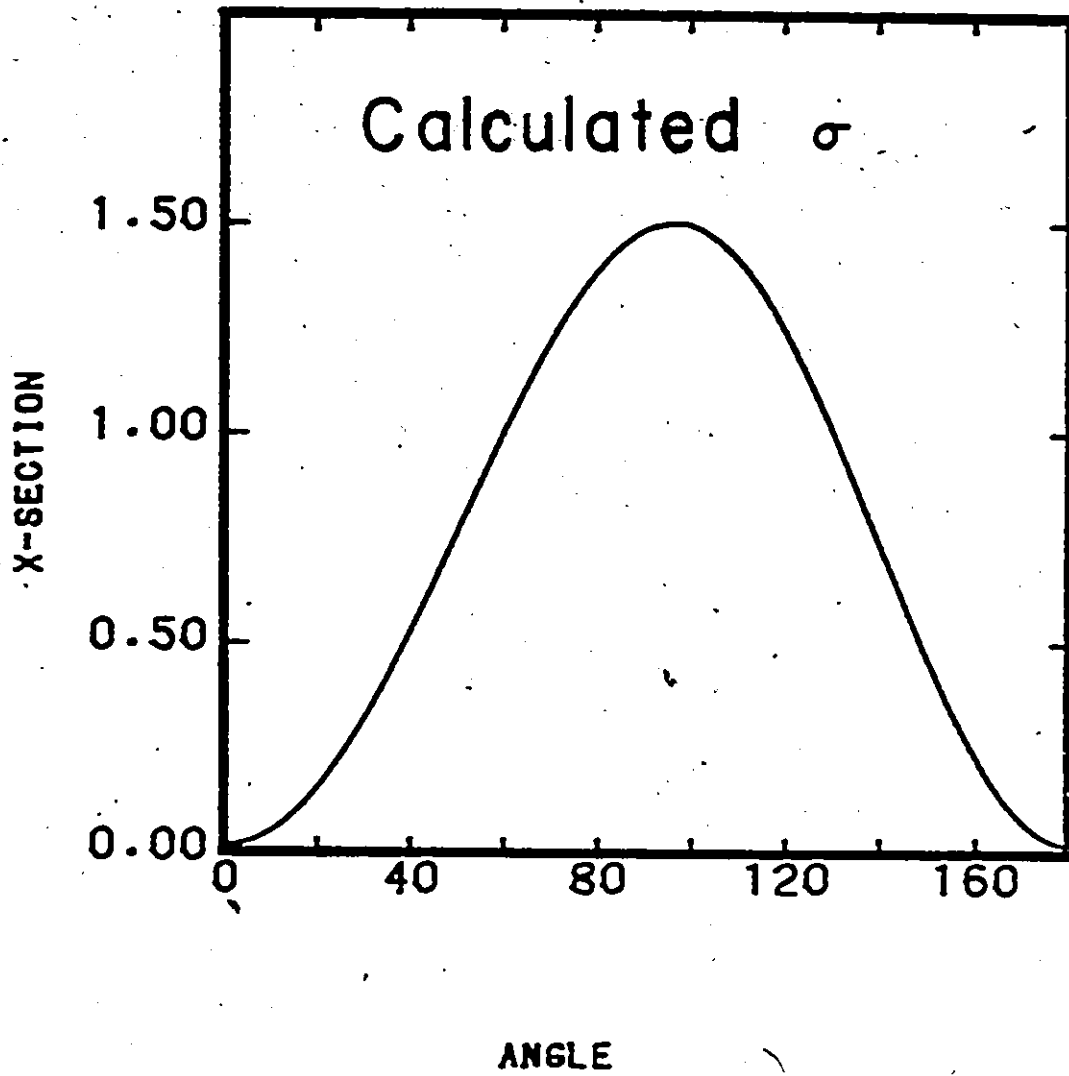


Fig. 6.11 Calculated  $T_{22}$  The  $P_D(d) = 7\%$  wave function was used.



• Fig. 6.12 Calculated differential cross-section. This agrees with the calculation of King et al. (KRS3).





calculation is repeated using these functions instead of realistic wave functions. A comparison of the S-states is shown in fig. 6.13. The two curves are almost identical outside 2.5 fm. This is reasonable since the tail of the wave function should be exponentially decaying. As seen above, only 10% of the E1, P-wave transition amplitude occurs inside 2.0 fm for realistic wave functions whether transitions to the S-state or the D-state are considered. The corresponding percentages with the asymptotic wave functions are 15% for transitions to the S-state and 43% for the D-state. Although the S-state transitions are reasonably well represented using asymptotic wave functions, the D-state transitions are grossly over-estimated in the interior leading to a value of  $T_{20}$  that is too large. This is due to the  $1/r^2$  and  $1/r^3$  terms in the D-state wave function. Hence, even though the radiative capture occurs in the tail of the wave function, the reaction is not purely asymptotic and it is difficult to obtain a model independent value of  $\eta$ . However, since most of the capture amplitude is outside 2.0 fm, and since the interior contributes almost equally to the  $S=1/2$  and  $S=3/2$  channels with realistic wave functions (remember we are concerned with the ratio of these channels) the asymptotic wave functions were cut off at  $r=2.0$  fm, and  $T_{20}(\theta)$  was calculated for different  $\eta$ . Results for  $\eta = -0.02, -0.03, \text{ and } -0.04$  are plotted in fig. 6.14. As found by Arriaga and Santos (ASS4),  $T_{20}$  is proportional to  $\eta$ . A value of  $\eta = -0.032 \pm 0.008$  is

Fig. 6.13 Asymptotic Wave Function. Comparison of the shape of the realistic and asymptotic S-state wave functions.

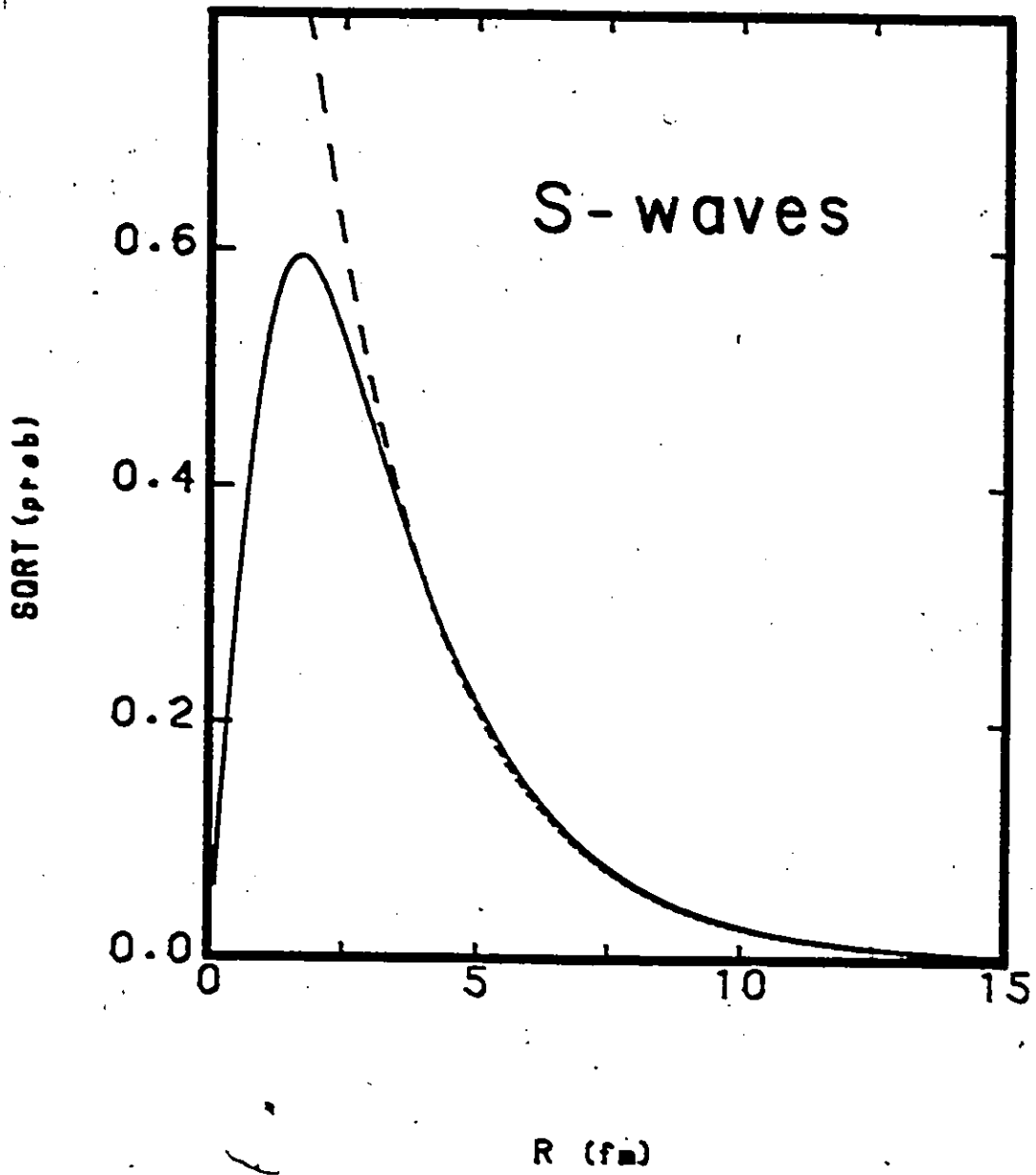
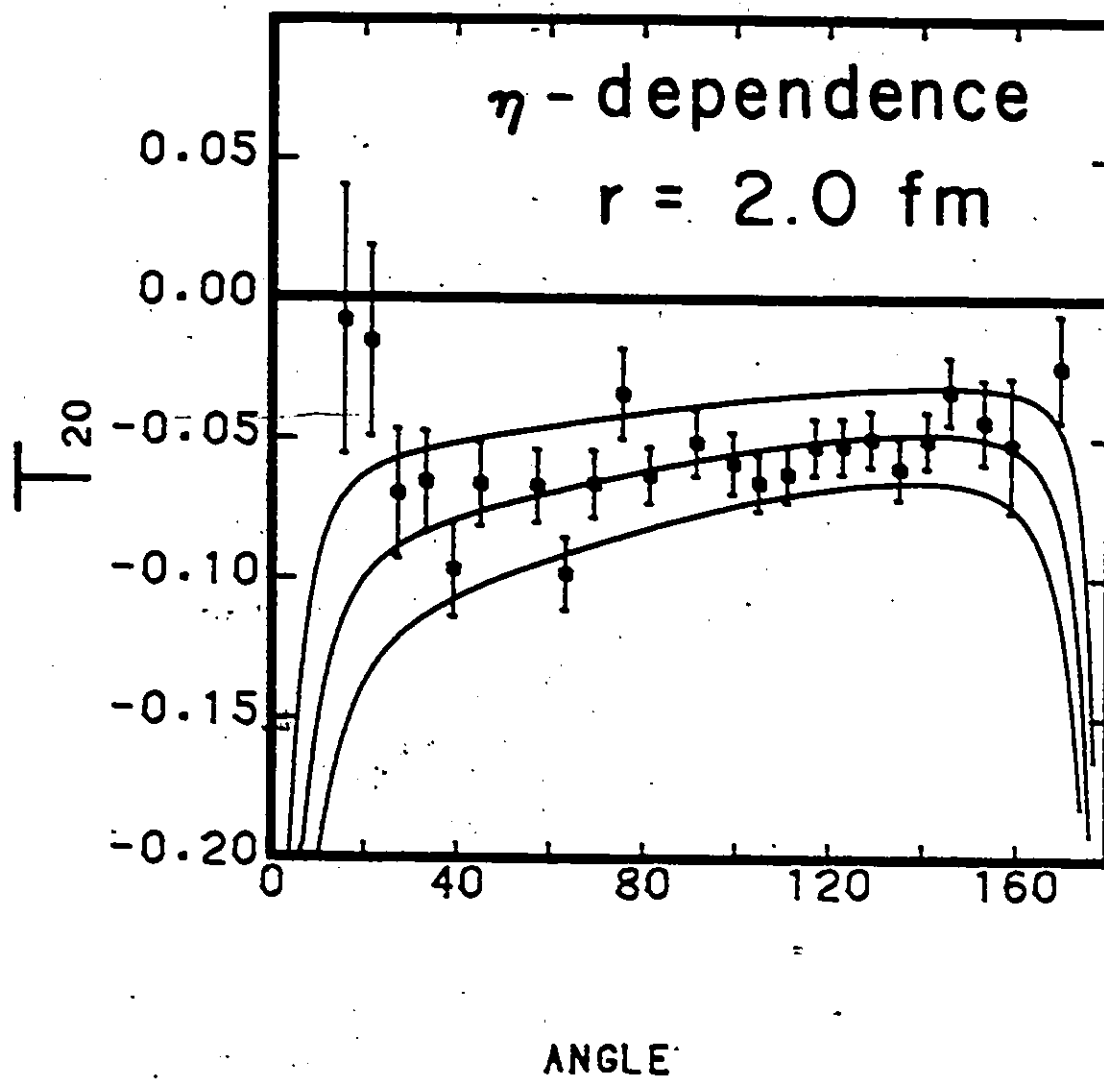


Fig. 6.14  $\eta$  Dependence.  $T_{20}(\theta)$  for different values of the asymptotic D/S state ratio  $\eta$  with  $r_{\text{cut}} = 2.0$  fm. From top to bottom, the curves correspond to  $\eta = -0.02$ ,  $-0.03$ , and  $-0.04$  respectively.



extracted from this graph. This is consistent with the result of (AS84).

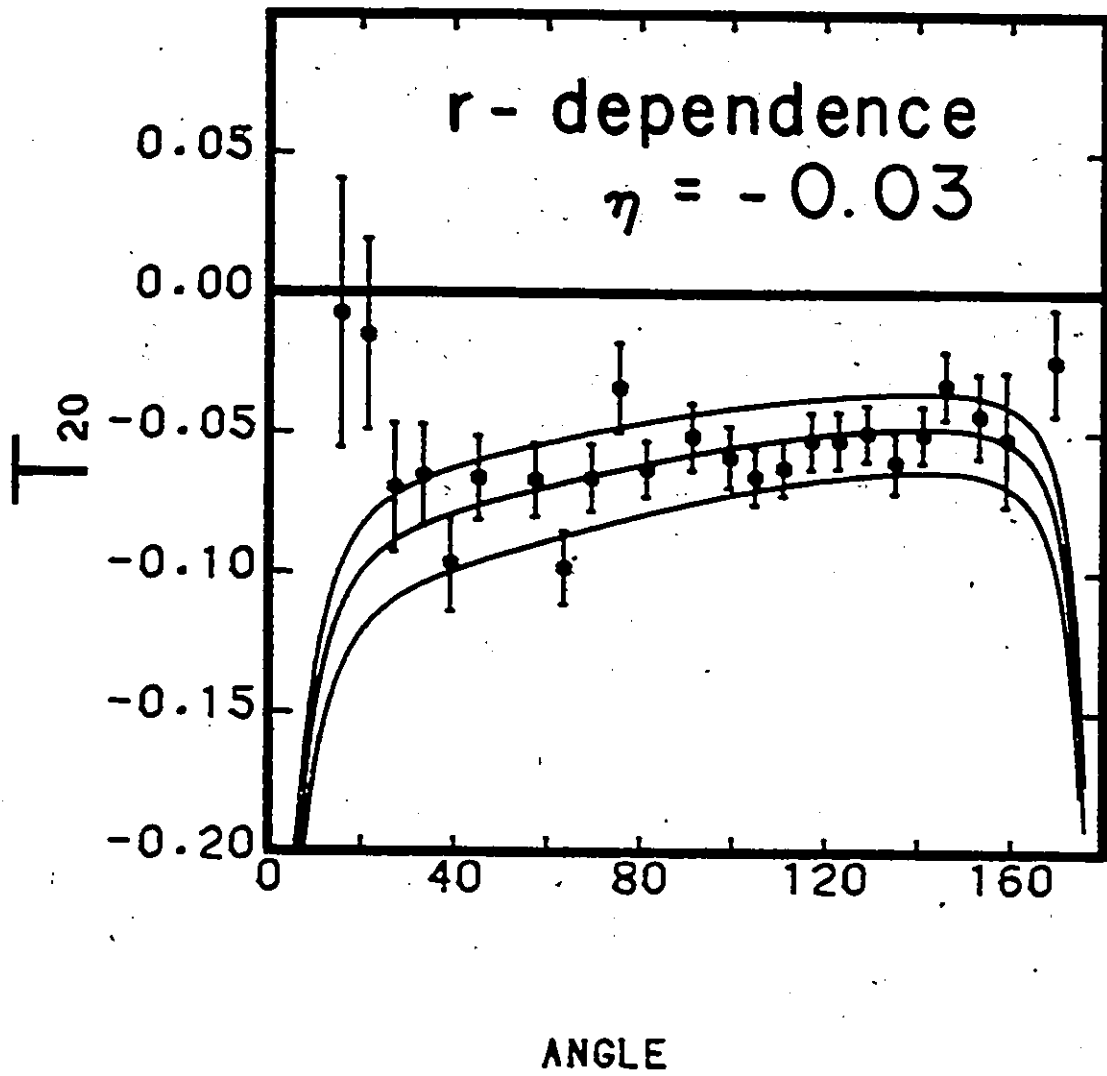
To study the effect of the cut-off radius  $r_{\text{cut}}$ , calculations were done varying this parameter while keeping  $n$  fixed. The results for  $n = -0.03$  and  $r_{\text{cut}} = 1.5, 2.0,$  and  $2.5$  fm are shown in fig. 6.15. We can see that changing  $r_{\text{cut}}$  by one half of one fermi is equivalent to a variation of 0.01 in  $n$ . Hence, the error in  $r_{\text{cut}}$  introduces an additional uncertainty of 0.01 in the asymptotic D/S state ratio. The final value we obtain is:

$$n = -0.032 \pm 0.014$$

This result is useful since the previous range for  $n$  as determined from the  $D_2$  parameter of DWBA (see chap. 2) is:  $-0.065 \leq n \leq -0.039$ , and we can therefore set a new upper limit on the magnitude of  $n$  ( $|n| \leq 0.046$ ).

Fig. 6.15  $r_{\text{cut}}$  Dependence.  $T_{20}(\theta)$  for different values of the cut-off radius with  $n = -0.03$ . From bottom to top, the curves correspond to  $r_{\text{cut}} = 1.5, 2.0,$  and  $2.5$  fm respectively.





## Chapter 7: CONCLUSION.

In conclusion, we will examine what has been learned in this study and what work is necessary to extend our knowledge of the three-body nuclear problem even further.

The first point to be made concerns the data themselves. The detection of the recoiling  $^3\text{He}$  particles has allowed high quality data to be collected which was not possible with other techniques. The quality of these data is determined both by their statistical accuracy and by the number of points obtained in the angular distribution. This distribution is fairly flat with an average value for the analysing power of:

$$T_{20} = -0.065 \pm 0.01$$

The data were fitted to a two-body direct radiative capture model using wave functions generated from Faddeev equations. These wave functions covered a range of 0.74% to 11.52% for the D-state probability in the three-body ground state. Although the sensitivity of the calculation was not as good as expected, a range for  $P_D$  could be determined:

$$5\% \leq P_D(^3\text{He}) \leq 9\%$$

$P_D(^3\text{He})$  is a property of the interior of the nucleus. Indeed, fig. 6.2 shows that the variation in the D-state wave functions occurs mainly inside 2.5 fm. The beam energy obtainable at the McMaster Tandem Accelerator allows us to probe only the edge of this region, and this is why the sensitivity of this measurement to  $P_D$  is reduced.

The data were also analysed in terms of asymptotic wave functions in order to determine the asymptotic D/S state ratio  $\eta$ . A value of:

$$\eta = -0.032 \pm 0.014$$

was found. However, this determination is model dependent because the value of  $\eta$  which gives the best fit to the angular distribution of  $T_{20}$  depends on the choice of  $r_{\text{cut}}$ , the radius at which the asymptotic wave functions are cut off. Nevertheless, this measurement is an improvement over earlier results since it sets a new upper limit, and it is the first direct determination of  $\eta$ , the previous range having been derived from the  $D_2$  parameter in (d,t) and (d, $^3\text{He}$ ) reactions.

An immediate extension of the present work is to measure  $T_{20}$  for a somewhat higher-beam energy to probe deeper into the nucleus. It is hoped that this will improve the sensitivity to  $P_D(^3\text{He})$ . Furthermore, a measurement at lower energy may remove the dependence of  $\eta$  on the value of the cut-off radius, allowing a model independent

determination of this quantity.

Figures 6.10 and 6.11 show calculations for  $T_{21}$  and  $T_{22}$ . Measurements of  $T_{21}$  were attempted but it was not deemed fruitful to continue since they are difficult and  $T_{21}$  does not show more sensitivity to the D-state probability than  $T_{20}$ . The small value of  $T_{22}$  makes a measurement of this quantity nearly impossible because the statistics required would make the experiment prohibitively long.

A more promising experiment is to compare the vector analysing power  $A_y$  (or  $iT_{11}$ ) for the  ${}^1\text{H}(\vec{d}, \gamma){}^3\text{He}$  and  ${}^2\text{H}(\vec{p}, \gamma){}^3\text{He}$  reactions. It has been calculated that the ratio of these quantities should be sensitive to the channel spin ( $S=1/2$  or  $S=3/2$ ) (KR84). Since the  $S=3/2$  channel is related to the D-state probability, this study would be useful. The first part of this comparison has been done at McMaster using the recoil method and the second experiment is planned for the near future.

As mentioned in chapter 2, initial state interactions between the deuteron and the proton were ignored in the calculation. These could lead to mixing of the  $S=1/2$  and  $S=3/2$  channels. Hence, an obvious improvement to the theory would be a full three-body calculation in the entrance channel which would take into account these effects.

In conclusion, we mention that radiative capture has also been found useful in the study of other few body

systems. In particular, the use of polarized beams has improved our ability to study small components of the wave function.

## Appendix A

### RELATIVISTIC KINEMATICS.

The equations introduced in chapter 3 will be derived in this appendix which is an extension of ref. (Mo60). A good treatment of the kinematics of nuclear reactions can be found in ref. (BG61). Consider the inelastic collision  $2(1,3)4$ , where particle 1 strikes particle 2, which is stationary, resulting in the ejection of particles 3 and 4 in the directions  $(\theta_3, \phi_3)$  and  $(\theta_4, \phi_4)$  respectively. To avoid lengthy expressions involving the velocity of light  $c$ , all quantities are given in energy units. Hence, for particle  $j$ , we have:

$M_j = m_j c^2$  ;  $P_j = p_j c$  ;  $W_j = E_j + M_j = (M_j^2 + p_j^2)^{1/2}$   
where  $m_j$  is the rest mass,  $p_j$  is the momentum,  $W_j$  is the total energy, and  $E_j$  is the kinetic energy. In what follows, primed quantities refer to the relativistic center-of-mass frame (CM) in which the total linear momentum vanishes.

Momentum and total energy must be conserved in the reaction; therefore:

$$\vec{P}_1 + \vec{P}_2 = \vec{P}_3 + \vec{P}_4 \quad (\text{A.1})$$

$$W_1 + W_2 = W_3 + W_4 \quad (\text{A.2})$$

Using the fact that particle 2 is at rest leads to:

$$\vec{p}_1 = \vec{p}_3 + \vec{p}_4 \quad (\text{A.3})$$

$$W_1 + M_2 = W_3 + W_4 \quad (\text{A.4})$$

Decomposing the momenta into their components in the CM frame, we get:

$$\begin{aligned} p'_x &= p' \sin(\theta') \cos(\phi') \\ p'_y &= p' \sin(\theta') \sin(\phi') \\ p'_z &= p' \cos(\theta') \end{aligned} \quad (\text{A.5})$$

Since the total momentum vanishes in the CM frame:

$$P'_3 \sin(\theta'_3) \cos(\phi'_3) + P'_4 \sin(\theta'_4) \cos(\phi'_4) = 0 \quad (\text{A.6})$$

$$P'_3 \sin(\theta'_3) \sin(\phi'_3) + P'_4 \sin(\theta'_4) \sin(\phi'_4) = 0 \quad (\text{A.7})$$

$$P'_3 \cos(\theta'_3) + P'_4 \cos(\theta'_4) = 0 \quad (\text{A.8})$$

Dividing eq. A.6 by eq. A.7, we have:

$$\cotan(\phi'_3) = \cotan(\phi'_4) \quad + \quad |\phi'_4 - \phi'_3| = \pi \quad (\text{A.9})$$

which gives:

$$\cos(\phi'_4) = -\cos(\phi'_3) \quad \text{and} \quad \sin(\phi'_4) = -\sin(\phi'_3) \quad (\text{A.10})$$

Using A.10 in equations A.6 to A.8, we get:

$$\left. \begin{aligned} P'_3 \sin(\theta'_3) &= P'_4 \sin(\theta'_4) \\ P'_3 \cos(\theta'_3) &= -P'_4 \cos(\theta'_4) \end{aligned} \right\} \rightarrow \tan(\theta'_3) = -\tan(\theta'_4)$$

$$\sin(\theta'_3) = \sin(\theta'_4)$$

$$\cos(\theta'_3) = -\cos(\theta'_4)$$

$$\theta'_3 + \theta'_4 = \pi \quad (\text{A.11})$$

$$P'_3 = P'_4 \quad (\text{A.12})$$

Equations A.9, A.11, and A.12 are the familiar result that the products of the reaction recoil from each other in a straight line and have the same momentum  $|P|$  in the CM frame.

Since momentum and energy form a four-vector, their components in the lab and CM frames are related by a Lorentz transformation:

$$p'_x = p_x \quad ; \quad p'_y = p_y \quad (\text{A.13})$$

$$p'_z = \gamma (p_z - \beta W) \quad ; \quad W' = \gamma (W - \beta p_z)$$

where:  $\beta = v/c$  ,  $\gamma = (1 - \beta^2)^{-1/2}$  (A.14)

and  $v$  is the velocity of the CM frame in the lab frame. From the definition of the CM frame with respect to the initial particles, we have:

$$\begin{aligned} P'_1 + P'_2 = 0 \quad + \quad P'_{z1} + P'_{z2} = 0 \\ + \quad \gamma (P_1 \cos(\theta_1) - \beta W_1) + \gamma (P_2 \cos(\theta_2) - \beta W_2) = 0 \end{aligned}$$

Since  $\theta_1 = 0$  and  $P_2 = 0$ :

$$\begin{aligned} P_1 - \beta (W_1 + W_2) = 0 \quad + \quad \beta = P_1 / (W_1 + W_2) \\ + \quad \beta = P_1 / (W_1 + M_2) \quad (\text{A.15}) \end{aligned}$$



The groundwork is set to calculate the quantities of interest for the study of the  ${}^1\text{H}(\bar{d}, \gamma){}^3\text{He}$  reaction, namely the energies and directions of the outgoing particles. First we calculate the energy in the CM frame of particle 3.

$$\begin{aligned} W'_3 + W'_4 &= \gamma ( W_3 - \beta P_3 \cos(\theta_3) + W_4 - \beta P_4 \cos(\theta_4) ) \\ &= \gamma [ W_3 + W_4 - \beta (P_3 \cos(\theta_3) + P_4 \cos(\theta_4)) ] \quad (\text{A.16}) \end{aligned}$$

From A.8 and A.13, we have:

$$\begin{aligned} \vec{p}'_{z3} + \vec{p}'_{z4} &= 0 \\ \gamma ( P_3 \cos(\theta_3) - \beta W_3 ) + \gamma ( P_4 \cos(\theta_4) - \beta W_4 ) &= 0 \\ P_3 \cos(\theta_3) + P_4 \cos(\theta_4) &= \beta (W_3 + W_4) \quad (\text{A.17}) \end{aligned}$$

Combining A.16 and A.17, we obtain:

$$W'_3 + W'_4 = \gamma (1 - \beta^2) (W_3 + W_4) = 1/\gamma (W_3 + W_4) \quad (\text{A.18})$$

Let us now express  $1/\gamma$  in terms of masses and energies:

$$1/\gamma = (1 - \beta^2)^{1/2} = [ 1 - (P_1^2 / (W_1 + M_2)^2) ]^{1/2}$$

where equation A.15 was used for  $\beta$ .

Recalling that  $P_1^2 = W_1^2 - M_1^2$ , we can write for  $1/\gamma$ :

$$1/\gamma = (M_1^2 + M_2^2 + 2 M_2 W_1)^{1/2} / (W_1 + M_2)$$

Substituting into equation A.18 and recalling that  $W_3 + W_4 = W_1 + M_2$ , we get:

$$W'_3 + W'_4 = (M_1^2 + M_2^2 + 2 M_2 W_1)^{1/2} \quad (\text{A.19})$$

$$\text{But } W'_4 = (P_4'^2 + M_4'^2)^{1/2}$$

which, since  $P'_3 = P'_4$ , gives:  $W'_4 = (P_3'^2 + M_4'^2)^{1/2}$

and finally:  $W'_4 = (W_3'^2 - M_3' + M_4'^2)^{1/2}$

Putting this into A.19 and solving for  $W_3'$ , we obtain the final expression for the energy of particle 3 in the CM frame:

$$W_3' = a/2 (M_1^2 + M_2^2 + 2 M_2 W_1)^{1/2} \quad (\text{A.20})$$

$$\text{where } a = M_1^2 + M_2^2 + M_3^2 - M_4^2 + 2 M_2 W_1 \quad (\text{A.21})$$

We now calculate the angle  $\theta_3'$  at which particle 3 is ejected in the CM frame as a function of  $E_4$ , the kinetic energy of particle 4 in the lab frame. Since this relates the angle of the  $\gamma$ -ray to the energy of the  $^3\text{He}$  particle, this makes the recoil method possible. Eq. A.13 gives:

$$P_3' \cos(\theta_3') = \gamma (P_3 \cos(\theta_3) - \beta W_3)$$

$$W_3' = \gamma (W_3 - \beta P_3 \cos(\theta_3))$$

Solving for  $P_3 \cos(\theta_3)$  in the second equation and substituting into the first, we have:

$$\begin{aligned} P_3' \cos(\theta_3') &= \gamma (W_3/\beta - W_3'/\beta\gamma - \beta W_3) \\ &= \gamma [ (1 - \beta^2)W_3/\beta - W_3'/\beta\gamma ] \\ &= 1/\beta (W_3/\gamma - W_3') \end{aligned}$$

where we have used  $\gamma (1 - \beta^2) = 1/\gamma$ . Since particle 3 is a  $\gamma$ -ray, it has zero mass and  $W_3' = P_3'$ . Therefore:

$$\cos(\theta_3') = 1/\beta W_3' (W_3/\gamma - W_3')$$

Recall eq. A.14:  $W_3 = W_1 + M_2 - W_4$ . We have seen that  $W_j = E_j + M_j$ . Therefore  $W_3 = E_1 + M_1 + M_2 - E_4 - M_4$ , and

finally:

$$\cos(\theta_3') = 1/\beta W_3' [ 1/\gamma (E_1 + M_1 + M_2 - M_4 - E_4) - W_3' ] \quad (\text{A.22})$$

where  $W_3'$  is known from eq. A.20. Hence, we have a relationship between  $\theta_3'$  and  $E(^3\text{He})$ .

The final point to study is the angular distribution of the  $^3\text{He}$  particles. From eq. A.13, we have:

$$W_4' = \gamma (W_4 - \beta P_4 \cos(\theta_4))$$

$$\cos(\theta_4) = 1/\beta P_4 (W_4 - W_4'/\gamma)$$

$$\text{but: } P_4^2 = W_4^2 - M_4^2 = (E_4 + M_4)^2 - M_4^2 = E_4^2 + 2 M_4 E_4$$

$$\text{and: } W_4 = E_4 + M_4.$$

Therefore:

$$\cos(\theta_4) = (E_4 + M_4 - W_4'/\gamma) / \beta (E_4^2 + 2 M_4 E_4)^{1/2} \quad (\text{A.23})$$

Appendix B

COEFFICIENTS  $a_k$  AND  $c_k$

This appendix gives expressions for the  $a_k$  and  $c_k$  coefficients used to calculate  $T_{20}$  in the following equation:

$$T_{20}(\theta) = \frac{\sum_k c_k P_k(\cos(\theta))}{\sum_k a_k P_k(\cos(\theta))}$$

The equations defining these coefficients can be found in ref. (SW79b). The notation used for the matrix elements is defined in chapter 2. The relative phase factor has been omitted from these expressions and is assumed included:

$$\text{ie. } 1.155 \text{ } ^2P_2 \text{ } ^2D_4 = 1.155 \text{ } ^2P_2 \text{ } ^2D_4 \cos(\phi(^2P_2) - \phi(^2D_4)).$$

Note that only E1 and E2 transitions are included here..

$$\begin{aligned} a_0 = & 0.333 \text{ } ^2P_2 \text{ } ^2 + 0.333 \text{ } ^4P_2 \text{ } ^2 + 0.667 \text{ } ^2P_4 \text{ } ^2 + 0.667 \text{ } ^4P_4 \text{ } ^2 \\ & + 0.667 \text{ } ^4F_4 \text{ } ^2 + 0.667 \text{ } ^2D_4 \text{ } ^2 + 0.667 \text{ } ^4S_4 \text{ } ^2 + 0.667 \text{ } ^4D_4 \text{ } ^2 \\ & + \text{ } ^2D_6 \text{ } ^2 + \text{ } ^4D_6 \text{ } ^2 + \text{ } ^4G_6 \text{ } ^2 \end{aligned}$$

$$\begin{aligned}
 a_1 = & 1.155 \ ^2P_2 \ ^2D_4 - 0.816 \ ^4P_2 \ ^4S_4 + 0.816 \ ^4P_2 \ ^4D_4 \\
 & + 0.231 \ ^2P_4 \ ^2D_4 + 2.078 \ ^2P_4 \ ^2D_6 + 0.516 \ ^4P_4 \ ^4S_4 \\
 & + 0.413 \ ^4P_4 \ ^4D_4 + 1.739 \ ^4P_4 \ ^4D_6 + 0.310 \ ^4F_4 \ ^4D_4 \\
 & - 0.248 \ ^4F_4 \ ^4D_6 + 2.028 \ ^4F_4 \ ^4G_6
 \end{aligned}$$

$$\begin{aligned}
 a_2 = & -0.667 \ ^2P_2 \ ^2P_4 + 0.211 \ ^4P_2 \ ^4P_4 - 0.632 \ ^4P_2 \ ^4F_4 \\
 & - 0.333 \ ^2P_4 \ ^2 + 0.267 \ ^4P_4 \ ^2 + 0.400 \ ^4P_4 \ ^4F_4 \\
 & - 0.267 \ ^4F_4 \ ^2 + 0.333 \ ^2D_4 \ ^2 + 0.286 \ ^2D_4 \ ^2D_6 \\
 & - 0.667 \ ^4S_4 \ ^4D_4 + 0.535 \ ^4S_4 \ ^4D_6 + 0.382 \ ^4D_4 \ ^4D_6 \\
 & + 0.571 \ ^2D_6 \ ^2 + 0.204 \ ^4D_6 \ ^2 - 0.300 \ ^4D_6 \ ^4G_6 \\
 & + 0.510 \ ^4G_6 \ ^2 + 0.374 \ ^4D_4 \ ^4G_6
 \end{aligned}$$

$$\begin{aligned}
 a_3 = & -1.155 \ ^2P_2 \ ^2D_6 + 0.436 \ ^4P_2 \ ^4D_6 - 1.069 \ ^4P_2 \ ^4G_6 \\
 & - 1.386 \ ^2P_4 \ ^2D_4 - 0.924 \ ^2P_4 \ ^2D_6 + 0.620 \ ^4P_4 \ ^4D_4 \\
 & + 0.883 \ ^4P_4 \ ^4D_6 + 0.676 \ ^4P_4 \ ^4G_6 + 1.033 \ ^4F_4 \ ^4S_4 \\
 & - 0.826 \ ^4F_4 \ ^4D_4 + 0.662 \ ^4F_4 \ ^4D_6 - 0.676 \ ^4F_4 \ ^4G_6
 \end{aligned}$$

$$\begin{aligned}
 a_4 = & -2.286 \ ^2D_4 \ ^2D_6 + 1.746 \ ^4S_4 \ ^4G_6 + 1.222 \ ^4D_4 \ ^4D_6 \\
 & - 1.247 \ ^4D_4 \ ^4G_6 - 0.571 \ ^2D_6 \ ^2 + 0.653 \ ^4D_6 \ ^2 + \ ^4D_6 \ ^4G_6 \\
 & - 0.367 \ ^4G_6 \ ^2
 \end{aligned}$$

$$\begin{aligned}
 c_0 = & 0.667 \ ^2P_2 \ ^4P_2 - 0.236 \ ^4P_2 \ ^2 - 0.422 \ ^2P_4 \ ^4P_4 \\
 & + 1.265 \ ^2P_4 \ ^4F_4 + 0.377 \ ^4P_4 \ ^2 + 0.566 \ ^4P_4 \ ^4F_4 \\
 & - 0.377 \ ^4F_4 \ ^2 + 0.943 \ ^2D_4 \ ^4D_4 - 0.943 \ ^4S_4 \ ^2D_4 \\
 & + 0.943 \ ^4S_4 \ ^4D_4 - 0.756 \ ^2D_6 \ ^4D_6 + 1.852 \ ^2D_6 \ ^4G_6 \\
 & + 0.505 \ ^4D_6 \ ^2 + 0.990 \ ^4D_6 \ ^4G_6 - 0.505 \ ^4G_6 \ ^2
 \end{aligned}$$

$$\begin{aligned}
c_1 = & -0.816 \ 2P_2^4 S_4 + 0.816 \ 2P_2^4 D_4 + 1.155 \ 4P_2^2 D_4 \\
& + 0.577 \ 4P_2^4 S_4 - 0.577 \ 4P_2^4 D_4 - 0.163 \ 2P_4^4 S_4 \\
& + 0.163 \ 2P_4^4 D_4 - 0.786 \ 2P_4^4 D_6 + 1.924 \ 2P_4^4 G_6 \\
& + 0.292 \ 4P_4^4 S_4 + 0.365 \ 4P_4^4 D_4 - 0.657 \ 4P_4^2 D_6 \\
& + 0.878 \ 4P_4^4 D_6 + 0.861 \ 4P_4^4 G_6 + 0.219 \ 4F_4^2 D_4 \\
& + 0.219 \ 4F_4^4 S_4 + 1.972 \ 4F_4^2 D_6 + 0.878 \ 4F_4^4 D_6 \\
& - 1.147 \ 4F_4^4 G_6 - 0.073 \ 4P_4^2 D_4
\end{aligned}$$

$$\begin{aligned}
c_2 = & 0.211 \ 2P_2^4 P_4 - 0.632 \ 2P_2^4 F_4 - 0.149 \ 4P_2^4 P_4 \\
& + 0.447 \ 4P_2^4 F_4 + 0.211 \ 2P_4^4 P_4 - 0.632 \ 2P_4^4 F_4 \\
& + 0.236 \ 4P_4^2 + 0.236 \ 4F_4^2 + 0.471 \ 2D_4^4 D_4 \\
& - 0.108 \ 2D_4^4 D_6 + 0.265 \ 2D_4^4 G_6 - 0.471 \ 4S_4^2 D_4 \\
& - 0.236 \ 4S_4^2 - 0.202 \ 4S_4^2 D_6 + 0.270 \ 4S_4^4 D_6 \\
& + 0.265 \ 4S_4^4 G_6 - 0.236 \ 4D_4^2 + 0.202 \ 4D_4^2 D_6 \\
& + 0.378 \ 4D_4^4 D_6 - 0.432 \ 2D_6^4 D_6 + 1.058 \ 2D_6^4 G_6 \\
& + 0.029 \ 4D_6^2 + 0.353 \ 4D_6^4 G_6 - 0.332 \ 4G_6^2 \\
& - 0.667 \ 4P_2^2 P_4
\end{aligned}$$

$$\begin{aligned}
c_3 = & 0.436 \ 2P_2^4 D_6 - 1.069 \ 2P_2^4 G_6 - 1.155 \ 4P_2^2 D_6 \\
& - 0.309 \ 4P_2^4 D_6 + 0.756 \ 4P_2^4 G_6 + 0.980 \ 2P_4^4 S_4 \\
& - 0.980 \ 2P_4^4 D_4 + 0.349 \ 2P_4^4 D_6 - 0.855 \ 2P_4^4 G_6 \\
& + 0.438 \ 4P_4^2 D_4 + 0.438 \ 4P_4^4 S_4 + 0.292 \ 4P_4^2 D_6 \\
& + 0.781 \ 4P_4^4 D_6 + 0.096 \ 4P_4^4 G_6 - 1.315 \ 4F_4^2 D_4 \\
& - 0.584 \ 4F_4^4 S_4 + 0.730 \ 4F_4^4 D_4 - 0.876 \ 4F_4^2 D_6 \\
& + 0.669 \ 4F_4^4 G_6
\end{aligned}$$

$$\begin{aligned}
 c_4 = & 0.864 \ ^2D_4 \ ^4D_6 - 2.116 \ ^2D_4 \ ^4G_6 + 1.616 \ ^4S_4 \ ^2D_6 \\
 & + 0.864 \ ^4S_4 \ ^4D_6 - 0.882 \ ^4S_4 \ ^4G_6 - 1.616 \ ^4D_4 \ ^2D_6 \\
 & + 1.234 \ ^4D_4 \ ^4G_6 + 0.432 \ ^2D_6 \ ^4D_6 - 1.058 \ ^2D_6 \ ^4G_6 \\
 & + 0.577 \ ^4D_6^2 + 0.141 \ ^4D_6 \ ^4G_6 + 0.433 \ ^4G_6^2
 \end{aligned}$$

## BIBLIOGRAPHY

- AC83 - M. Anghinolfi, P. Corvisiero, M. Guarnone, G. Ricco, and A. Zucchiatti, Nuc. Phys. A410 173(1983).
- AD81 - S. Aufleger and D. Drechsel, Nuc. Phys. A364 81(1981).
- AS84 - A. Arriaga and F.D. Santos, Phys. Rev. C29 1945(1984).
- BB70 - B.D. Belt, C.R. Bingham, M.L. Halbert, and A. van der Woude, Phys. Rev. Lett. 24 1120(1970).
- Be70 - B.D. Belt, PhD. thesis, Univ. of Tennessee.
- BG61 - A.M. Baldin, V.I. Goldanskii, and I.L. Rozenthal, "Kinematics of Nuclear Reactions." Oxford University Press, 1961
- B153 - J.M. Blatt, Phys. Rev. 89 86(1953).
- BP77 - B. Buck and A.A. Pilt, Nuc. Phys. A280 133(1977).
- Da70 - S.E. Darden  
"Proceedings of the Third International Symposium on Polarization Phenomena in Nuclear Reactions."  
edited by H.H. Barschall and W. Haeberli (1970) p.39.
- DB58 - G. Derrick and J.M. Blatt, Nuc. Phys. 8 310(1958).
- De67 - L.M. Delves  
"Few Body Problems, Light Nuclei, and Nuclear Interactions" Vol. 1,  
edited by G. Paic and I. Slaus (1967) p.153.  
- L.M. Delves and A.C. Phillips  
Rev. Mod. Phys. 41 497(1969).
- Fe70 - H. Feshbach  
"Proceedings of the Third International Symposium on Polarization Phenomena in Nuclear Reactions."  
edited by H.H. Barschall and W. Haeberli (1970) p.29.
- FG82 - J.L. Friar, B.F. Gibson, D.R. Lehman, and G.L. Payne  
Phys. Rev. C25 1616(1982).
- GL84 - B.F. Gibson and D.R. Lehman, Phys. Rev. C29 1017(1984).



- Go58 - L.J.B. Goldfarb, Nuc. Phys. 7 622(1958).
- HP73 - J.A. Hendry, A.C. Phillips, Nuc. Phys. A211 533(1973).
- In70 - "Proceedings of the Third International Symposium on Polarization Phenomena in Nuclear Reactions." edited by H.H. Barschall and W. Haeberli, Madison, Wisconsin (1970).
- In75 - "Proceedings of the Fourth International Symposium on Polarization Phenomena in Nuclear Reactions." edited by W. Gruebler and V. Konig, Zurich, Switzerland (1975).
- In80 - "Proceedings of the Fifth International Symposium on Polarization Phenomena in Nuclear Reactions." edited by G.G. Ohlsen, R.E. Brown, N. Jarmie, W.W. McNaughton, and G.M. Hale, Santa Fe, New Mexico (1980).
- KC79 - L.D. Knutson, P.C. Colby, and J.A. Bieszk, Phys. Lett. 85B 209(1979).
- Ki83 - S.E. King, PhD. thesis, Duke Univ.
- KG75 - J.A. Kuehner, P.W. Green, G.D. Jones, and D.T. Petty, Phys. Rev. Lett. 35 423(1975).
- KG80 - V. Konig, W. Gruebler, R.E. White, P.A. Schmelzbach, B. Jenny, F. Sperisen, and C. Schweider, "Proceedings of the Fifth International Symposium on Polarization Phenomena in Nuclear Reactions." edited by Ohlsen et al. (1980) p.1208.
- KR83 - S. King, N.R. Roberson, H.R. Weller, and D.R. Tilley Phys. Rev. Lett. 51 877(1983).
- KR84 - S.E. King, N.R. Roberson, H.R. Weller, D.R. Tilley, H.P. Engelbert, H. Berg, E. Huttel, G. Clausnitzer Phys. Rev. C30 1335(1984).
- La55 - W. Lakin, Phys. Rev. 98 139(1955).
- Le84 - D.R. Lehman, private communication.
- LPS1 - D.R. Lehman, W.C. Parke, and L.C. Maximon, J. Math. Phys. 22(7) 1399(1981).
- Mc76 - J.W. McKay, Masters thesis, McMaster Univ.
- MK74 - J.L. Matthews, T. Kruse, M.E. Williams, R.O. Owens, and W. Savin, Nuc. Phys. A223 221(1974).

- ML68 - J.L. McKibben, G.P. Lawrence, and G.G. Ohlsen,  
Phys. Rev. Lett. 20 1180(1968).
- Mo60 - J. Monahan, Fast Neutron Physics, vol. 4, edited by  
J.B. Marion and J.L. Fowler  
Interscience Publishers Inc., New York, 1960, p.49
- Oh70 - G.G. Ohlsen  
"Los Alamos Lamb-Shift Polarized Ion Source: A  
User's Guide." Los Alamos Scientific Laboratory,  
internal publication, 1970.
- Sa84 - F.D. Santos, private communication.
- SA83 - D.M. Skopik, J. Asai, D.H. Beck, T.P. Dielschneider,  
R.E. Pywell, and G.A. Retzlaff,  
Phys. Rev. C28 52(1983).
- Se77 - E. Segre, "Nuclei and Particles", p.31  
Benjamin Cummings Publishing, 1977.
- Si74 - M. Simonius,  
"Polarization Nuclear Physics", edited by D. Fick,  
Springer Verlag (1974) p.38.
- SS79 - T. Sasakawa and T. Sawada, Phys. Rev. C19  
2035(1979).
- SW79a - D.M. Skopik, H.R. Weller, N.R. Roberson,  
and S.A. Wender, Phys. Rev. C19 601(1979).
- SW79b - R.G. Seyler and H.R. Weller, Phys. Rev. C20  
453(1979).
- WA52 - L. Wolfenstein and J. Ashkin, Phys. Rev. 85  
947(1952).
- We84 - H.R. Weller, private communication.
- WRSO - H.R. Weller and N.R. Roberson, Rev. Mod. Phys. 52  
699(1980).